Treating Coalbed Natural Gas Produced Water for Beneficial Use by MFI Zeolite Membranes

Final Report

Submitted by

New Mexico Petroleum Recovery Research Center
New Mexico Institute of Mining and Technology
Socorro, New Mexico 87801

Robert R. Lee
Liangxiong Li

Prepared for

U.S. Department of Energy
National Energy Technology Laboratory
(Project Number: DE-FC26-04NT15548)

Report Submittal Date: April 10 2008

DISCLAIMER

Acknowledgement

This research was sponsored by the U.S. Department of Energy through the National Energy Technology Laboratory (grant # DE-FC26-04NT15548).

The contributions of the project team members and graduate students are greatly appreciated. They are Dr. Ning Liu, Dr. Brian Mcpherson, Ms. Liz Bustmante, Mr. Jun Lu, and Ms. Xinhua Li. Dr. Junhang Dong, Associate professor of Chemical and Materials Engineering (CME) Department at the University of Cincinnati, also contribute to the success of this project.

PUBLIC ABSTRACT

Desalination of brines produced from oil and gas fields is an attractive option for providing potable water in arid regions. Recent field-testing of subsurface sequestration of carbon dioxide for climate management purposes provides new motivation for optimizing efficacy of oilfield brine desalination: as subsurface reservoirs become used for storing CO_2, the displaced brines must be managed somehow. However, oilfield brine desalination is not economical at this time because of high costs of synthesizing membranes and the need for sophisticated pretreatments to reduce initial high TDS and to prevent serious fouling of membranes. In addition to these barriers, oil/gas field brines typically contain high concentrations of multivalent counter cations (eg. Ca^{2+} and SO_4^{2-}) that can reduce efficacy of reverse osmosis (RO). Development of inorganic membranes with typical characteristics of high strength and stability provide a valuable option to clean produced water for beneficial uses.

Zeolite membranes have a well-defined subnanometer pore structure and extreme chemical and mechanical stability, thus showing promising applicability in produced water purification. For example, the MFI-type zeolite membranes with uniform pore size of ~0.56 nm can separate ions from aqueous solution through a mechanism of size exclusion and electrostatic repulsion (Donnan exclusion). Such a combination allows zeolite membranes to be unique in separation of both organics and electrolytes from aqueous solutions by a reverse osmosis process, which is of great interest for difficult separations, such as oil-containing produced water purification.

The objectives of the project "Treating Coalbed Natural Gas Produced Water for Beneficial Use by MFI Zeolite Membranes" are: (1) to conduct extensive fundamental investigations and understand the mechanism of the RO process on zeolite membranes and factors determining the membrane performance, (2) to improve the membranes and optimize operating conditions to enhance water flux and ion rejection, and (3) to perform long-term RO operation on tubular membranes to study membrane stability and to collect experimental data necessary for reliable evaluations of technical and economic feasibilities.

Our completed research has resulted in deep understanding of the ion and organic separation mechanism by zeolite membranes. A two-step hydrothermal crystallization process resulted in a highly efficient membrane with good reproducibility. The zeolite membranes synthesized therein has an overall surface area of ~0.3 m^2 . Multichannel vessels were designed and machined for holding the tubular zeolite membrane for water purification. A zeolite membrane RO demonstration with zeolite membranes fabricated on commercial alpha-alumina support was established in the laboratory. Good test results were obtained for both actual produced water samples and simulated samples. An overall 96.9% ion rejection and 2.23 $kg/m^2.h$ water flux was achieved in the demonstration. In addition, a post-synthesis modification method using Al^{3+}-oligomers was developed for repairing the undesirable nano-scale intercrystalline pores. Considerable enhancement in ion rejection was achieved. This new method of zeolite membrane modification is particularly useful for enhancing the efficiency of ion separation from aqueous solutions because the modification does not need high temperature operation and may be carried out online during the RO operation. A long-term separation test for actual CBM produced water has indicated that the zeolite membranes show excellent ion separation and extraordinary stability at high pressure and produced water environment.

Table of Contents

List of Figures

List of Tables

EXECUTIVE SUMMARY

Introduction

Desalinated brine from oilfields or coalbed methane gasfield is a potential water resource for beneficial use. Produced water typically contains a high concentration of dissolved salts and organic compounds, requiring the desalination technology to be tolerant of strong solvents and high concentrations of salts. To reclaim produced water for beneficial use, dissolved components in produced water, both organics and inorganic salt, must be removed in a cost-effective way. Current technologies, such as polymeric reverse osmosis (RO) membranes, multiple-effect evaporation, and ion exchange, purify produced water with difficulty due to serious fouling, material instability and insufficient efficiency. The project "Treating Coalbed Natural Gas Produced Water for Beneficial Use by MFI Zeolite Membranes" was proposed to develop and demonstrate zeolite membranes for produced water treatment, targeting the removal of both salt and dissolved organics simultaneously.

Project objectives

This project aimed to develop a new technology of reverse osmosis through molecular sieve zeolite membranes for purifying high-TDS CBM produced water. The project included three phases with the following objectives for each phase:

Phase I. The fundamental studies in Phase I include mass-transport behaviors of water, ions, and dissolved organics passed through the zeolite membranes of varied Si/Al ratios; and effects of operation temperature, pressure, feed velocity, feed chemical composition, and pH on RO performance.

Phase II. Research focuses on optimizing RO operating conditions and developing a cost-effective method to repair the undesirable nanoscale intercrystalline pores.

Phase III. A RO unit with a 0.1-m² tubular membrane module will be established to carry out long-term operations testing for technical and economic evaluations.

Project achievements

Researchers focused on membrane fabrication, ion/water transport in confined zeolite pores, and module design. Considerable success has been achieved through the proposed processes, including (1) experimental demonstration of ion separation by zeolite membranes, (2) development of a two-step process for zeolite fabrication with high flux and good reproducibility, (3) establishment of a mathematical model for describing the ion/water competitive diffusion through zeolite membranes, (4) development of a post-synthesis modification method for "healing" of zeolite intercrystalline pores, and (5) construction of a RO demonstration with membrane area of 0.3 m^2.

In phase I, ion separation by zeolite membranes has been sucessfuly demonstrated and a two-step process for fabrication of high-flux zeolite membranes has been established. Pure silica zeolite membranes have been synthesized on both lab-made disc substrate and commercial tubular substrate. The pure silicalite zeolite membranes synthesized by in-situ hydrothermal crystallization process show good ion separation efficiency but low water flux. To enhance water throughput, hydrophilic zeolite membranes with high aluminum content in zeolite framework have been synthesized on tubular alpha-alumina substrate by a two-step process. Zeolite membranes show high ion removal efficiency at a mechanism of size exclusion and electrostatic repulsion. Zeolite

membranes synthesized with the newly developed two-step crystallization show considerable enhancement in RO separation with a water flux increase averaged from 0.165 to 2.23 kg/m^2.h and ion rejection improvement from 66.5% to 96.9%. Also, over 91% of zeolite membranes synthesized with this process show high ion rejection efficiency, indicating good reproducibility and the potential for large-scale application of this technology. Figure 1 shows the tubular zeolite membranes synthesized with the two-step hydrothermal crystallization. Each zeolite membrane was tested for ion rejection and water flux, which is indicated in Fig. 2.

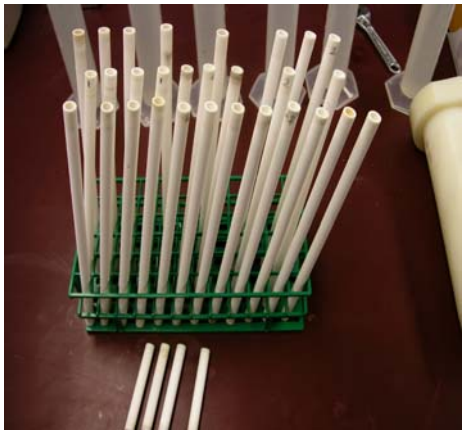

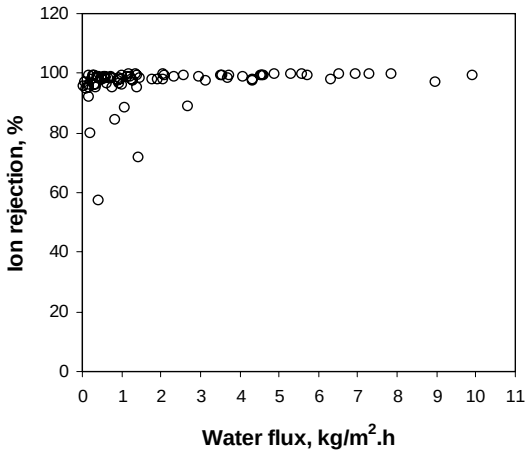

Fig. 1. Picture of tubular zeolite membranes synthesized by two-step hydrothermal crystallization.	**Fig. 2. Ion separation performance of zeolite membranes synthesized by two-step hydrothermal treatment.**

Influences of ion species, ion valence, transmembrane pressure and water sweeping flow rate on the zeolite membrane RO performance have been investigated. Experimental results suggest that size exclusion of large hydrated ions is the major mechanism of ion separation by zeolite membranes. Also, electrostatic repulsion plays critical role in ion separation from intercrystalline pores.

In Phase II, a post-synthesis modification for enhanced ion separation has been established. An efficient process for membrane modification was developed by depositing metal oligomers into the zeolite intercrystalline pore region. To selectively deposite metal oligomers into zeolite intercrystalline pores, on-line filtration and counter diffusion were applied to modify the pore structure of zeolite membrane or "heal" the non-selective intercrystalline pores. Al^{3+}-oligomers were screened out from other metal ions because of their appropriate size and oligomer growth rate. At the same operating pressure, water flux declined while the ion rejection rate increased significantly after modification. The membrane modified by metal oligomer deposition was tested with actual produced water (TDS=1.2×10^4 ppm) for long-term stability evaluation. Ion rejection remained nearly constant while water flux declined slightly with elapsed time for more than 500 hr, indicating the strong attachment of metal oligomers in zeolite pores, with no need for reinforcement.

A mathematical model for describing ion/water permeation through zeolite thin film has been developed. Activated diffusion at zeolite pore entrance governs the ion diffusion through zeolite membranes. Raising temperature has a greater influence on the ion permeation than on the water permeation, resulting in a decline of the ion rejection. On the contrary, increasing the transmembrane pressure can enhance both the water flux and ion rejection rates because the ion flux is much less affected by pressure compared to the water flux. These findings suggest that for RO on zeolite membranes, operating at elevated temperatures and high hydraulic pressures is desirable for enhancing the separation efficiency.

In Phase III, a zeolite membrane demonstration with membrane surface area of 0.3 m^2 has been constructed and long-term permeation of produced water has been performed. About 73 zeolite membranes (total surface area of ~0.3m^2) with good ion separation efficiency and high water flux have been synthesized. Each membrane was tested for RO separation on 0.1 M NaCl solution for membrane quality evaluation. A multichannel nylon vessel was designed and machined for the cross-flow RO permeation of tubular zeolite membranes. A reverse osmosis demonstration with total membrane surface area of ~0.3 m^2 was constructed in a trailer with the lab-designed multichannel vessels. The zeolite RO demonstration gave an overall 96.9% ion rejection and 2.23 kg/m^2.h water flux for 0.1M NaCl solution. Figure 3 shows a picture of the zeolite RO demonstration established in our laboratory and cross-flow vessels for tubular zeolite membranes.

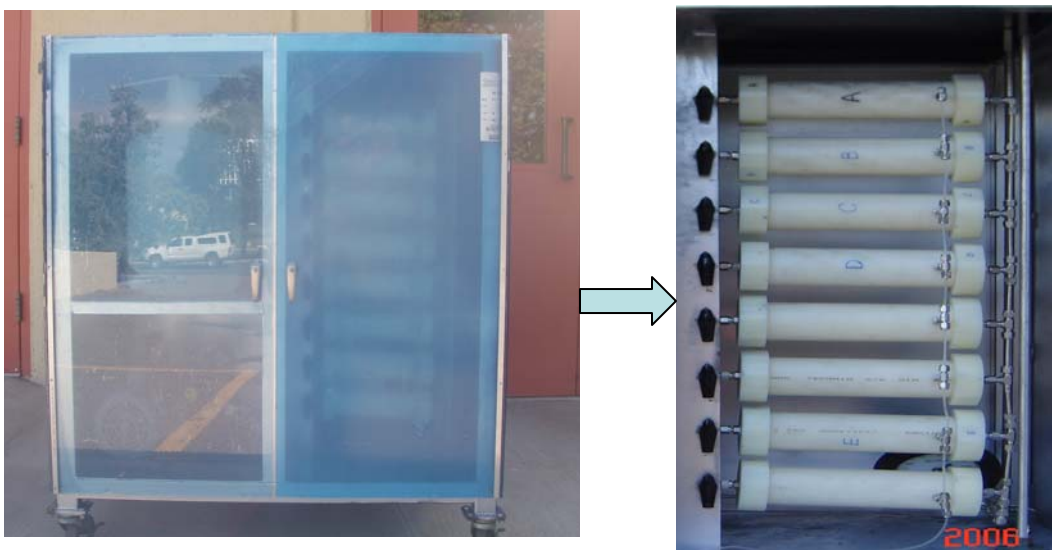

Fig. 3. Reverse osmosis zeolite membrane demonstration.

Long-term desalination of CBM produced water indicated that both water flux and ion rejection declined with elapsed permeation time. The fouling mechanism was

revealed to be scale deposition and organic sorption on zeolite membrane surfaces. Periodic chemical cleaning is suggested to maintain a sustainable separation performance of zeolite membranes.

Conclusions and recommendations

Ion separation by zeolite membranes was first demonstrated by experimental process. Ion separation by zeolite membranes is controlled by size exclusion through intracrystalline zeolitic pores and electrostatic repulsion through intercrystalline pores. The size exclusion through zeolitic pores dominates ion and organic separation mechanism and thus ion separation efficiency is less affected by ionic strength and pH. Operating the zeolite membranes, which possess excellent thermal and mechanical stabilities, at elevated temperatures and high hydraulic pressures is desirable for enhancing the separation efficiency.

Zeolite membranes modified by ion doping show enhanced ion separation efficiency and water throughput. The improvement in water flux and ion separation efficiency is attributed to the strong surface hydrophilicty and surface charge. Long-term permeation indicated that both water flux and ion rejection decline gradually with elapsed operating time. Scale deposition and organic sorption on membrane surface are the main reason for the decline of water permeation. Periodic chemical cleaning is suggested to maintain a stable membrane performance.

Even with the excellent thermal, mechanical stabilities and comparable water flux to polymeric membranes, zeolite membranes are not competitive in seawater desalination due to the expensive substrates. At the very specific condition where polymeric

membranes fail, i.e., a produced water environment, zeolite membranes are more likely be used and will be competitive, with the assumption of 5-year membrane lifetime.

Technology Transfer Efforts

The research of this project has resulted in one pending patent, eight peer-reviewed journal papers, and six conference proceedings. The research findings have also been presented in multiple international conference, including 2007 SPE International Symposium on Oilfield Chemistry, Farmington Carbon Sequestration Southwest Partnership Workshop (Aug. 20, 2006, Farmington), 2004 SPE Annual Meeting at Houston, and the 3th International Zeolite Membrane meeting.

1. INTRODUCTION

1.1. Broader Context of Produced Water Purification

Desalination of brines produced from oil and gas fields is an attractive option for providing potable water in arid regions. At present, more than seven barrels of produced brine are generated for each barrel of oil in the United States; coalbed methane (CBM) produced water is increasing rapidly as CBM production increases [1]. Dissolved salts and organics are the main components that need to be removed in CBM produced water for direct disposal or beneficial use. In addition, recent field-testing of subsurface sequestration of carbon dioxide for climate management purposes provides new motivation for optimizing efficacy of oilfield brine desalination: if subsurface reservoirs are utilized for storing CO_2, the displaced brines must be managed somehow.

The successful handling and utilization of produced water relies on the effective removal of dissolved salts and organics from the water. However, oilfield brine purification is not economical at this time because of the high costs of synthesizing membranes, the need for sophisticated pretreatments to reduce initial high TDS and the lack of prevention for serious fouling of the membranes [2−4]. Novel technology must be developed for all these purposes.

1.2. Zeolite Membranes for Ion Separation

Zeolites are crystalline aluminosilicate materials with well-defined pore structures. Ions could be separated from aqueous solution by zeolite membranes, particularly those with a small pore size, such as A-type and MFI-type zeolites (silicalite or ZSM-5), at a mechanism of size exclusion and electric restriction [5−6]. Their solvent resistance and molecular sieving mechanism allow zeolite membranes to be unique in

separations of both organics and electrolytes from aqueous solutions by reverse osmosis [5], which is of great interest for difficult separations, such as produced water purification.

In aqueous solutions, electrolyte ions exist tightly bound with water due to polar-polar interactions [7]. The diffusivity of ions in an aqueous solution is governed by the crystallographic ion size [8, 9] and the interactions between ions and surrounding water molecules [10]. The mobility and transport behavior of water and hydrated ions in microchannels will be more complicated because of strong interactions between pore surface and ion species [11, 12]. The ionic mobility of hydrated ions in cylindrical pores of radius less than 1.1 nm was reported to be considerably lower than that in bulk solution [13]. The factors governing the structure and diffusion of ion and water in microchannel include surface charge [12], hydrophilicity [14], and pore wall roughness [15]. However, data on ion permeation in zeolite membranes are very limited with regard to furthering insight into the transport mechanism, especially when the hydrated ion size is in the same range as that of the pore diameter [16].

Zeolite membranes synthesized on α-alumina substrate have a negatively charged surface via several mechanisms including ion substitution in the zeolite framework during membrane synthesis [17], dissociation of surface hydroxyl hydrogen [15], and/or ionization of surface hydroxyl groups [18]. When in contact with liquid water or aqueous solutions, an electrically charged double layer forms at the surface of the zeolite pore walls and shows restriction on ion entering and permeation if the double layers are thick enough to overlap at the pore opening. The thickness of the double layer decreases with an increase in ion concentration or in the presence of the membrane's high valence

counter ions (ions with opposite charge as the membrane surface) [19]. The electrostatic exclusion governing ion transport will therefore be strongly dependent on the surface charge of zeolite and the chemistry of the feed solution.

Basic understanding of ion and water transport in microporous zeolite channel is essential to fabricate and modify the material for satisfying the separation requirements. This research targets the ion/water transport in microporous zeolite membranes and fabrication of zeolite membranes for produced water desalination.

1.3. Statement of Work

The proposed research includes experimental studies on the mechanism of the RO process on zeolite membranes, membrane improvement, optimization of operation conditions, and long-term membrane performance. The fundamental studies in Phase 1 included membrane fabrication, mass transport behaviors of water, ions and dissolved organics through the zeolite membranes of varied Si/Al ratios and effects of operation temperature, pressure, feed velocity, feed chemical composition and pH on the RO performance. In Phase 2, research focused on optimizing the RO operating conditions and developing a cost-effective method to repair the undesirable nano-scale intercrystal pores. In Phase 3, a RO unit with a ~0.3-m^2 tubular membrane module has been established to carry out long-term operation test for technical and economic evaluations and system design.

1.4. Layout of the Report

This research aims to develop a new technology of reverse osmosis through molecular sieve zeolite membranes to efficiently treat organic-containing produced water. We have focused on zeolite membrane fabrication, ion/water transport in confined zeolite

micropores, post-synthesis modification, and module design for desalination demonstration.

In Chapters 2 and 3, we introduced the fabrication of zeolite membranes with different Si/Al ratios. Pure silicalite membranes show high ion separation efficiency but low water flux. High water-flux zeolite membranes were synthesized by incorporating aluminum ions into zeolite framework.

In Chapter 4, pore structure of zeolite membranes was investigated by applying HK and BJK model to N_2 adsorption/desorption curve. Study revealed that nanoscale intercrystalline pores (2.0–4.0nm) in zeolite membranes formed on porous support. A smooth surface with random packing of zeolite crystals reduces the density and pore size distribution of intercrystalline pores.

In Chapter 5, a post-synthesis modification method by using Al^{3+}–oligomers for zeolite intercrystalline remediation was developed and considerable enhancement in ion separation was achieved.

In Chapter 6, operating conditions and feed water chemistry have been found to play crucial roles in the ion separation performance of zeolite membranes. Both size exclusion and electrostatic repulsion govern ion permeation through zeolite membranes. However, size exclusion dominates the separation process.

In Chapters 7 and 8, ion and water permeation through zeolite membranes was experimentally investigated. A mathematical model for describing ion/water permeation through thin zeolite film has been developed.

In Chapter 9, a zeolite RO demonstration with membrane surface area of ~0.3m^2 has been established. Ways to upscale the fabrication of zeolite membrane for industry implementation is discussed.

In Chapter 10, CBM produced water desalination by zeolite membranes was tested for prolonged times. Membrane fouling and remediation during long-term produced water desalination was investigated.

In Chapter 11, engineering aspects of application of zeolite membrane for produced water purification are discussed. Economic evaluation suggests that the high cost of membrane substrates is the primary obstacle for upscale application of this technology to water desalination. However, zeolite membranes will be competitive in specific applications where conventional polymeric membranes fail.

2. SYNTHESIS OF PURE SILICALITE ZEOLITE MEMBRANES

MFI-type zeolite membranes were synthesized through two techniques: (1) in-situ crystallization, and (2) seeding and second growth method. In-situ crystallization is carried out by immersing porous substrate into a synthesis solution containing organic templates function as a structure directing agent, such as tetrapropylammonium hydroxide (TPAOH). Membranes synthesized by in-situ crystallization need to be heat-treated to remove the template (TPAOH) and open zeolite pores for mass transport. In the second growth technique, a seeding layer of synthesized silicalite nano particles (average dia. ~100 nm) was first coated onto the polished surface of substrates by conventional dip-coating technique. After drying and firing at 450°C, a secondary growth step was conducted in a solution without template. Zeolite membranes formed thereafter had an open pore structure and did not need firing for template removal.

2.1 Porous alpha-alumina support

Alumina substrates with different geometry were deployed for membrane fabrication in this study, including disc-shaped and tubular substrates. The tubular substrates (pore dia. 0.2 μm) were purchased from Pall Inc. Tubular substrates with length of 8.0 cm and 25 cm both have an ID of 7.4 mm and OD of 10 mm. Porous α–alumina disks with thickness of 3.0 mm and diameter of 28 mm were fabricated in our laboraty by pressing commercial α-alumina powders and sintering at 1150°C. The α-alumina powders used for substrate preparation were provided by Alcoa (lot# 4422603, mean particle size 0.44 μm). Figure 4 shows these α-alumina substrates for zeolite membrane coating.

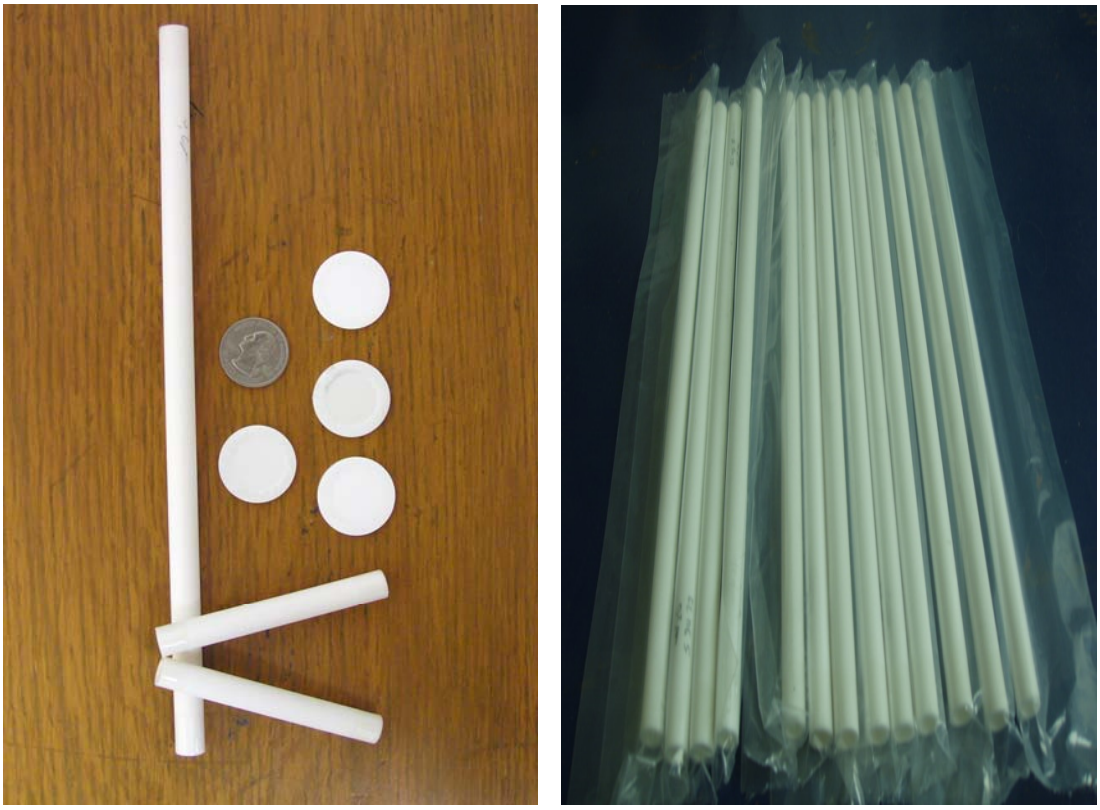

Fig. 4. Alpha-alumina substrate for zeolite membrane fabrication with different dimensions.

Tubular membrane synthesis was carried out in a stainless steel vessel lined with Teflon. A lab-constructed rotation system was designed and constructed to rotate the stainless steel autoclave for homogeneous nucleation. The tubular membranes were wrapped outside with Teflon tape and rotated at a constant rate of 1.5 rad/min during hydrothermal crystallization. Disc-shaped zeolite membranes were synthesized by in-situ crystallization at static state. Figure 5 gives the diagram of the membranes synthesized at static and rotation conditions.

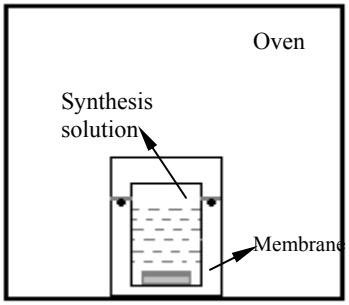

(b) Static synthesis cell

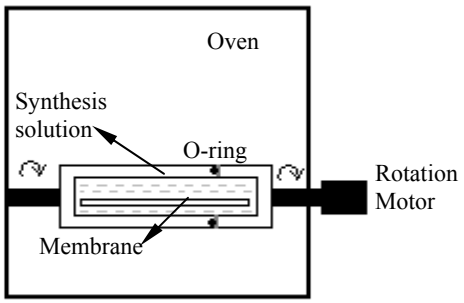

(b) Rotating synthesis system

Fig. 5. Schematic diagram of membrane synthesis reactor.

2.2 Equipment and membrane characterization

Fumed silica (99.8%, Aldrich), sodium hydroxide (99.99%, Aldrich), tetraethyl orthosilicate (TEOS, 98%, ACROS Organics) and TPAOH (1.0 M, Aldrich) were used for the membrane synthesis. Hydroxypropyl cellulose (HPC, M_w=100,000, Aldrich) was used as a binder for dip-coating to avoid crack formation during sintering and 0.1 M nitric acid (0.998 M, Aldrich) was used to adjust the pH value of the coating suspensions. Other chemicals used in this study include sodium chloride (analytical reagent, Riedel-deHaen), potassium chloride (analytical reagent, J. T. Baker), calcium chloride (biotech grade, FisherBiotech), aluminum chloride (>99.0%, ACROS), sodium bromide (>99.0%, ACROS), and sodium sulfate $Na_2SO_4^{2-}$ (>99.0%, Alfa Aesar®).

The membrane was examined by X-ray diffraction (XRD, Siemens D-500) with Cu k_α radiation. The membrane thickness and surface morphology were studied with a scanning electron microscope (SEM, JEOL 5800LV). All the SEM samples were coated with gold before analysis. Zeolite morphology and membrane thickness were investigated by scanning electron microscope (SEM, JEOL 5800LV). Chemical composition of the

zeolite membranes was verified by microscope (Cameca SX-100 with SPARC-5 workstation).

2.3. Membrane synthesis by in-situ crystallization

The disc-shaped substrate for membrane growth was first polished with 320-mesh silicon carbide paper and then with 600-mesh. The tubular porous substrate was used as received.

The in-situ crystallization of MFI-type zeolite membranes by hydrothermal synthesis was conducted at 180°C and autogenous pressure in an autoclave. The synthesis solution was prepared by dissolution of 5.0 g fumed SiO_2 and 0.35 g NaOH into 25 mL TPAOH (1.0 M) solution at 80°C. The substrate was immersed in the solution in a 30 mL Teflon-lined autoclave. The autoclave was closed with O-ring sealing and put in a preheated oven at 180°C for 4 hr for crystallization. After hydrothermal treatment, the membranes were recovered and washed with DI water and immersed in a large quantity of DI water for 24 hr to remove ions trapped in the membrane and substrate. The membrane was then dried at 50°C overnight. The silicalite membranes were calcined at 450°C in air for 8 hr to remove the template (TPA^+). The calcination used a heating rate of 0.5°C/min and a cooling rate of 1.0°C/min. The same synthesis procedure was repeated once to minimize the intercrystalline gaps. Figures 6 and 7 give the SEM images of zeolite membrane synthesized on disc-shaped substrate once and twice, respectively. The membrane thickness increased from ~1.5 μm to ~3 μm after the second synthesis process. The zeolite crystal sizes increased from ~0.3 μm to ~1.0 μm, indicating the crystal growth during the second crystallization process.

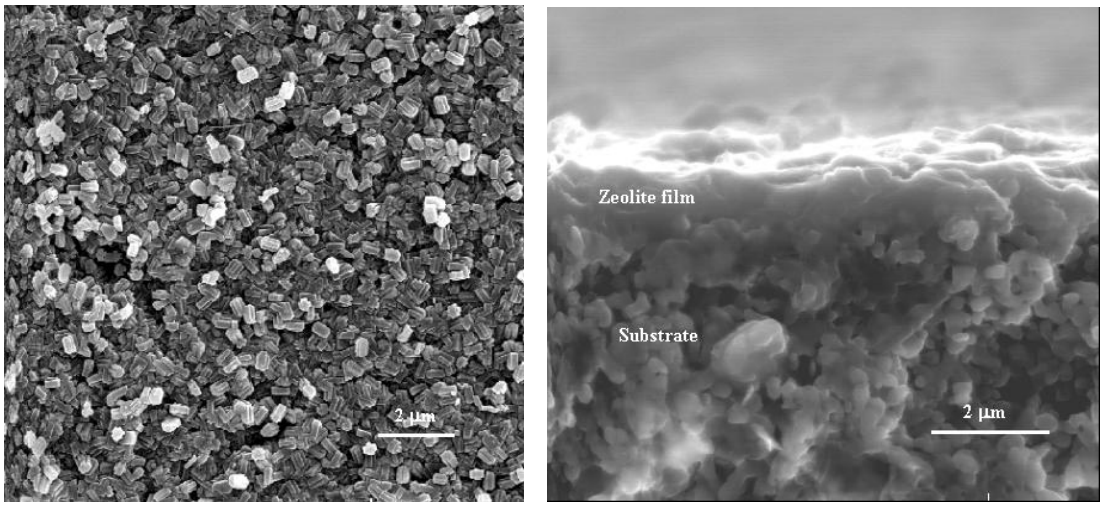

(a) Surface (b) Cross-section

Fig. 6. SEM images of zeolite membrane synthesized by single in-situ crystallization.

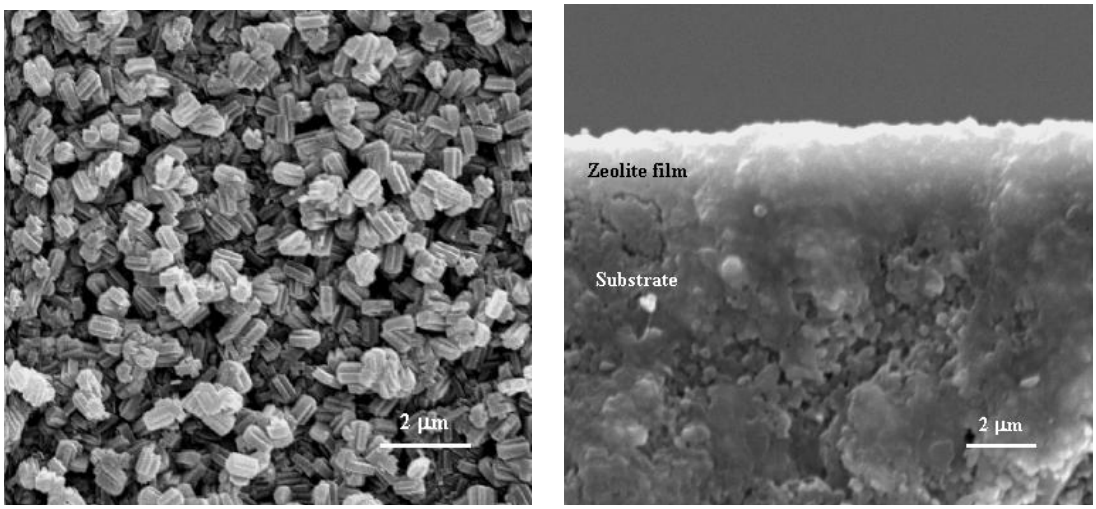

Fig. 7. SEM images of zeolite membrane synthesized by double in-situ crystallization.

The X-ray diffraction patterns of the zeolite membranes obtained by single and double in-situ crystallization are shown in Fig. 8 together with the patterns of the alumina substrate and standard MFI silicalite powders. The XRD patterns verified that the membranes had a crystal structure of pure MFI-type zeolite. The increase in relative

intensity of the zeolite XRD peaks after the second hydrothermal synthesis also indicated the growth of zeolite film thickness.

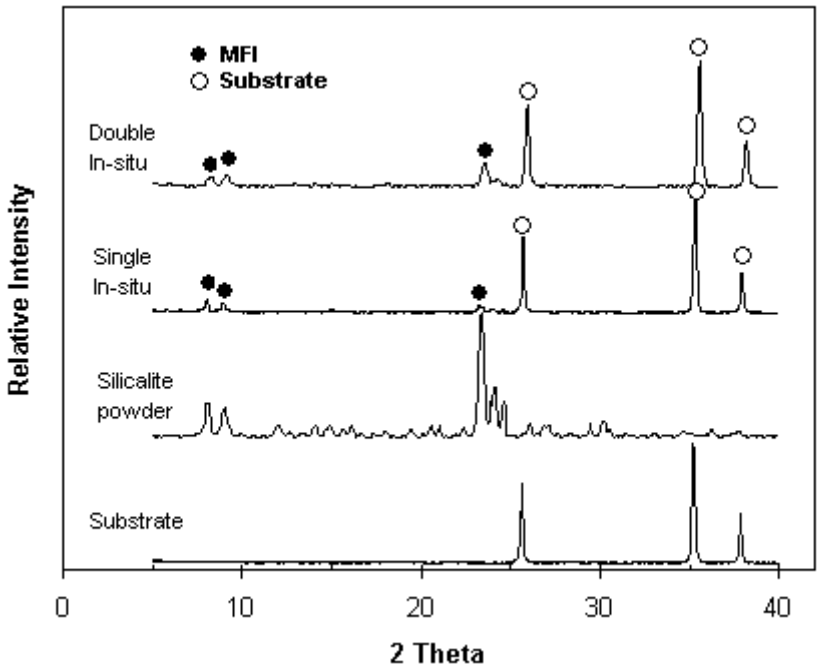

Fig. 8. XRD patterns of MFI zeolite membranes synthesized by single and double in-situ crystallization.

The synthesis of tubular membranes was performed in a Teflon-lined autoclave, which was constructed in our laboratory for a constant rotation. The synthesis solution and crystallization condition is the same as that of the disc-shaped membranes except that the synthesis time was extended to 20 hr. After membrane synthesis, the zeolite membranes were rinsed and dipped into a large quantity of deionized (DI) water for cleaning. After drying at 45°C for two days, the membrane was fired at 450°C for 8 hr to remove the organic template. The synthesis was also repeated once to eliminate zeolite intercrystalline pores. The zeolite membrane synthesized therein had a thickness of ~2

μm as measured by scanning electron microscopy (SEM), slightly thinner than that formed in static condition.

2.4. Membrane synthesis by seeding and second growth

Fabrication of zeolite membranes by second growth was also investigated in this research; a zeolite thin film was first formed by coating silicalite nanocrystalls on porous support and then a second growth was carried out to form a defect-free zeolite film for separation. The nanosized silicalite crystals with diameter of ~100 nm were synthesized from a solution identical to the sol used for the in-situ crystallization. The crystallization was carried out at 120°C for 12 hr. The seeding crystals were purified by repeated centrifuge until the conductivity of supernant was below 10 μs/cm. Dip-coating was applied to form a thin seeding layer on porous α-alumina substrates. In the dip-coating process, zeolite suspensions were mixed with HPC binder in a controlled weight ratio. Next, 0.1 M nitric acid was added dropwise to adjust the pH to desired value. The pH value, zeolite composition and binder concentration were varied to optimize the coating condition for uniform coating layer formation. A good seeding film was obtained by coating with a suspension of 0.6% seeds and 0.05% HPC, at a pH of 3 to 4. After coating, the seeded support was dried in an oven at 45°C in a controlled humidity (~60%) for 48 hr. Then, the support was fired at 450°C for 8 hr to remove the organic template and enhance the adhesion between the coated seed layer and the substrate. Figure 9 gives the SEM image of a coated zeolite film.

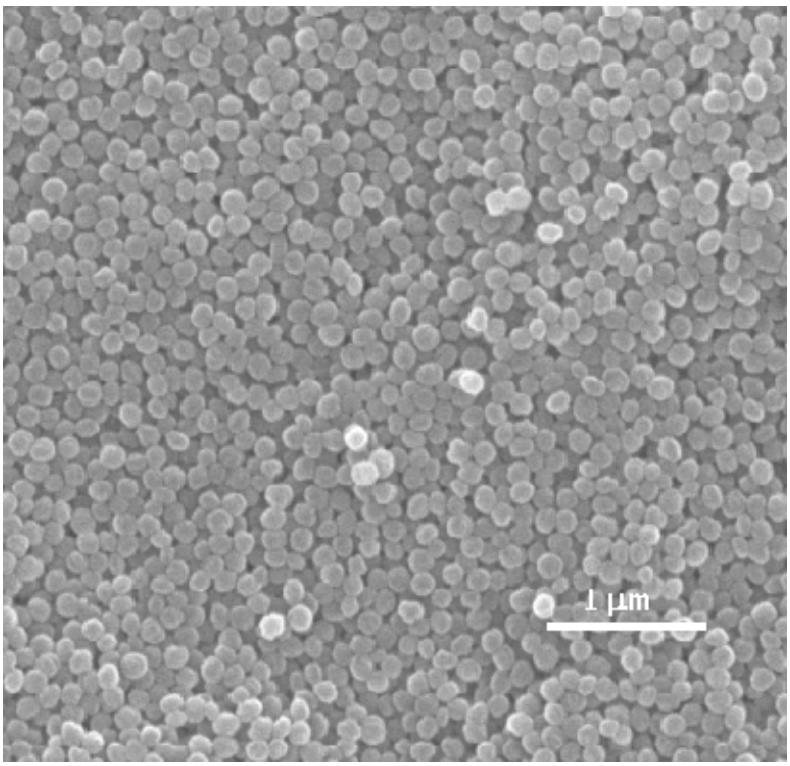

Fig. 9. SEM images of zeolite seeding layer on α-alumina substrate.

A second growth synthesis solution with molar composition of 1.0 TPAOH: 4.5 SiO_2: 550 H_2O: 18 EtOH was prepared by dissolution of TEOS and TPAOH (1.0 M) into DI water at 50°C for 12 hr. Following the preparation of the synthesis solution, the seeded support was mounted in a Teflon holder with the coated side facing down and immersed in the synthesis solution in Teflon-lined autoclave. The autoclave was closed and put in a preheated oven at 180°C for 6 hr. In the hydrothermal condition, the seeded zeolite crystals grow to form continuous layer on the support. After synthesis, the membrane was rinsed with DI water and fired at 450 °C for 8 hr. Figures 10 and 11 give the surface and cross-section of SEM images of the zeolite membrane synthesized by second growth. The zeolite membrane synthesized with above procedure has a thickness of ~1.5 μm as revealed by SEM images.

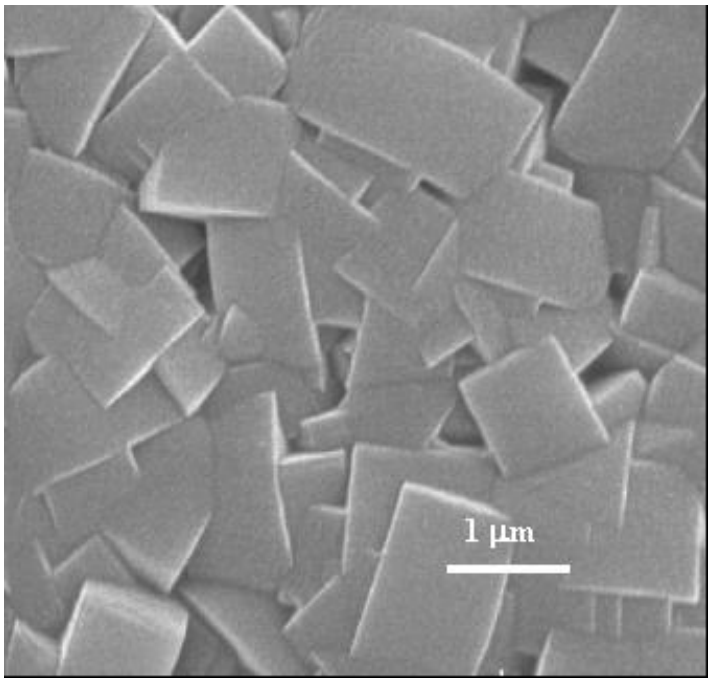

Fig. 10. Surface SEM image of zeolite film synthesized by second growth.

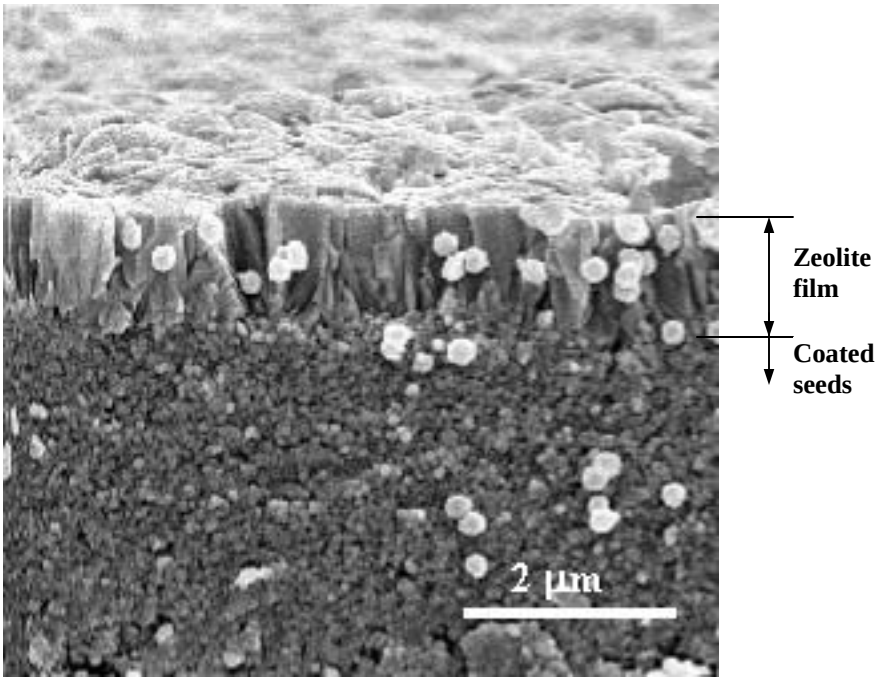

Fig. 11. SEM image of Cross-section of zeolite membranes synthesized by second growth.

3. SYNTHESIS OF HIGH-ALUMINUM ZEOLITE MEMBRANES FOR ENHANCED WATER PERMEATION

Pore network and surface chemistry are the principal properties by which a membrane controls the permeability of different species and achieves separation. The material chemistry (i.e. Si/Al ratio) plays an important role on the membrane charge and surface wettability and thus water permeation because water transport in confined spaces, such as micropores, whose pore sizes are in the range of intermolecular forces, is strongly dependent on the surface wettability and pore wall roughness [15, 20]. The understanding of the dynamics of ion and water entrance into zeolite pores and interaction between ion and water in zeolite micropores will be crucial to tailor the membrane structure for enhanced water flux and ion separation efficiency.

Water wettability on a zeolite surface is mainly determined by the aluminum content of the zeolite framework and extraframework counterions [21]. Zeolite membranes with high Si/Al ratios, such as pure silicalite-1 membranes, exhibit hydrophobic separation behavior [22; 23]. As aluminum ions are incorporated into the zeolite framework, more hydroxyl group forms on the membrane surface [24], resulting in a higher tendency to adsorb water molecules [25]. Also, the substitution of Si^{4+} by Al^{3+} in the zeolite framework creates a large-density surface charge, which is usually balanced by small cations (i.e. Na^{+} and Ca^{2+}) [25]. The extra framework cations present in the pores can coordinate with water molecules and enhance the water affinity on the zeolite surface. The high surface charge created by ion substitution will form strong surface potential when in contact with aqueous solution. A double layer will form and overlap in

the intercrystalline pore region, showing restriction on ion entering and permeation and enhance the ion separation efficiency.

In the work described in this chapter, MFI-type zeolite membranes with large variations in Si/Al ratio were synthesized on porous α-alumina supports by seeding and secondary growth. The influence of chemical composition on the surface zeta potential and water wettability as well as on RO separation was investigated. The water permeation behavior in confined spaces (i.e. zeolite micropores) was further analyzed.

Considering the commonly encountered problem of poor reproducibility in zeolite membrane synthesis [26,27], the variation in ion rejection of zeolite membranes synthesized in this work is within a reasonable range.

3.1 Process of ZSM-5 membrane fabrication

ZSM-5 membranes were synthesized by seeding and secondary growth on disc-shaped α-Al_2O_3 substrates. The substrates were made in the laboratory with a diameter of 28 mm and thickness of 4 mm. The substrate surface for seed coating was polished with 600-mesh sand paper. Coating the substrate surface with a layer of silicalite seeds of about 60 nm was carried out by dipping the substrate into a seed suspension contain 0.5% silicate and 0.05% hydroxypropyl cellulose (HPC, M_W=100,000, Aldrich) for 3 sec. The pH of the coating suspension was adjusted to ~3 by adding 0.1 M HNO_3 by drops. The seeded substrates were dried at 45°C for two days and calcinated at 450°C for 6 hr to remove the organic template. The seeding process was repeated one time to obtain better surface coverage. The nanosized silicalite seeds were synthesized from a solution

containing 0.35 g NaOH pellets (>99.99%, Aldrich), 5.0 g fumed SiO_2 (particle size 0.014 μm, Aldrich), and 25 ml 1.0M TPAOH (Aldrich) at 60°C for 14 days.

Following the substrate seeding, a second growth was performed to form a continuous zeolite layer on the seeded substrate. The second growth synthesis solution was prepared by dissolving fumed silica and NaOH pellets into deionized water at 80°C. When a clear solution was obtained, a measured amount of $Al_2(SO_4)_3 \cdot 18H_2O$ (>98%, Aldrich) was added and stirred at room temperature for 12 hr. The seeded substrate was placed in a Teflon-lined autoclave with the coated surface facing down and the synthesis solution was poured in to immerse the substrate. The autoclave was sealed and moved to a preheated oven at 180°C for 6 hr. After synthesis, the membranes were rinsed with deionized water and dried at 150°C for the RO permeation test.

As described in the last chapter, random surface searching of SEM images of seeded substrated indicated that the whole surface was covered by zeolite crystals with diameter of 60–100 nm. However, high densities of interparticle pores and a dome-like structure of the coating layer were observed due to random packing of the zeolite crystals on the porous support.

After the template was removed by calcination at 450°C for 6 hr, the seeded substrate was immersed in a synthesis solution containing 1.0 SiO_2+41.5 H_2O+ 0.38 NaOH +0.0076 Al_2O_3 for secondary growth. The crystallization time was varied to improve the intergrowth and surface coverage for achievement of high separation performance.

Figure 12 shows top-view SEM images of ZSM-5 membranes synthesized from 6 hr to 12 hr. All zeolite membranes synthesized at 180°C for 6 hr or longer show good

surface coverage. As synthesis time increased, large crystals formed and embedded in the growing zeolite layer, resulting in higher surface roughness as shown in Figures 12 (b) and (c). Crystal growth of MFI-type zeolite crystals during secondary growth was confirmed by X-ray study as shown in Figure 13.

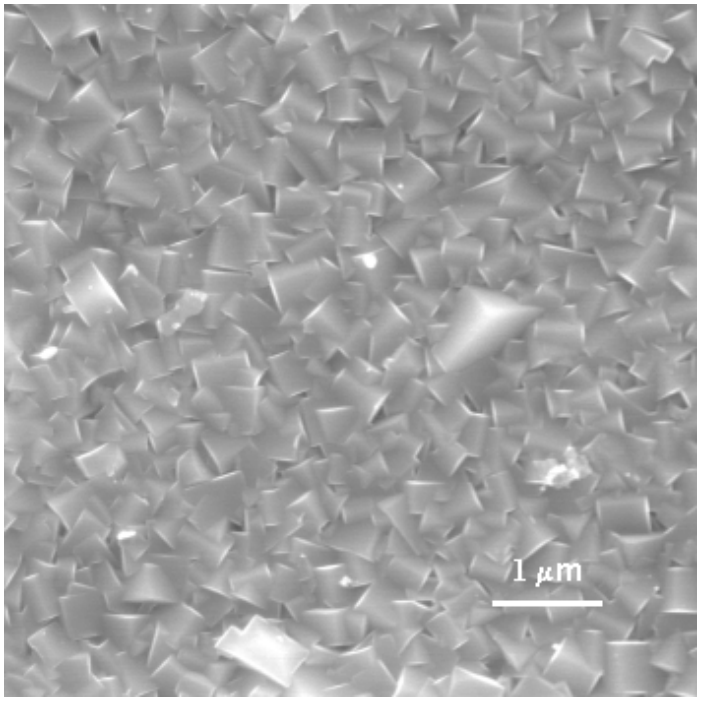

(a) 6 hr

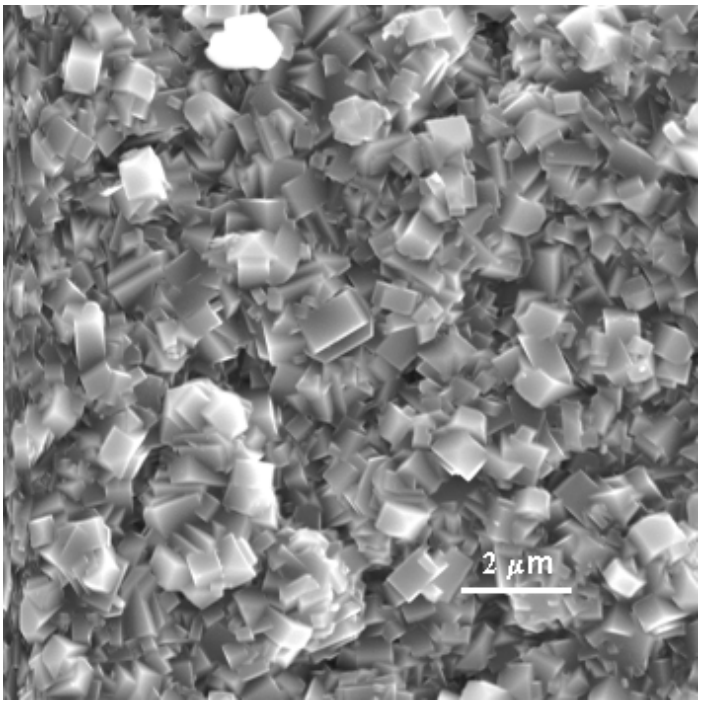

(b) 9 hr

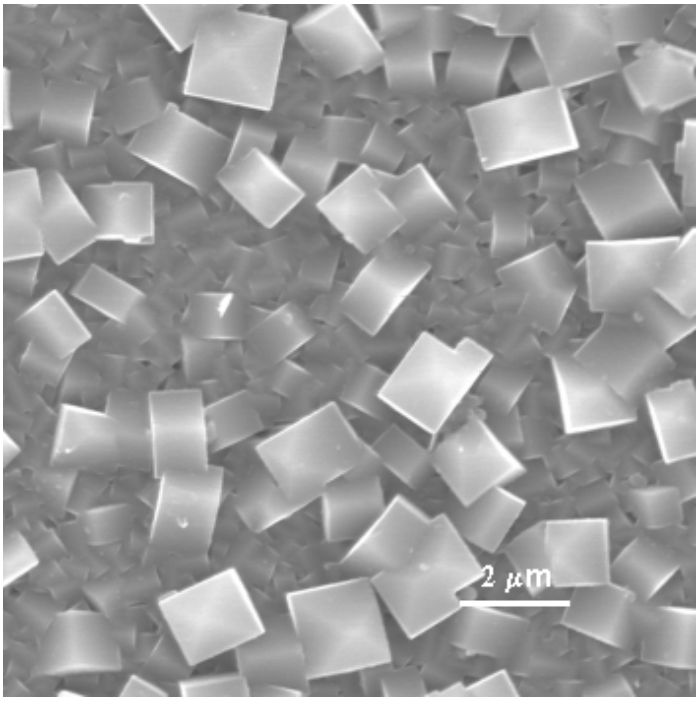

(c) 12 hr

Fig. 12. Effect of synthesis time on membrane morphology.

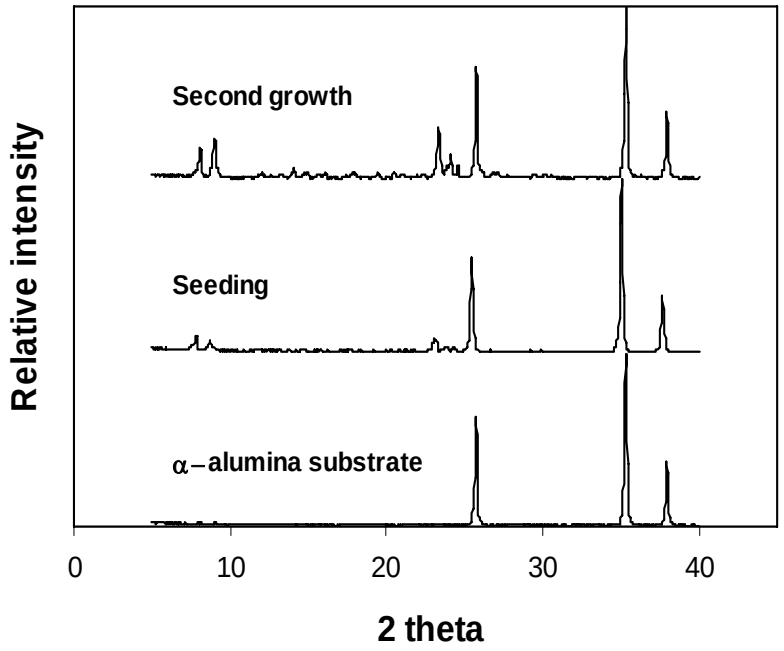

Fig. 13. The XRD pattern of a zeolite film synthesized by seeding and secondary growth.

Alkalinity in the synthesis solution is crucial for zeolite nucleation and growth, especially in the absence of the organic template, because the Na^+ essentially functions as the structure directing agent [28]. Also, the alkalinity will affect the dissolution of SiO_2 species in the synthesis solution and thus the zeolite crystallinity during zeolite crystallization [29]. In this study, zeolite membranes with good surface coverage were synthesized from solutions having a wide range of alkalinity. Figure 14 shows the surface images of zeolite membranes synthesized from solutions having $NaOH:SiO_2$ ratios (x) of 0.32 and 0.48, respectively. Comparing these to the SEM image shown in Figure 12 (a) (x=0.38), it can be seen that increasing solution alkalinity promotes the zeolite crystal growth and forms large zeolite crystals and rough membrane surface.

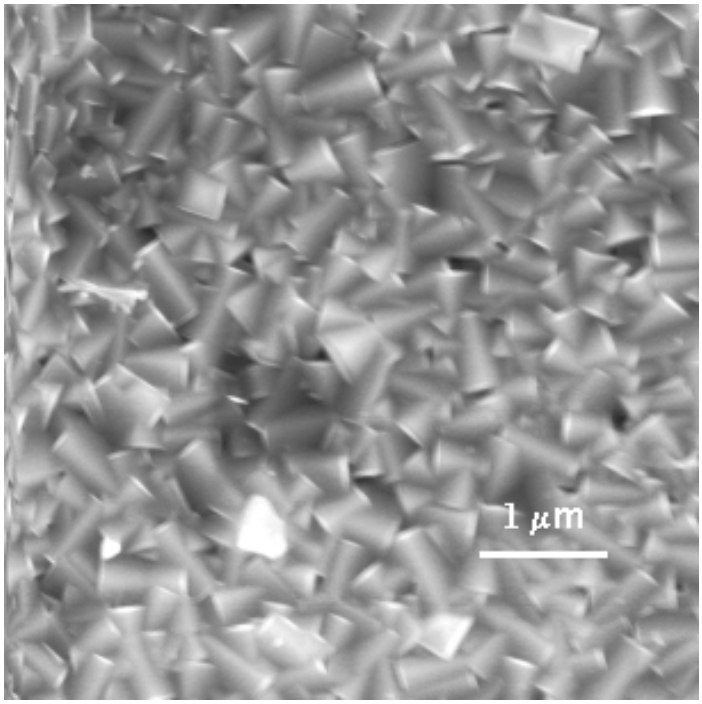

(a) x=0.32

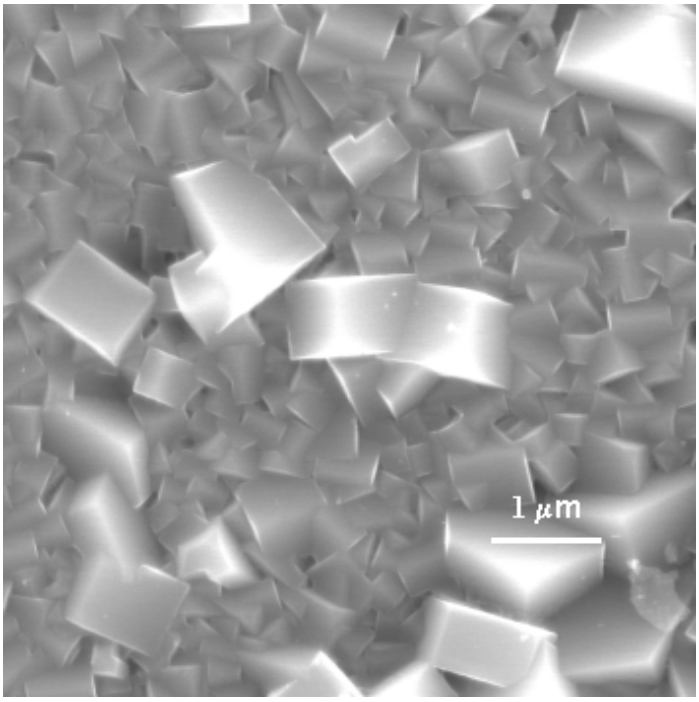

(b) x=0.48

Fig. 14. SEM images of ZSM-5 membranes synthesized from solutions with different alkalinities (1.0 SiO_2+41.5 H_2O+ x NaOH +0.0076 Al_2O_3).

Figure 15 gives SEM images of the surface of zeolite membranes synthesized from solutions containing different Si/Al ratios. The presence of aluminum ions in the synthesis solution affects membrane morphology and crystal shape. Membranes synthesized from an aluminum-free solution preserve the characteristic coffin shape of zeolite crystals (Figure 15 (a)). High density of pin holes between crystal boundaries were observed on the pure silicalite membranes synthesized by secondary growth. As aluminum ions were incorporated into the zeolite framework, considerable twinning growth was observed as shown in Figures 15 (b) and (c). The twining growth eliminates most of the pinholes by promoting the intercrystalline growth. Such an observation was reinforced by xylene isomer (p-xylene and o-xylene) separation, which indicated that zeolite membranes synthesized from solutions containing aluminum ions would show molecular sieving on xylene isomers ($\alpha_{p-xylene/o-xylene}$=2.3). The xylene isomer separation was carried out at 300°C with a procedure described in the literature [30].

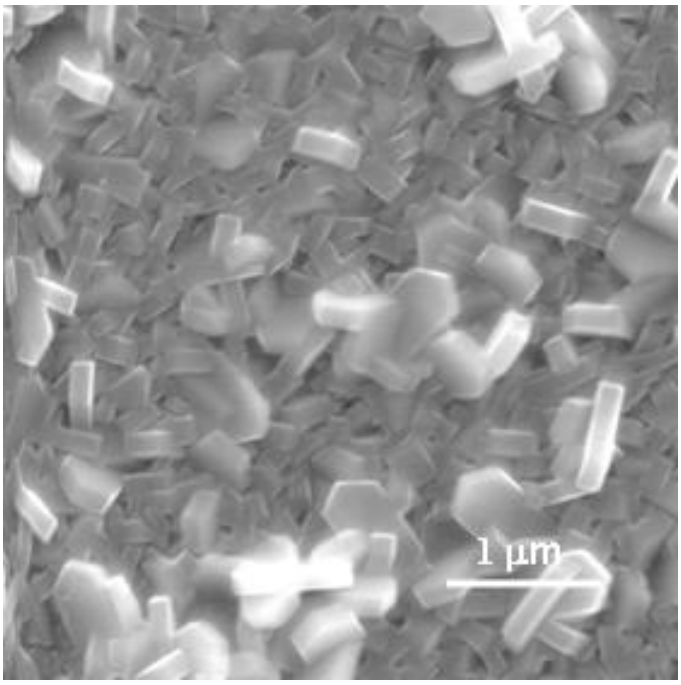

(a) Si/Al=~∞

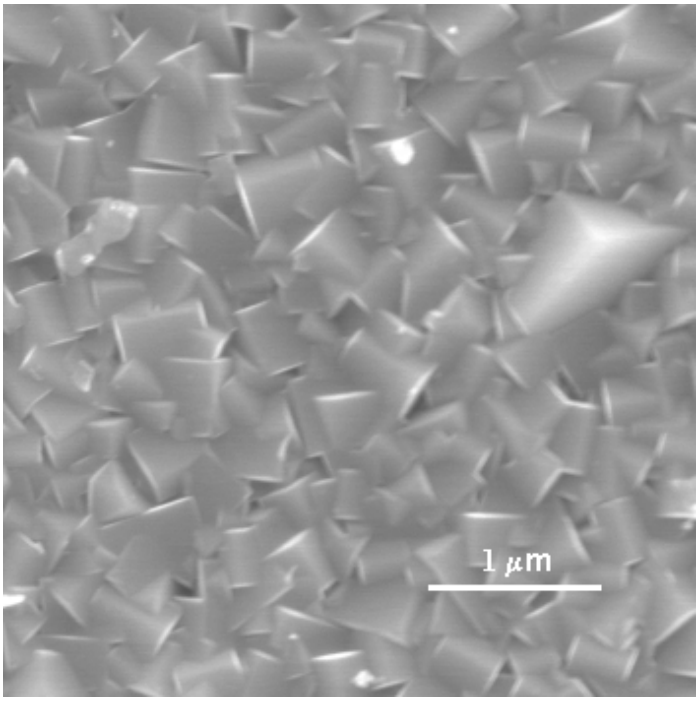

(b) Si/Al=65

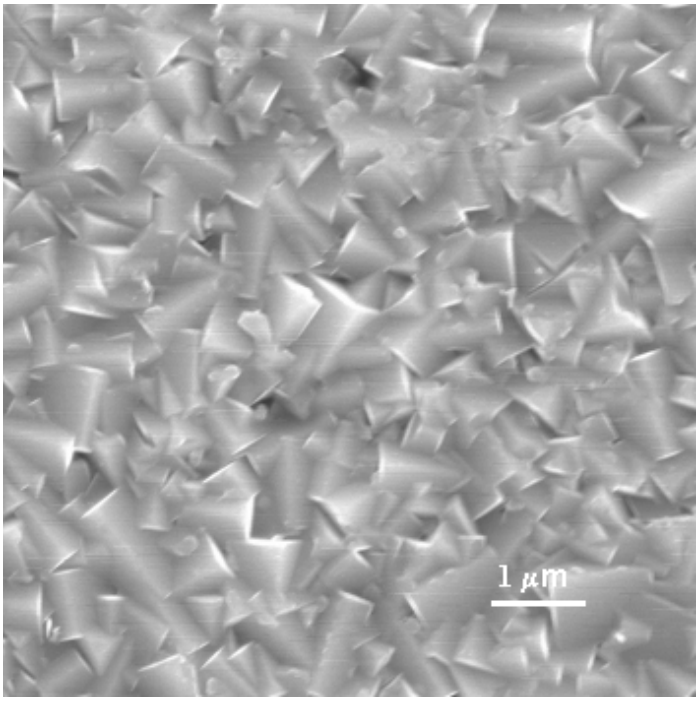

(c) Si/Al=50

Fig. 15. Effect of Si/Al ratio on zeolite membrane morphology (1.0 SiO_2+41.5 H_2O+ 0.38 NaOH + x Al_2O_3).

Figure 16 gives the cross-section SEM images of the seeded substrate before and after the secondary growth. To increase the surface coverage, dip-coating was repeated once and the seeding layer formed therein had a thickness of 0.5~1.0 μm. The second growth was carried out at 180°C for 6 hr. The membrane synthesized in that condition had an overall zeolite thickness of ~2.5 μm, giving an effective membrane thickness of ~2 μm.

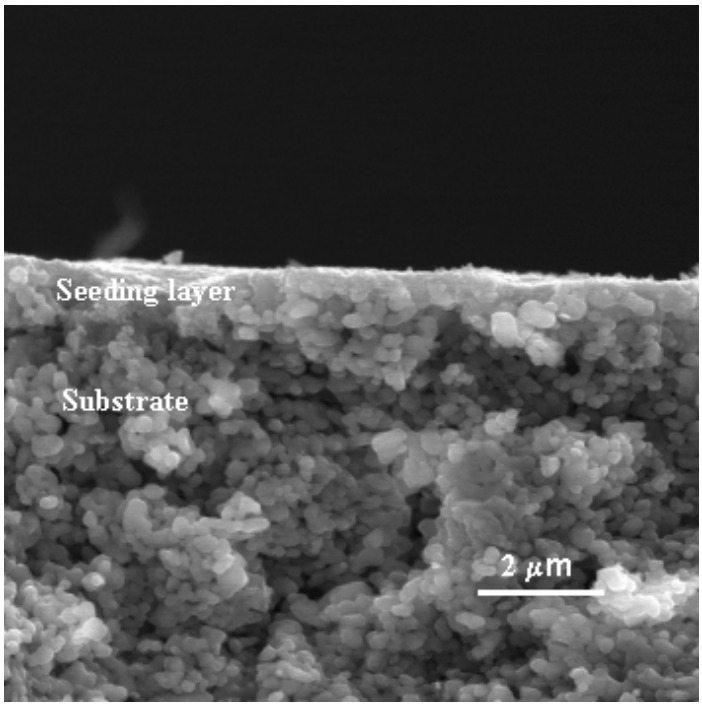

(a) Zeolite seeding layer

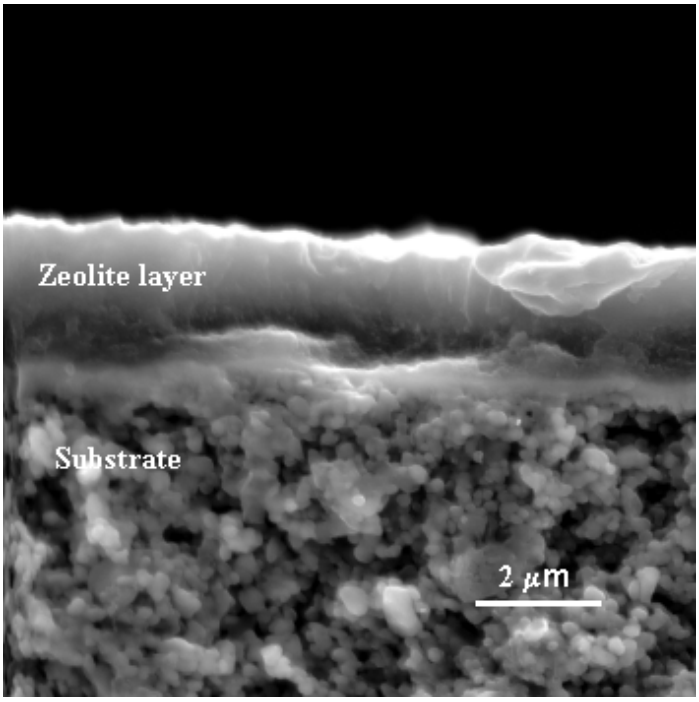

(b) ZSM-5 membrane

Fig. 16. SEM images of cross-section of seeded substrates before and after the second growth (Si/Al=65).

3.2 Surface chemistry and ion separation

The surface hydrophilicity of the zeolite membranes with different Si/Al ratios was determined by contact angle measurement (OCA 30, FDS Inc.) using sessile and captive drop methods. The surface charges of the zeolite membranes were estimated from the zeta potential measurement of zeolite particles synthesized from the same solution. Zeolite particles with an average particle size of 120 nm were diluted to ~0.05% in a 0.01 M NaCl solution and the zeta potential was measured by DELSA 440SX (Coulter).

Ion separations were performed with a cross-flow RO permeation setup. The feed side was connected to a pressurized solution tank containing NaCl solutions; the desired trans-membrane pressure was maintained by a high-pressure nitrogen cylinder. A

constant feed flow rate of 1.0 mL/min was controlled through a needle valve located at the concentrate side. The permeate, defined as the solution transport across the membrane, was collected every 12 hr and stored at 5°C for further composition analysis. The NaCl concentrations in both the feed and the permeate sides were analyzed by ion chromatograph (IC, DX120, Dionex).

Each RO test lasted for ~80 hrs for achievement of stabilized water flux and ion rejection. Water flux (F_w) and ion rejection (r_i) are two important parameters in the RO membrane process.

Table 1 gives the RO separation results for 0.10 M NaCl solution on ZSM-5 membranes synthesized from solutions with Si/Al ratios ranging from 40 to 65. For comparison, RO permeation of 0.10 M NaCl solution on a pure silicalite membrane was also given in Table 1. The silicalite membrane was synthesized by in-situ crystallization with a procedure reported the previous chapter.

Table 1. RO permeation of 0.10 M NaCl solution on MFI zeolite membranes with different Si/Al ratios (P=2.76 Mpa)

No.	Si/Al Ratio	Membrane thickness, μm	Na^+ rejection, %	Water flux, $kg/m^2.h$	Permeability mol/(m.h.kPa)	Remarks
M-1	40	~2	81.8	1.416	5.70×10^{-8}	2th growth
M-2	50	~2	92.9	1.129	4.55×10^{-8}	2th growth
M-3	65	~2	91.5	0.527	2.12×10^{-8}	2th growth
M-4	~∞	~3	90.6	0.112	6.76×10^{-9}	In-situ

Pure silicalite membrane synthesized by in-situ crystallization gives an ion rejection of 90.6% and water flux of 0.112 $kg/m^2.h$ at an operating pressure of 2.76 MPa. Both water flux and ion rejection increase considerably as small amount of aluminum

ions were substituted into zeolite structure, with water flux increase from 0.112 kg/m^2.h to 1.129 kg/m^2.h and ion rejection enhancement from 90.6% to 92.9%. However, as aluminum content increased further (i.e. Si/Al=40), ion rejection declined because of poor zeolite crystallinity. The nearly onefold increase in water flux of ZSM-5 membranes is attributed to the reduced membrane thickness and enhanced surface hydrophilicity. As trivalent cations (Al^{3+}) are progressively incorporated into zeolite framework, a high-density hydroxyl group forms and enhances the affinity of water molecules with the membrane surface [22]. Also, extra-framework counter ions (i.e. Na^{+}, and Ca^{2+}) can coordinate to water molecules, enhancing water affinity on the membrane surface. The thickness-independent permeabilities calculated in Table 1 clearly show the enhancement in water permeation for high aluminum ZSM-5 membranes. The water affinity on the membrane surface was qualitatively studied by contact-angle measurements. The membrane samples were tested as received to simulate the actual membrane preparation process. Because water droplets spread rapidly on membrane surface, the images were taken 30 sec after the water droplet touched the membrane surface. Figure 17 gives the contact angle measurement results of zeolite membranes with increasing aluminum contents. The pure silicalite membrane shows a weak hydrophilic property with a contact angle of ~30°, which is consistent with the literature result [31]. Such an observation is explained by the dissolution of trace aluminum elements from the α-alumina substrate in the strong basic synthesis solution and their incorporation into the zeolite structure [23]. As the aluminum content increased, the contact angles were below 5° as shown in Figs. 17(b) and (c), indicating strong hydrophilic characteristic of the membranes.

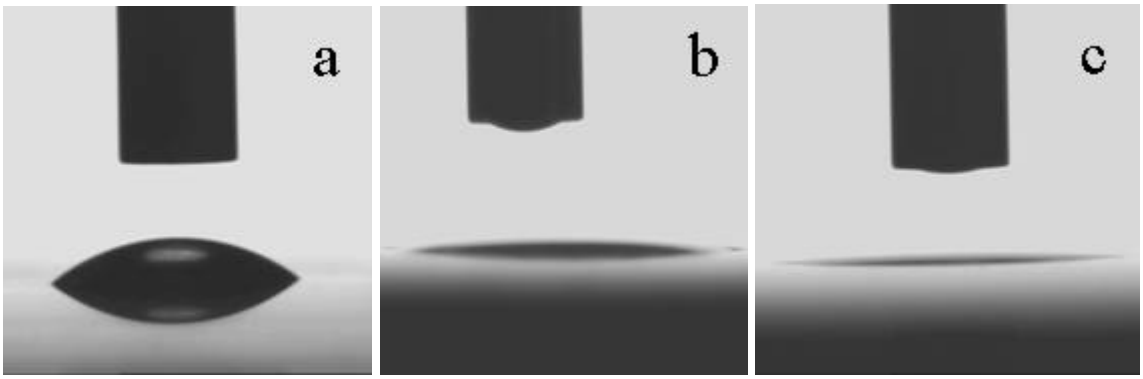

Fig. 17. Contact angle measurement of zeolite film on porous support: (a) silicalite, (b) Si/Al=65, (c) Si/Al=50.

Zeolite membranes synthesized from a wide range of aluminum content show high ion rejection for 0.10 M NaCl solution (r_i>90%). Both the xylene isomer separation and gas permeation study indicated that zeolite membranes synthesized from an aluminum-containing solution have poor intercrystalline growth [32]. It is more likely that the enhancement in ion rejection for ZSM-5 membranes is caused by strong surface charge rather than the molecular sieving [33]. The surface charge of zeolite membranes was estimated from zeta-potential measurement of zeolite nanoparticles synthesized from the same solution as that of the membranes. Figure 18 gives the zeta potential of nanocrystalline zeolite particles as a function of aluminum content. The trace element of aluminum ions (Si/Al=200) resulted in a high increase in surface ζ-potential, from -4.7 to -49.2 mv. As aluminum content increased further (i.e. Si/Al=65), surface zeta potential increased gradually to -54.7 mv. The further increase of aluminum contents (Si/Al=50) resulted in a leap in zeta potential to –76.2 mv. In contacting with aqueous solution, a double layer will develop and overlap in the intercrystalline pore region and restrict ion entrance and transport. The double layer thickness monotonically increases with increase of surface potential, [34], with the result that more intercrystalline pores are

permselective when high concentrations of aluminum ions are incorporated into a zeolite framework.

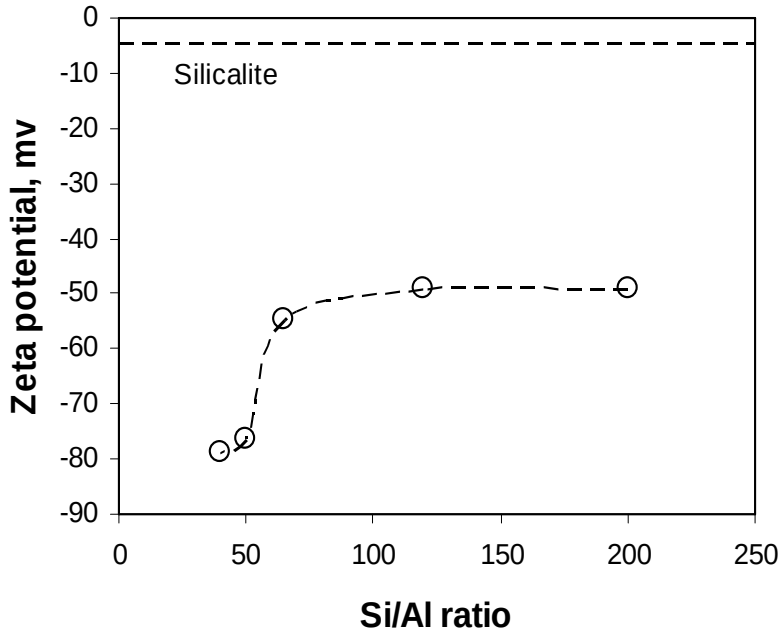

Fig. 18. Zeta potential of zeolite particles with different Si/Al ratios at 0.01 M NaCl solution.

3.3. Presence of aluminum ions on ion separation performance

Figures 19 and 20 give the pressure-dependent water flux and ion rejection of zeolite membranes with Si/Al ratios ranging from 50 to infinity (pure silicalite). Increasing operation pressure leads to a linear increase in water flux. Ion rejection, on the other hand, increases initially and then levels off with an increase in operating pressure. Ions permeate through zeolite membrane by two mechanisms: (1) surface diffusion and (2) transport through intercrystalline pores where double layer can not overlap [6]. In a micropore with structure similar to pure silicalite zeolite membranes, ions and water prefer to stay in the center of the microchannels and ion permeation by surface diffusion is negligible [10]. When aluminum ions are incorporated into a zeolite structure, the

framework is anionic with its charge balanced by extraframework cations. Such changes in zeolite structure will enhance ion permeation through surface diffusion while hindering ion transport from intercrystalline pores because of the high ion surface coverage and increased double layer thickness [35]. At low operating pressures, zeolite membranes with higher aluminum contents show lower ion rejection because of the large contribution of ion permeation through surface diffusion. As transmembrane pressure increases, water permeation increases faster than do ions [16], resulting in enhanced ion rejection efficiency. The increase in ion rejection with operating pressure is more significant when high aluminum ions are incorporated into zeolite framework, as shown in Figure 20.

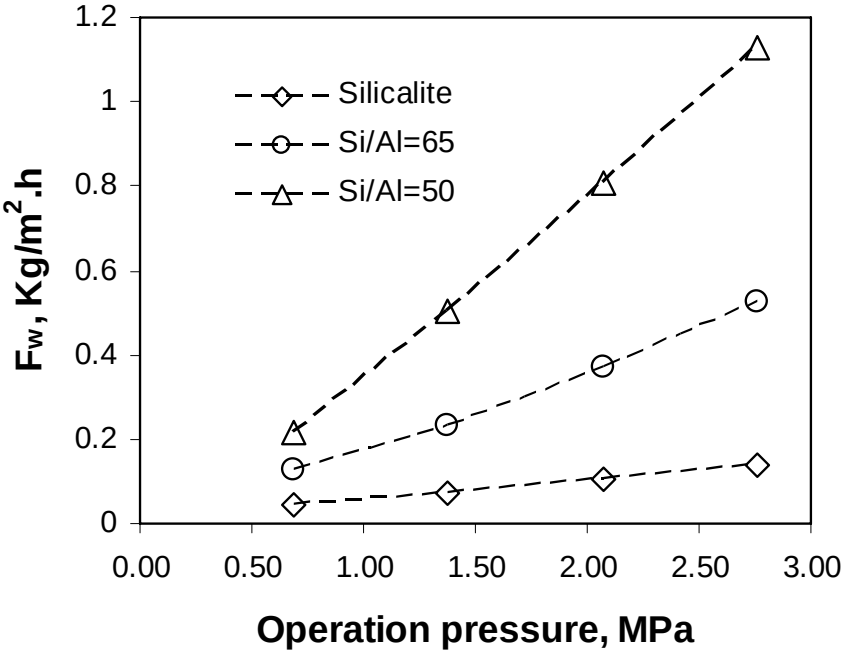

Fig. 19. Water flux of zeolite membranes as a function of operating pressure.

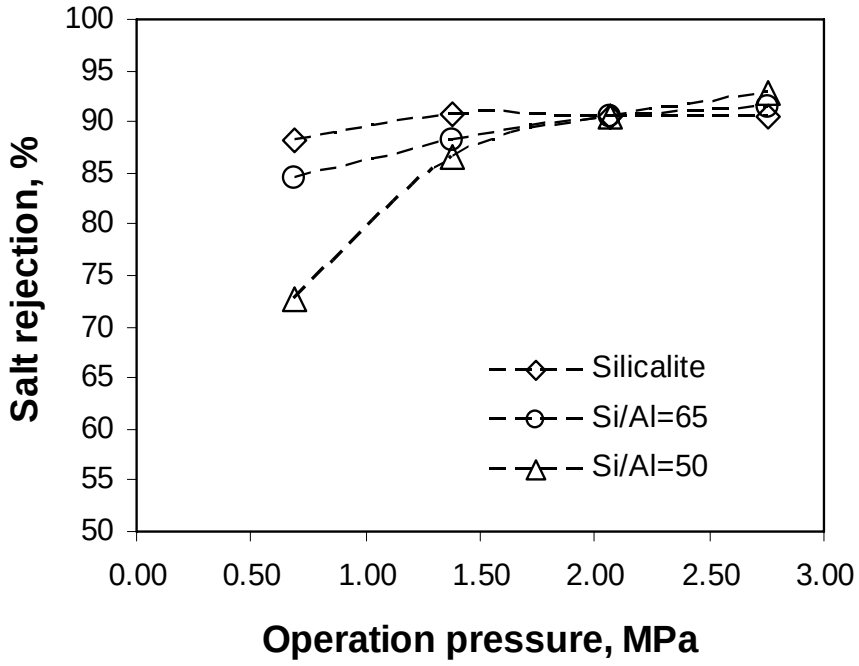

Fig. 20. Ion rejection as a function of operating pressure for zeolite membranes with different Si/Al ratios.

Conventional reverse osmosis theory suggests that water permeation in RO membranes increase linearly with the transmembrane pressure [36], while ion transport is pressure-independent [37]. These theories cannot easily explain the transport behavior of water and ions in zeolite membranes because the permeation of ions and water in confined spaces, i.e. zeolite pores, are strongly dependent [10, 38]. Ion and water permeation in zeolite-like pores is not a single file movement; they need to overcome a high energy profile to pass each other [39]. Enhanced water permeation under increased operating pressure facilitates the diffusion of ions due to the "dragging effect" of water molecules on large and slow ions [38]. This results in a monotonic increase of ion flux with increase of water flux, as shown in Figure 21. The enhanced diffusion of large species by small and fast molecules is widely observed in zeolite membranes [40].

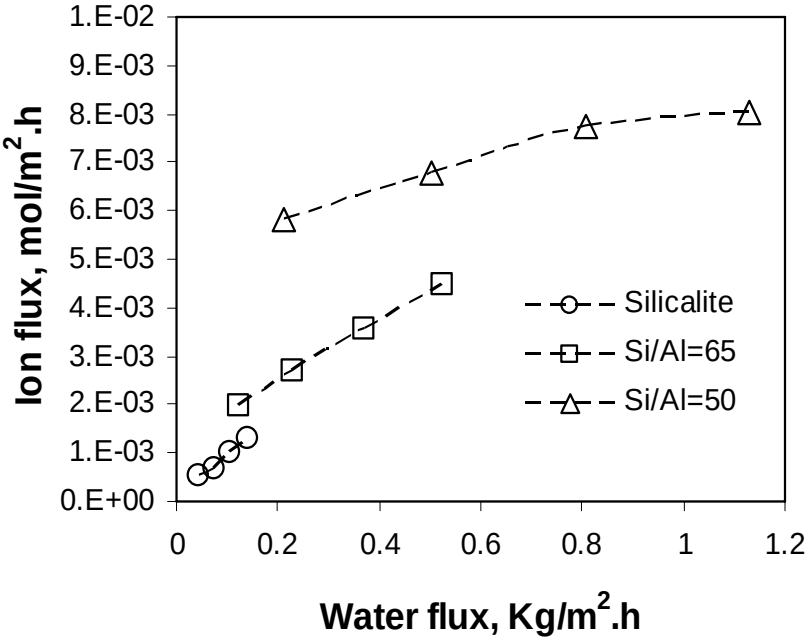

Fig. 21. Enhanced ion flux by water transport in zeolite membranes.

4. ZEOLITE INTRA/INTERCRYSTALLINE PORES AND THEIR INFLUENCE ON ION SEPARATION

All practical zeolite films are polycrystalline, suggesting the presence of non- or less-selective intercrystal pores [25]. The presence of the non-selective intercrystal pores limits the separation performance so these need to be eliminated by post-synthesis modification such as metal oligomer modification or chemical vapor deposition (CVD) [41]. Precise determination of the pore size distribution (PSD) and porosity is important for understand the separation mechanism and design appropriate processes for pore modification. In this work, zeolite membrane microstructure, particularly intercrystalline pore size distribution, was studied by applying the HK and BJH models to the N_2 adsorption isotherm at 77K. The research indicated that the zeolite intercrystalline pore sizes are related to surface roughness associated with the properties of substrate and zeolite orientation. Zeolite films on a dense glass surface have mesopores with size distribution ranging from 1.0 nm to 2.5 nm. The intercrystal pore sizes of zeolite membranes on porous α-alumina support shift to larger values at 2.0–4.0 nm.

All the micro- and mesoporous materials used in this study were synthesized in the laboratory. The microporous crystalline materials including MFI-type zeolite with different particle sizes and Fau-type zeolite were synthesized by hydrothermal crystallization [6, 42]. Mesoporous γ-alumina was synthesized by sol-gel process [43]. Hexagonally ordered SBA-15 was synthesized by silica-surfactant self-assembly [44]. Other materials investigated in this study include MFI-type zeolite membranes on porous α-alumina support, b-oriented and randomly oriented zeolite film on silica glass. The

porous supports were made in the laboratory with a procedure described in previous chapter.

Nitrogen adsorption isotherms at 77K were determined using ASAP 2020 MicroPore System (Micromeritics, USA). The micro- and mesoporous powder samples were used as obtained. The membrane samples including zeolite membranes on porous support and thin films on glass surface were ground to small power in a marble mortar for N_2 physisorption isotherm analysis. All samples for the BET test were degassed at 90°C for 1 hr and then at 350°C for 8 hr. The isotherm data were analyzed by t-plot, HK, DFT, and BJH models for PSD derivation. Particle size, zeolite orientation and membrane morphology were studied by scanning electron microscopy (SEM, JEOL 5800LV). X-ray diffraction (XRD, Rigaku® Geigerflex diffractometer using Cu Kα radiation) was used to determine the real pore size. All the samples for X-ray test were dried at 120°C for 24 hours.

4.1 Isotherm and pore filling of micro- and mesoporous materials

Physical gas adsorption and desorption isotherm reveal the kind of porosity, pore size and surface area. More importantly, PSD can be further derived from the feature of the isotherm such as hysteresis loop and inflection point. Figure 22 gives the adsorption isotherm of the different type of micro- and mesoporous materials investigated in this work. The insets are the adsorption isotherm branch at low relative pressures (P/P_0) ranging from 10^{-7} to 10^{-2}.

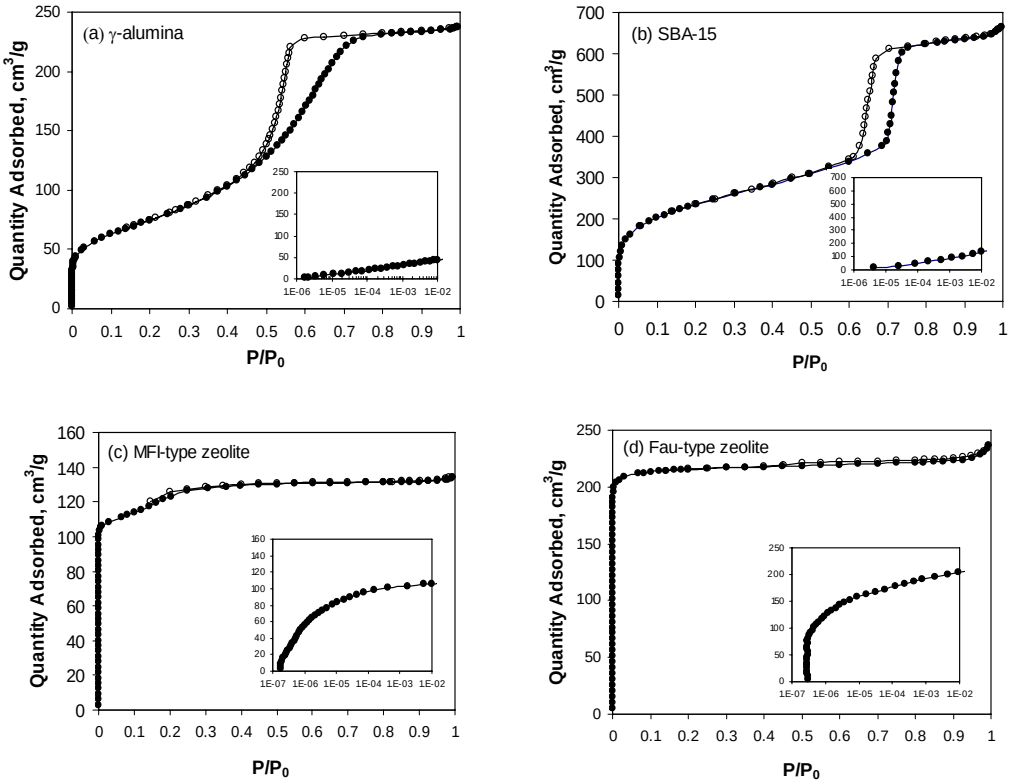

Fig. 22. N_2 adsorption isotherm at 77K ((a) γ-alumina, (b) SBA-15, (c) MFI-type zeolite, and (d) Fau-type zeolite). Solid circles denote adsorption and open circle denote desorption branch.

Zeolites show typical Type I isotherms (Figures 15 (c) and (d)) as defined by Brunauer [45], in which primary adsorption occurred at low relative pressures (P/P_0<0.01). The mesoporous γ-alumina and SBA-15 show typical Type IV isotherms with a large adsorption increase at higher relative pressure (P/P_0=0.4–0.7) and characteristic hysteresis loop as shown in Figs. 15 (a) and (b). The insets low-pressure adsorption isotherm branch (P/P_0=10^{-7}–10^{-2}) gives the characteristics of micropore filling. The γ-alumina and SBA-15 show a continuous increase in absorption volume at low P/P_0 range with no observable pressure transition and inflection point, suggesting the absence of micropores [46]. The rapid increase in adsorption at low relative pressure of Fau- and MFI-type zeolites is caused by the micropore filling of N_2. The adsorption isotherms of

MFI-type zeolites (dia.=0.56 nm) and Fau-type zeolites (dia.=0.74 nm) each have different features, so that the latter show much faster increases in adsorption at low partial pressure ranges.

To derive the PSD of micro- and mesoporous materials as well as microporous membranes, several models including HK, BJH and DFT models were applied to the physisorption isotherm shown in Fig. 15. The HK model derived from relations between relative pressures ranging from 10^{-7} to 10^{-2} and micropore radius is reported to be reliable for slit-shape micropore determination [47]. In this case, HK (Saito-Foley) model was applied for micropore size calculation because of the cylindrical pore geometry of zeolites [48]. Table 2 compares the pore size of microporous zeolites (Fau-type and MFI-type) and mesoporous γ-alumina and SBA-15 derived from different models and pore size calculated from X-ray diffraction pattern.

Table 2. Pore size distribution determined by different model

Material	HK (SF model)	BJH	DFT, cylindrical pore	X-ray
γ-alumina	4.0 nm	4.6 nm (adsorption branch) 4.3 nm (desorption branch)	5.0–8.5 nm	4.5 nm
SBA-15	7.1 nm	7.6 nm (adsorption branch) 6.0 nm (desorption branch)	9.5 nm	8.0 nm
MFI-type zeolite	0.72 nm	50 nm for particles with dia.<100 nm	0.76 nm	0.56 nm
Fau-type zeolite	0.78 nm	0.38 nm for desorption branch	0.75 nm	0.74 nm

Large deviations in PSD of microporous zeolite derived from HK and DFT models were observed. Also, the PSDs of MFI-type and Fau-type zeolites are not distinguishable, which was explained by the presence of quadrupolar moment in N_2 [49].

The HK pore size distribution of mesoporous γ-alumina and SBA-15 are underestimated comparing to the real pore size obtained from x-ray diffraction. The DFT model, on the other hand, overestimates the PSD for both micro- and mesoporous materials. The BJH pore size distribution of γ-alumina and SBA-15 in this study is in good agreement with the X-ray results but considerable difference between the adsorption and desorption branches was observed. If the physisorption is used as a routine analysis method, the experimental condition, pore model selection, and operating parameters must be carefully calibrated using materials with well-defined pore structure.

Presence of mesopores is widely observed in microporous membranes synthesized by sol-gel process (i.e. silica membranes) and hydrothermal crystallization (i.e. zeolite membranes) [50]. Pore size distribution in the mesopore range is critical to evaluate the membrane performance in molecular sieving because they are usually non-selective for separation. In order to judge the presence and amount of mesopores in microporous membranes, it is necessary to determine the PSD in the mesoporous region (2.0nm<dia.<50nm). Figure 23 gives the BJH pore size distribution of the porous material derived from the N_2 adsorption and desorption isotherm.

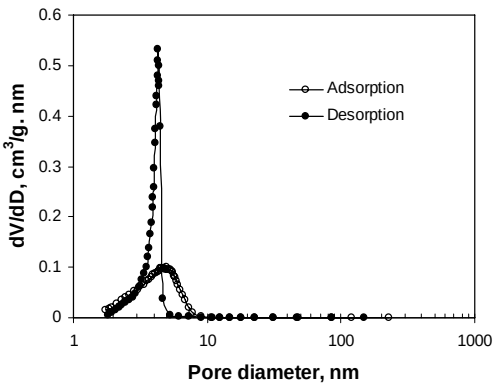

(a) γ-alumina

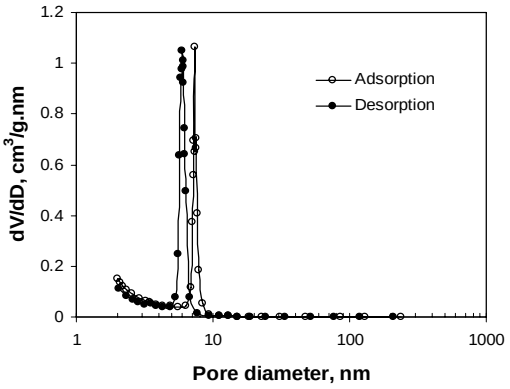

(b)SBA-15

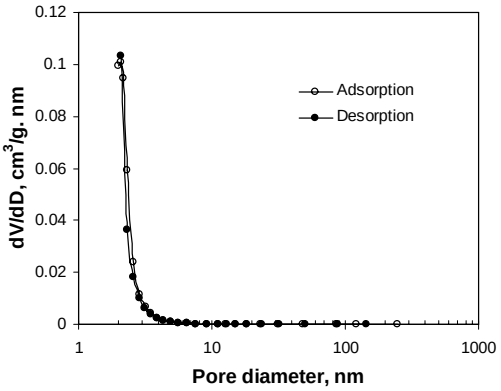

(c)MFI-type zeolite

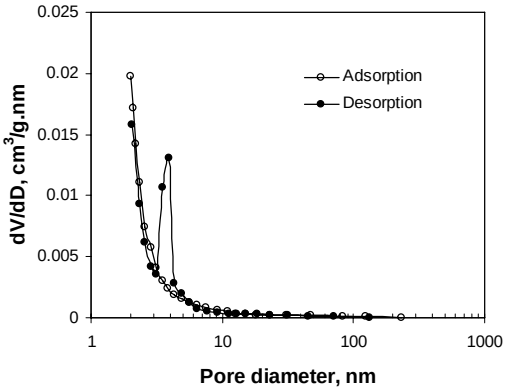

(d) Fau-type zeolite

Fig. 23. BJH pore size distribution derived from N2 physisorption isotherm.

For mesoporous material, the PSD derived from adsorption branch of the physisorption isotherm give a large pore size compared to that obtained from the desorption branch, for example. We attribute this observation to the hysteresis loop in the phyisorption isotherm. The inhibition of evaporation causes the decreasing loop lag behind and result a shift of PSD to lower values [51]. The PSD determined by BJH model on adsorption isotherm is in good agreement with the XRD results. In this case, using the adsorption branch for PSD calculation is suggested even though the BJH pore size distribution obtained from the adsorption and desorption branches has identical trends due to the reversible adsorption and desorption isotherm. The BJH model does not give an estimation of PSD when the pore sizes are less than 1.0 nm. However, PSD at ~4.0nm could be erroneously created when the BJH model is applied to the desorption branch of the isotherm, as shown in Fig. 16 (d). A similar phenomenon was reported on ZSM-5, which is explained by the forced closure of the hysteresis loop on the desorption branch [49].

4.2. Adsorption isotherm of zeolite with different crystal size

MFI-type zeolite crystals having different particle sizes were synthesized with the procedure listed in Table 2. Figure 24 gives the N_2 physisorption isotherm of these zeolites at 77K. The insets are corresponding SEM images of the zeolite crystals. As particle size decreased from 500 nm to 80 nm, a considerable increase in adsorption amounts at a high relative pressure (P/P_0>0.9) was observed. The adsorption on the outer surface and gas filling in the interparticle spaces are responsible for such inflections.

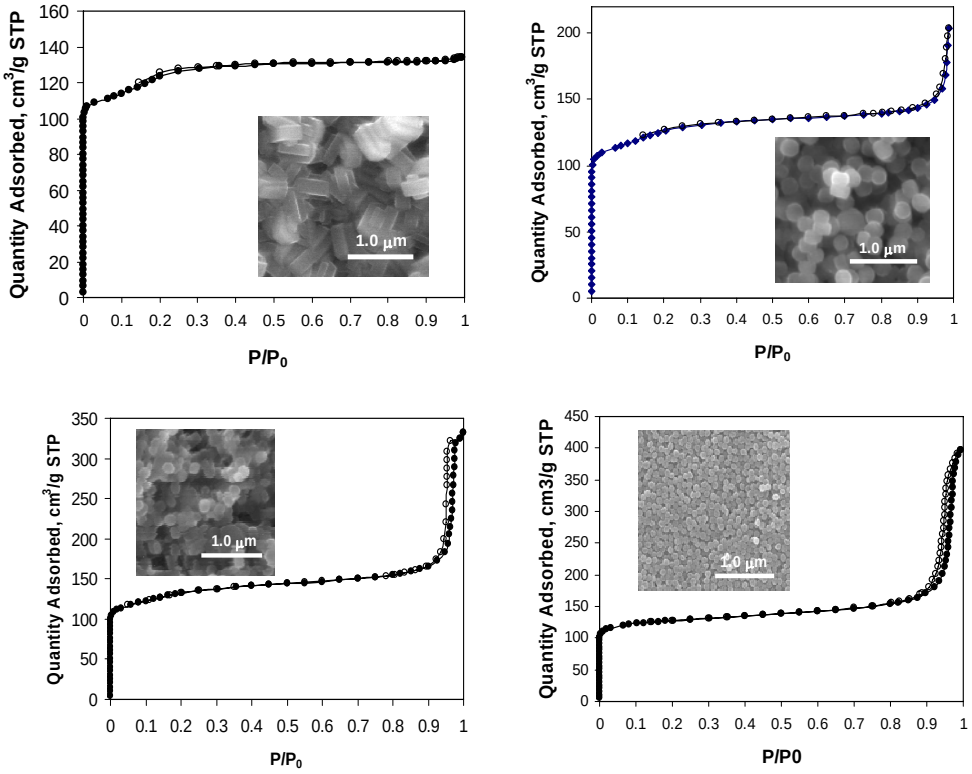

Fig. 24. Physisorption isotherm of N2 at 77K for MFI zeolite with different particle size.

4.3. Pore size distribution of zeolite films on glass surface

Many zeolites exhibit anisotropic pore geometry. For example, MFI-type zeolite has an anisoptropic bidimensional pore structure: straight channels of elliptical cross

section and sinusoidal channels of nearly circular cross section [52]. Zeolite membranes with b-orientation were suggested to have minimized intercrystal pores and enhanced molecular sieving performance when used for gas and liquid separations [30]. To study the influence of orientation on the intercrystal pore size distribution, MFI-type zeolite films with b-orientation and random-orientation were synthesized on thin glass slides by hydrothermal crystallization. Figure 25 shows the SEM surface images of b-oriented and randomly-oriented zeolite on dense glass. After firing at 500°C for 3 hr, the zeolite film on glass was tested for N_2 adsorption isotherm at 77K. Figure 26 gives the HK pore size distribution of the zeolite film shown in Figs. 25(a) and 25(b), respectively. The insets are t-plots derived from the adsorption isotherm, with solid circles denoting the second inflection in the curve.

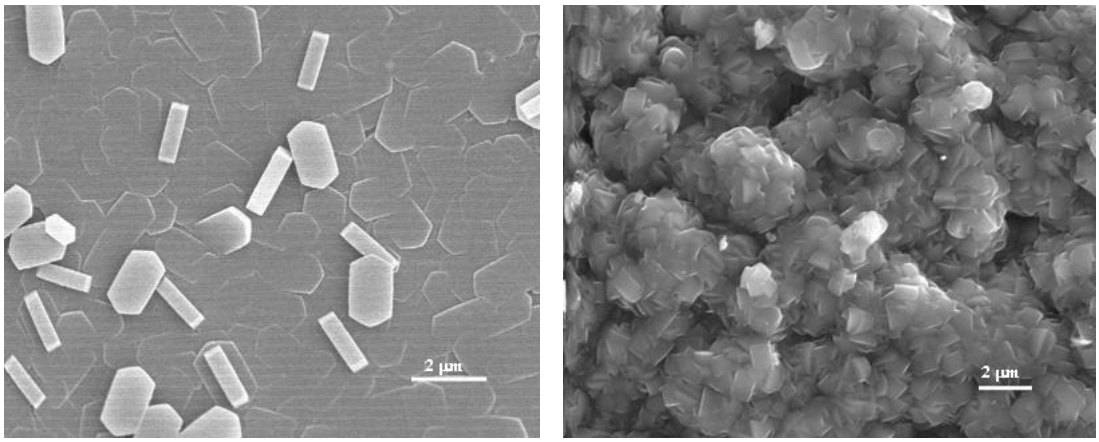

(a) b-oriented (b) randomly-oriented

Fig. 25. SEM images of zeolite film on glass slides with different orientation.

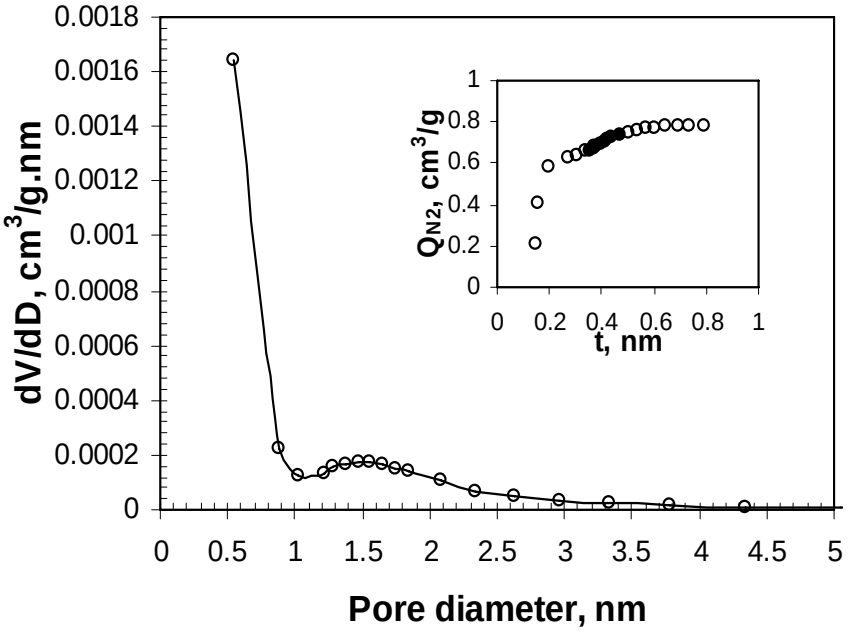

(a) b-oriented

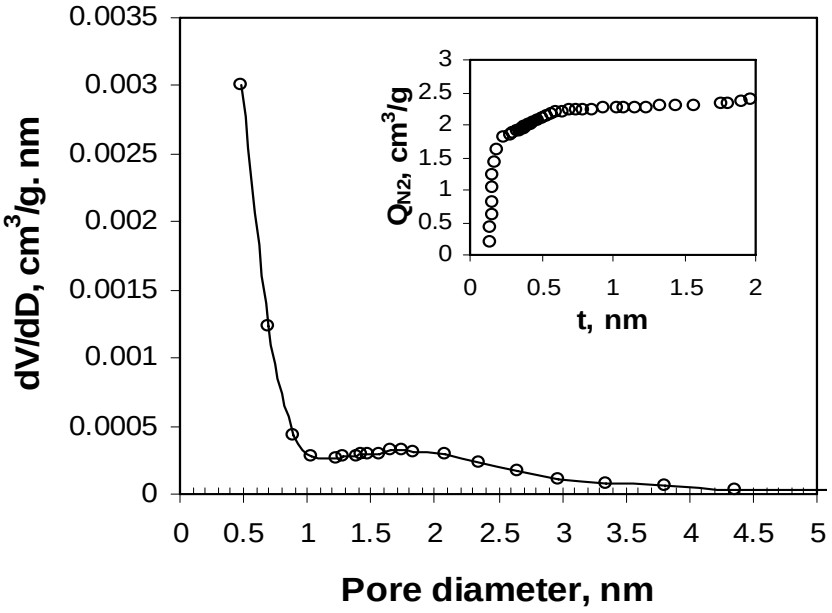

(b) Randomly oriented

Fig. 26. Pore size distribution (HK) of zeolite film on glass slides. Insets are t-plots with solid circles denoting the second inflection.

Both HK pore size distribution and step-wise t-plot (two inflections in the curve) denote the presence of bimodal pore structure of zeolite film synthesized therein. Besides the well-known zeolitic pores (0.56 nm), b-oriented zeolite films also have intercrystal pores with PSD ranging from 1.0 nm to 2.5 nm while the randomly-oriented zeolite films give enlarged intercrystal pores centering at 2.0 nm. The PSD of zeolite film on glass slides is in the same range as that of the spin-on zeolite film (2.7-3.3 nm) [53], but is larger than that on stainless steel revealed by molecular probing [54].

4.4. Pore size distribution of polycrystalline zeolite membranes on porous support

Zeolite membranes are generally formed on porous supports such as α-alumina and stainless steel for separation applications. The PSD of zeolite membranes is subject to increasing interest due to its determining influence on separation performance [30]. Figure 27 gives the adsorption isotherms of MFI-type zeolite membranes and porous α-alumina support. The isotherm of the substrate has a sharp increase in adsorption at relative pressure (P/P_0) of 0.9, which is explained by pore filling in large pores (>50 nm). Since the zeolitic pores are well-defined (dia.=0.56nm), a BJH model is applied to the isotherm of both substrate and zeolite membrane for mesopore characterization. Figure 28 gives the PSD of the substrate and zeolite membranes on porous α-alumina support. The substrate has large pores with PSD at ~90 nm as expected. The zeolite membranes have a wide PSD with major mesopores in the range of 2.0nm–4.0nm, which is responsible for the size of grain boundary defects caused by synthesis and sintering. However, the presence of larger intercrystal pores cannot be determined from the isotherm analysis. The PSD of zeolite membranes derived from physisorption isotherm is in good consistency with the estimation reported in the literature [17].

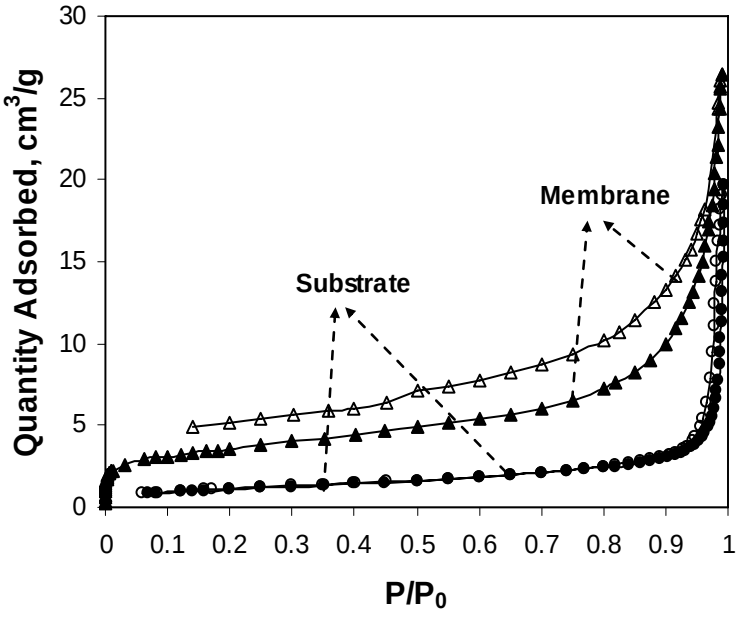

Fig. 27. N2 adsorption isotherm at 77K.

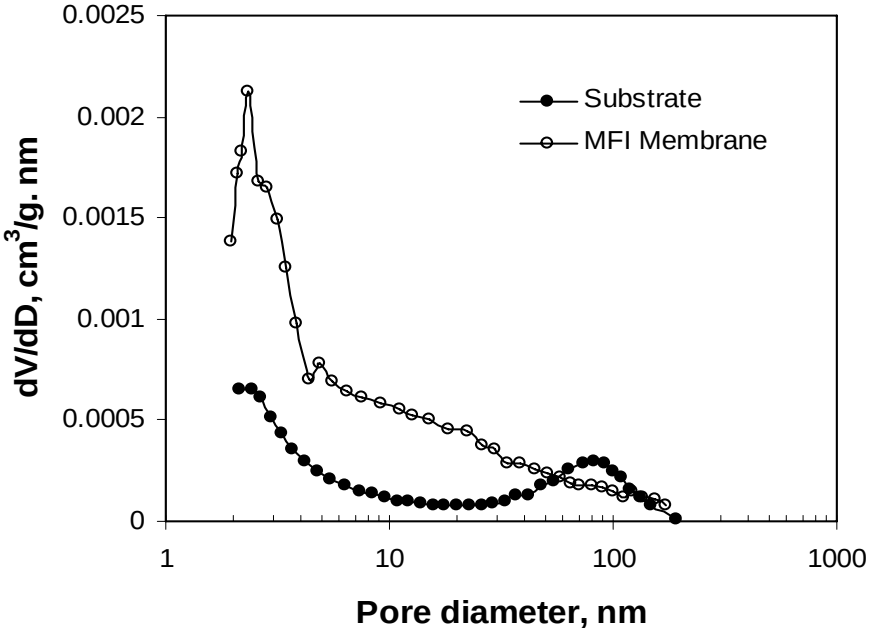

Fig. 28. Pore size distribution of substrate and zeolite membrane.

5. ELIMINATION OF ZEOLITE INTERCRYSTALLINE PORES BY POST-SYNTHESIS AL^{3+} OLIGOMER DEPOSITION

As confirmed by the N_2 adsorption and desorption investigation, all the polycrystalline zeolite membranes contain permselective zeolitic pores and intercrystalline microdefects, which contribute to the ion leakage and weak performance in ion separation. To eliminate the intercrystalline nano- or subnano pores, Al^{3+} oligomer deposition was performed for post-synthesis modification. The oligomers are deposited into the intercrystal pore region by a counter-diffusion process, in which the oligomer precursor solution flows on one side of the membrane and a 0.05M NaOH solution flows on the other side. The polyhydroxy-cation precursor ($[Al_{13}]^{n+}$) with small oligomer size (~0.84nm) meets the alkali solution (OH^-) in the intercrystal pores to form higher oligomeric clusters ($[Al_{13\sim24}]^{9+\sim12+}$) [55]. These large ionic oligomers are deposited in the intercrystal pores by strong electrostatic sorption to the zeolite surface, thus significantly reducing the intercrystal space. The ionic oligomers also make the intercrystal space strongly charged that restrict the cations to enter and transport. Figure 29 shows schematically the counter-diffusion apparatus employed for the membrane modification.

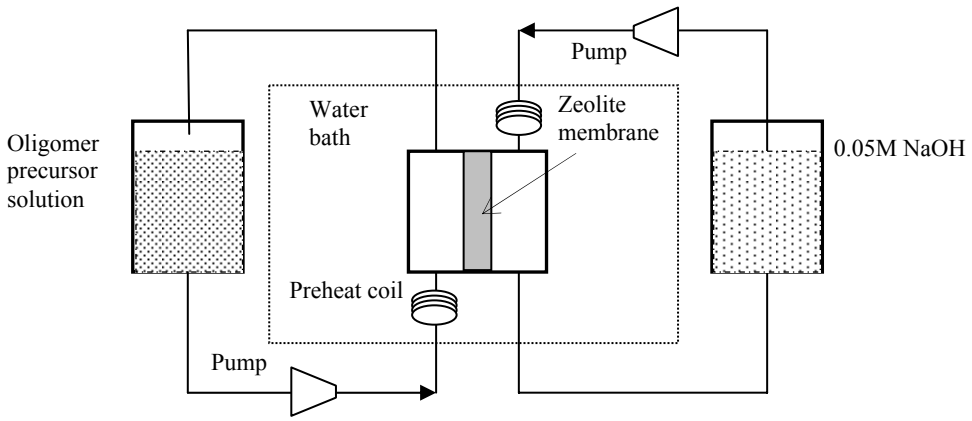

Fig. 29. Schematic diagram of the apparatus for membrane modification.

The Al^{3+} oligomer precursor solutions were prepared following a procedure developed by Pinnavaia, et al. [56]. A 0.20M NaOH solution was added dropwise into a 0.10M $AlCl_3$ solution under vigorous stirring at 55°C. The volumetric ratio of the NaOH and $AlCl_3$ solutions was controlled to give a hydrolysis ratio (OH^-/Al^{3+}) of 2.0 in the final mixture to ensure a relatively small oligomer size (<0.84nm). The mixture was then stirred for 12 hr at the same temperature. The resultant Al^{3+} oligomer precursor solution was refrigerated at 5°C before use.

The oligomer precursor and the 0.05M NaOH solutions flowed over the two sides of the membrane at a flow rate of 2.0 ml/min. The water bath temperature was controlled at 55°C to enhance diffusion and facilitate the oligomerization. After modification, the membrane was rinsed thoroughly with deionize water and then dried at 100°C in an air flow for 12 hr.

5.1. Tests of the modified membranes

The membrane was tested by nitrogen permeation and RO desalination for NaCl solutions with different concentrations before and after the modification. Nitrogen gas permeation was conducted by the Wicke-Kallenbach method at 50°C using helium as

sweeping gas on the permeate side. The RO experiments were performed on a cross-flow system. The membrane cell was immersed in a water bath for temperature control (±0.2^{o}C, RDL 20, GCA). The RO desalination was performed for NaCl solutions with concentrations of 0.01M, 0.03M, 0.10M, 0.30M and 1.00M, respectively. For each feed solution, the RO experiment lasted for more than 120 hr to obtain stabilized flux and ion rejection rates. The membrane was rinsed and then immersed in 500 mL DI water for overnight to extract the residual solution before switching to the next solution of different concentration.

The nitrogen permeance (defined as flux normalized by transmembrane pressure) of the MFI membrane decreased from 2.80×10^{-8} mol/m^2·s·Pa before modification to 1.94×10^{-8} mol/m^2·s·Pa after modification. The decrease in the nitrogen permeance was caused by the reduction of intercrystalline pores by the oligomer deposition since the ionic oligomers, as well as the hydrated Al^{3+} , are too large to enter the zeolite channels.

The RO tests for all the NaCl solutions were conducted at 30°C with atmospheric pressure (0.086MPa in the lab) on the permeate side. The feed pressure for the 1.0M NaCl solution was 4.13MPa. For all the other solutions, the feed pressure was 2.75MPa. The results of the RO tests are shown in Table 3.

Table 3. Results of reverse osmosis for NaCl solutions with different concentrations.

Feed concentration (M)	Before modification		After modification	
	F_w, mol/m^2.h	r_i, %	F_w, mol/m^2.h	r_i, %
0.01	39.4	84.1	22.6	91.7
0.03	40.0	73.8	20.9	89.7
0.10	37.4	61.5	20.4	88.4
0.30	36.9	55.4	16.1	81.3
1.00	36.1	44.6	14.1	60.2

Both the water flux and ion rejection rates exhibited general trends to decrease with increasing the ion concentration from 0.01 to 0.30M for the MFI membrane before and after the modification. The decline of water flux for high feed concentration is caused by (1) the increased osmosis pressure which lowered hydraulic pressure difference (ΔP) across the membrane thickness and (2) the enhanced ion sorption to the internal and external surface of the zeolite which increased the resistance for water transfer. Similar phenomena were observed on other zeolite membranes synthesized with different methods.

After modification, the water flux of the membrane became significantly lower compared to that measured before modification. This was caused by the reduced intercrystalline pore volume and enhanced charge density in the intercrystalline space by ionic oligomer deposition. It is possible that electrostatic sorption of the ionic oligomer also occurred at the membrane surface, which could have further hindered water transport through the membrane.

The concentration-dependent ion rejection is caused by the diminishing of the double layer in the high-concentration solution in which the intercrystalline pores will open up for free ions to transport. The water flux in RO membranes increases proportionally with ΔP, while the ion flux depends primarily on the gradient of chemical potential, which is virtually independent of pressure in liquid phases. The mechanisms of ion and water transport during reverse osmosis have been discussed in our previous report. Figure 30 shows the ion rejection rates as a function of feed concentration or estimated double layer thickness, i.e. the Debye screening length (κ^{-1}) [57], to compare the membrane RO performance before and after modification.

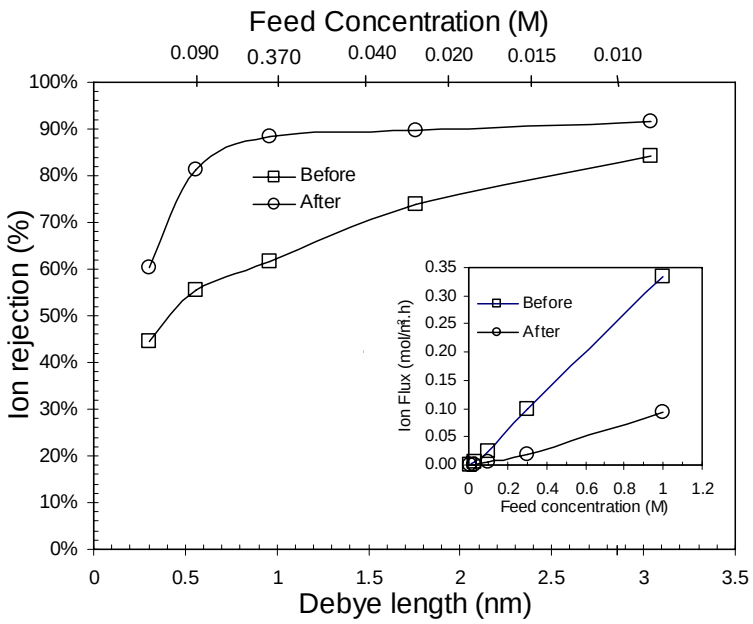

Fig. 30. Ion rejection as functions of feed concentration and double layer thickness (inset: ion flux as a function of the feed concentration).

The ion rejection rates on the modified membrane were significantly higher than those obtained before modification. However, the ion rejections for the 0.01 M solution were similar for the membrane before and after modification. In the dilute solutions, the charged double layers were able to overlap in all the intercrystal spaces to limit the ion transport even without modification. Thus, for dilute solutions, the membrane modification is less effective to improve the ion rejection but causes significant loss of water flux.

The enhancement in ion rejection by the membrane modification became more significant as the feed concentration increased. This indicates that the relatively large intercrystalline pores were reduced and modified effectively by the deposition of ionic oligomers. The double layer thickness drops from 3.0nm for the 0.01M NaCl solution to 0.30nm for the 1.0M solution. Therefore, the charged double layer diminishes and the

intercrystalline pores open up gradually for ion transport in the unmodified membrane as the feed concentration increases, leading to a fast decrease in ion rejection rate starting from the lowest concentration. On the contrary, the ion rejection rate decreased only slightly when the feed concentration increased from 0.01 M to 0.1 M. This indicates that most of the intercrystal pores with sizes larger than ~2nm were modified effectively. However, the ion rejection rate on the modified membrane started to drop rapidly for feed concentrations higher than 0.1 M, suggesting that the modification was inefficient for pores with relatively small sizes (i.e. <2nm). The highly charged Al^{3+} oligomers may carry a large number of bonded water molecules that makes the oligomeric clusters too large to enter the small intercrystallline pores.

5.2. Long-term stability of modified membranes

Desalination of real produced water on a modified zeolite membrane was performed for over 500 hr to investigate the stability of metal oligomers at produced water environment and necessity for reinforcement. The produced water sample obtained from local gas field in Farminton, NM was pretreated by filtering through a 2 μm-Whatman® filter paper for removing of particulates. The pretreated produced water was forced to flow across the membrane surface and the permeate samples were collected and analyzed by IC for ion concentration analysis. Then the membrane was rinsed with DI water and treated by Al^{3+}-oligomer modification. Finally, permeation of the produced water was carried out on the modified membrane for the elapsed time for stability testing. Table 4 gives the chemical composition of the produced water sample together with the ionic compositions in the permeate solution after permeating through the zeolite membrane.

Table 4. Effect of membrane modification on the RO performance

Ions	Feed concentration mg/L	Permeate concentration, mg/L Before modification	After modification
Sodium (Na^+)	4327.3	2067.3	1331.5
Potassium (K^+)	384.4	163.4	119.1
Chloride (Cl^-)	6315.3	3254.3	2065.2
Sulfate (SO_4^{2-})	975.4	82.1	<2.0
Total dissolved salt (TDS), mg/L	12002.4	5567.1	3515.8

After modification, the rejection of the total dissolved solid (TDS) increased from 53.6% to 70.7% and the water flux declined from 0.102 kg/m^2.h to ~0.056 kg/m^2.h. Figure 31 gives the water flux and ion rejection as a function of permeation time. The ion rejection first increase then stabilized at 71% throughout the permeation period, indicating good stability of the metal oligomer deposition. The water flux declines slightly with elapsed permeation time because of the cake formation caused by particle deposition from the produced water sample.

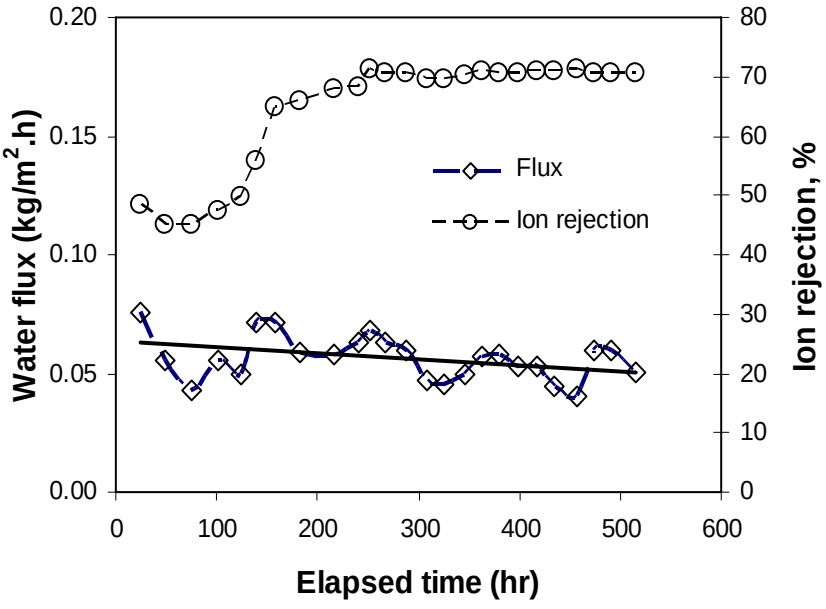

Fig. 31. Water flux variation at the prolonged RO permeation time.

6. ION SEPARATION PERFORMANCE ON ZEOLITE MEMBRANES

Zeolite membranes, specifically LTA (pore size ~0.4 nm) and MFI (pore size ~0.56 nm) type, can separate ions from aqueous solution by reverse osmosis [58]. The separation mechanism involves size exclusion of hydrated ions [54, 58] and electrostatic repulsion (Donnan exclusion) at intercrystalline pore entrance. Such a combination allows zeolite membranes to be unique in separations of both organics and electrolytes from aqueous solutions by reverse osmosis process [5].

A considerable amount of experimental work and theoretical modeling studies have been carried out for understanding the transport of water and ion in microporous media [10, 21, 59]. The ionic mobility of hydrated ions in cylindrical pores of radius less than 1.1 nm was reported to be considerably lower than that in bulk solution [13]. The factors governing the structure and diffusion of ion and water in microchannel include surface charge [12], hydrophilicity [14], and pore wall roughness [15]. The fundamental study of ion permeation through zeolite membranes is crucial to understand the ion separation mechanism in zeolite membranes. In addition, ion permeation behavior in microporous channels can help us to better understand the microstructure of zeolite thin film.

Ion separation by zeolite membranes was performed by cross-flow experiments, as shown in Fig. 32. Membranes with different configuration were mounted in a cross-flow cell in which orginal produced water was forced to flow across the membrane surface. The disc-shaped zeolite membrane was mounted facing the feed stream in a

stainless steel cell sealed by silicone O-rings. Both the feed chamber and permeate chamber of the cell had small volumes of about 0.5 cm^3. Tubular membranes were assembled by inserting the membrane tube into a lab-designed Nylon cell. Both ends of the tubular membranes were sealed by O-rings. The feed solution flows through the internal and the outer cylinder of the Nylon cell retains the effluent, where it is removed through a port and collected in an 8.0 mL-Tyflon bottle. In this design, membranes can be easily replaced for permeation testing. For commercial application, a large number of tubular membranes could be packed into a pipe and ends of tubes could all be capped with injection-molded plastic caps that can seal both ends of the tubular membranes and the outer cylinder. It should be noted that the membranes used in this study include both pure silicalite membranes and ZSM-5 membranes, which show considerable difference in water flux.

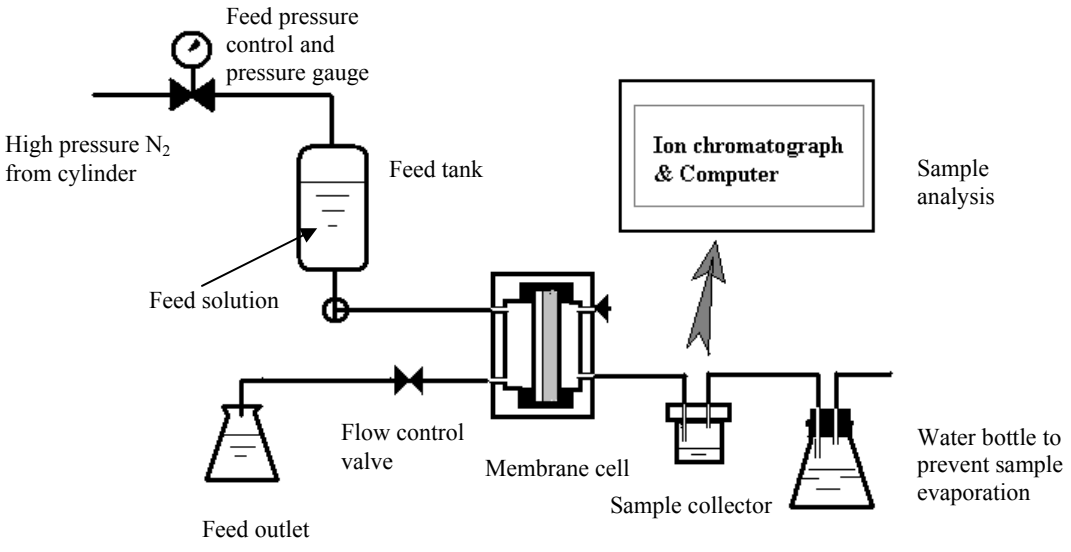

Fig. 32. Schematic diagram of the RO system.

The feed pressure was maintained by a nitrogen cylinder, and the feed flow rate was controlled by a needle valve located at the feed chamber exit. A very stable feed

pressure was maintained throughout the experimental process. The feed flow rate was maintained at 0.5 mL/min at the outlet, while the permeate flow rate was less than 1% of the feed flow rate so that the feed side concentration could be considered constant at inlet and exit. The liquid permeate was collected by a small Teflon sample bottle at ambient pressure (86 kPa in Socorro, New Mexico). The sample bottle was connected to the gas phase of a water flask through a capillary tube to prevent evaporation of the received liquid. Both the feed solution and the collected permeate solution were diluted to appropriate concentrations (~0.0025 M) and analyzed by a dual-column ion chromatograph (IC, DX120, Dionex), equipped with a computer data acquisition and analysis system. Rejection of ion *i*, r_i, is defined by equation (1),

$$r_i = \frac{(C_i)_{feed} - (C_i)_{perm}}{(C_i)_{feed}} \times 100\% \qquad (1)$$

where $(C_i)_{feed}$ and $(C_i)_{perm}$ are concentrations of ion *i* in the feed and permeate solutions, respectively. The water flux (F_w) and permeance (P_a) are defined as follows:

$$F_w = \frac{Q_w}{A_m \cdot t} \qquad (2)$$

$$P_a = \frac{F_w}{\Delta P} = \frac{F_w}{P_f - P_p - \Delta\pi} \qquad (3)$$

$$\Delta\pi = \left[\left(\frac{C_s}{100 - C_s}\right)_{Feed} - \left(\frac{C_s}{100 - C_s}\right)_{Permeate}\right]\frac{RT}{Mw} \qquad (4)$$

where C_s is the total ion concentration, mol/L; $\Delta\pi$ is the difference in osmotic pressures between the feed and permeate solutions; Q_w is the quantity of water collected in a time period *t*; A_m is the effective membrane area, 2.5×10^{-4} m^2 for the disc-shaped membranes

and 1.24×10^{-3} m^2 for the tubular membranes; T is the temperature; R is the gas constant; and M_w is the molecular weight of the ion.

6.1 Influence of operation condition and solution chemistry on ion separation performance

The influence of operatiing parameters on the separation performance of zeolite membranes is critical to understand water and ion transport in microporous systems. Also these basic understandings give important information for improving the synthesis process and modification technique. The influences of ion valence, ion concentration, temperature and trans-membrane pressure on the ion separation performance of zeolite membranes were investigated through cross-flow RO permeation tests.

6.1.1 Ion valence

Influence of ion valence on desalination by zeolite membranes was studied through RO permeation tests of 0.10 M metal chloride solutions including 0.10 M NaCl, 0.10 M $MgCl_2$, and 0.10 M $AlCl_3$. Figure 33 compares the ion and water flux of the metal chloride solutions. Both ion and water fluxes decreased and the ion rejection increased in the order of NaCl, $MgCl_2$, and $AlCl_3$. The reduction of ion transport with an increase in ion valence is caused by the increasing charge density, which enhances the interactions between the ions and the pore wall and the double layers. Moreover, the apparent dynamic hydration number also increases with the charge density in the order of Al^{3+} > Mg^{2+} > Na^+. Since the intercrystalline pores have a size distribution, the number of intercrystalline pores permeable for ions is inversely proportional to the hydrated ion size or ADHN. Therefore, ion rejection increases in the order of $Na^+ < Mg^{2+} < Al^{3+}$.

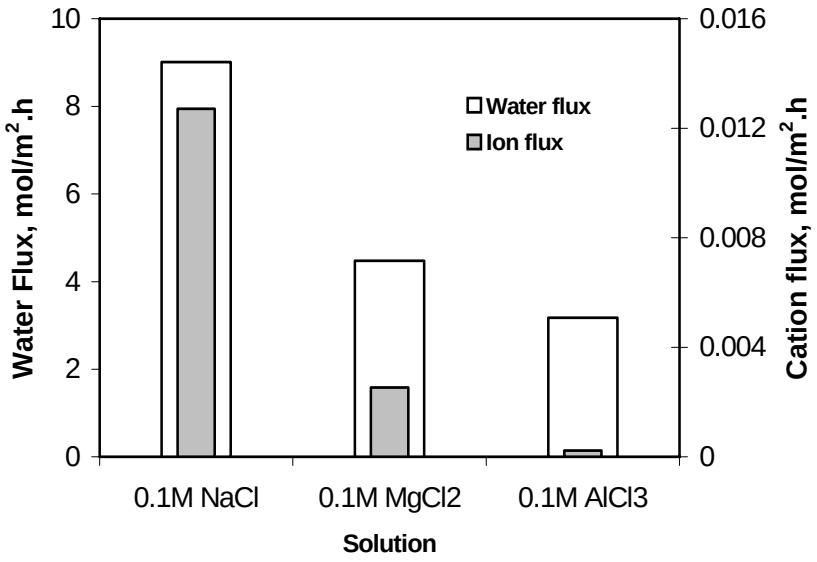

Fig. 33. Effect of cation valance on water and ion fluxes.

The mobility of water molecules neighboring the ions decreases with increasing ion-water bond strength and with dielectric friction, which enhances ion charge density and the inverse ion radius [7, 11, 60–61]. In the micropores, free water molecules are much fewer than in the bulk solution because the hydrated ions interact directly with the charged double layers, especially when the double layers tend to overlap in a small space [62]. Thus, the mobility of water molecules inside the pores is lower than that in the bulk solution because of the joint motion of water and ions [7] under the influence of charged double layers. Therefore, water and ion fluxes decrease with increasing ion valence in an order of Na^{+}> Mg^{2+}>Al^{3+}.

6.1.2 Ion radius

In the same column of periodic table, crystallographic ion size increases with increase of molecular weight. RO permeation tests with ions in the first column of periodic table (K^{+} and Na^{+}) and in the second column (Ca^{2+} and Mg^{2+}) were performed to study the influence of ion size on membrane separation performance. All ions existed as

0.10 M metal chloride solutions in water. Figure 34 shows the comparison between ion and water flux for these metal chloride solutions.

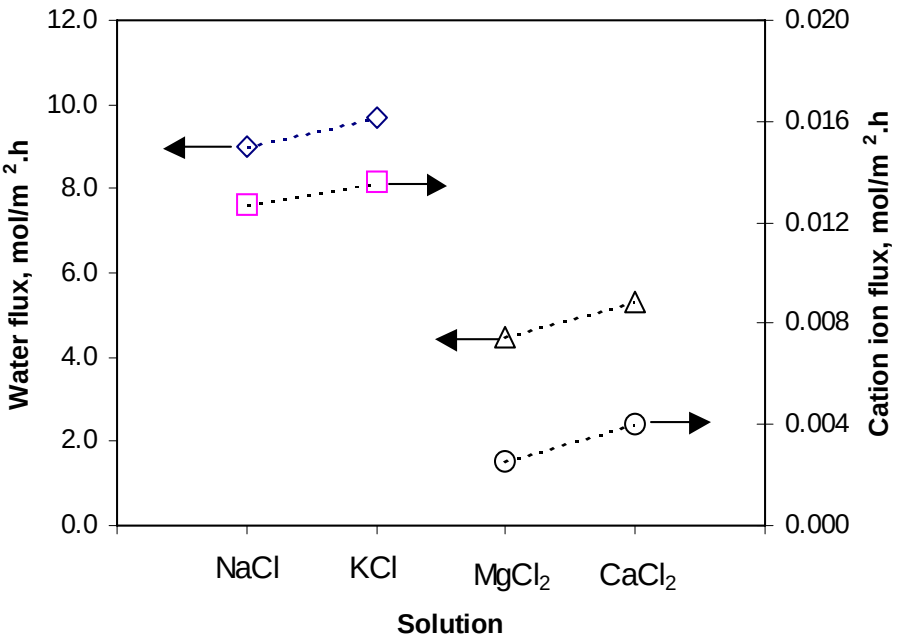

Fig. 34. Effects of cation size on water and ion flux.

The ion and water flux of 0.10 M KCl solution were higher than those of the 0.10 M NaCl solution. This can be explained by the fact that, for alkali metal ions in aqueous solutions, the diffusion coefficient increases and the friction coefficient decreases with increasing crystallographic ion size [8, 9]. The diffusion rate of ions in aqueous solution is governed by ion and water interactions. As ion crystallographic size increases, the distance between ion charge center and surrounding water is enlarged, resulting in weaker interaction between ion and water, thus reducing the friction coefficient [63]. The rejections of Na^+ and K^+ were close because they have similar hydrated ion sizes (with ADHN). Similar results were obtained by comparison of the ion and water flux between the $MgCl_2$ and $CaCl_2$ 0.10 M solutions. However, the rejection of Mg^{2+} was much higher

than that of Ca^{2+} because the former has a stronger polarization effect on the surrounding water molecules [64] and thus possesses a higher ADHN [65].

6.1.3 Ion concentration

Sequences of metal chloride solutions containing cations of Na^{+}, Mg^{2+} and Ca^{2+} were tested for RO separation on zeolite membranes. The solutions studied here have total dissolved solids (TDS) ranging from 856 to 8.56×10^{4} mg/L. The cations (Na^{+}, Mg^{2+} and Ca^{2+}) in all solutions have identical molar ratio of 86:2:1, a typical concentration ratio in CBM produced water of NM [66]. The RO separations were carried out on a tubular membrane at room temperature (~20°C) and trans-membrane pressure of 2.75 MPa. Figure 35 gives the individual ion rejection as a function of feed concentration. The influence of ion concentration on the overall performance of the zeolite membrane is shown in Figure 36.

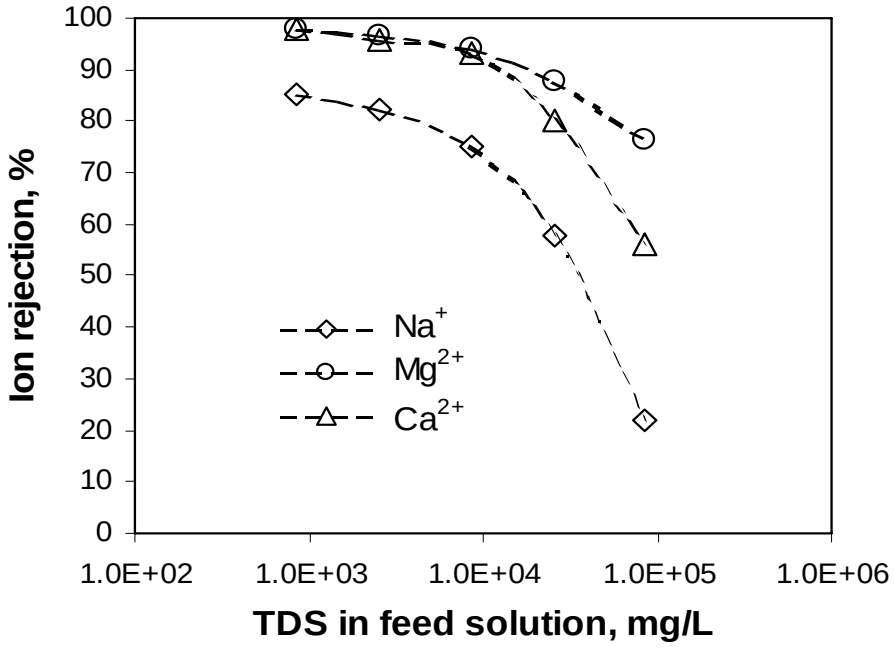

Fig. 35. Influence of ion concentration on individual ion rejection.

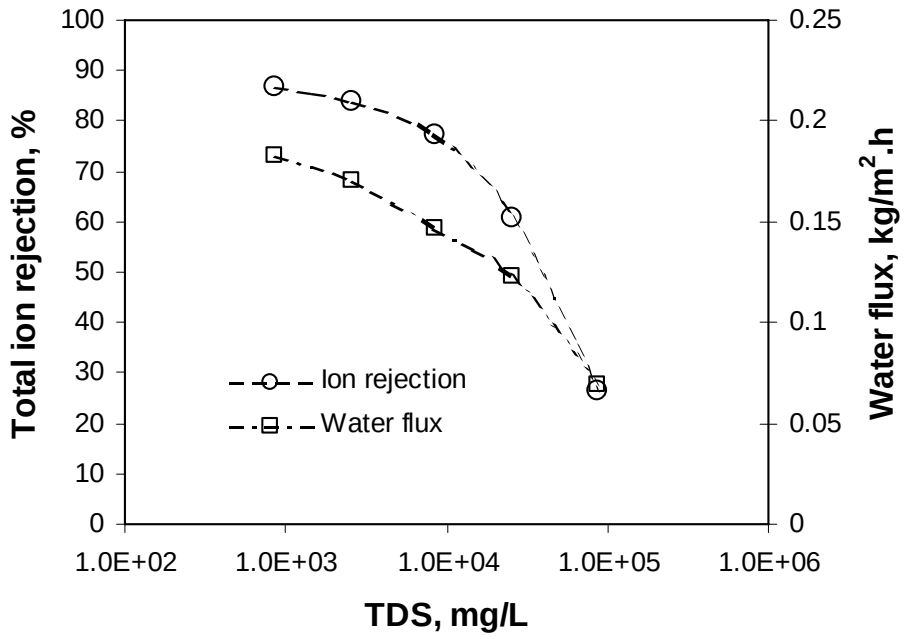

Fig. 36. Influence of ion concentration on overall ion rejection and water flux.

Both ion rejection and water flux decreased progressively with increase of ion concentration. The ion rejection of Na^+ declined rapidly from 85.3 to 22.1% as the TDS increased from 856 to 8.56×10^4 mg/L while the ion rejections of Ca^{2+} and Mg^{2+} were less affected by ion concentration. The decline of solute rejection with an increase in ion concentration was explained by the decrease of double layer thickness with ionic strength [67] that resulted in opening of more intercrystalline pores through which ions could penetrate. Separation through intracrystalline zeolitic pores was less affected by ion concentration because the sizes of hydrated ions are virtually constant as ion concentration changes [68]. At low ion concentration, both zeolitic pores and intercrystalline zeolite pores show ion rejection through the mechanisms of size exclusion and the overlapping of the double layer. As ion concentration increased, the majority of intercrystalline pores were opened up for Na^+ transport, but were still small enough to restrict the transport of multivalent ions such as Mg^{2+} and Ca^{2+} due to their large ADHN

and high charge density [7]. As ion concentration increases further, the ion rejection of Mg^{2+} and Ca^{2+} started to decline, as shown in Fig. 35.

The decline of water flux with an increase in ion concentration was explained by the reduced numbers of free water molecules and narrowed transport pathways in the zeolite layer. Water molecules in electrolyte solution exist as free water or hydrated water. The number of free water molecules decreases as ion concentration increases because the hydration number of ions is almost constant as ion concentration changes [68]. Moreover, as ion concentration increased, more ions were trapped in zeolitic pores and adsorbed onto the surface of intercrystalline pores that reduced the effective pore size, resulting decline in water flux.

6.1.4 Transmembrane pressure

RO permeations of 0.10 M NaCl solution on a tubular zeolite membrane were conducted at differential pressures ranging from 1.03 MPa to 2.76 MPa. Figure 37 gives the ion rejection and water flux as a function of operation pressure.

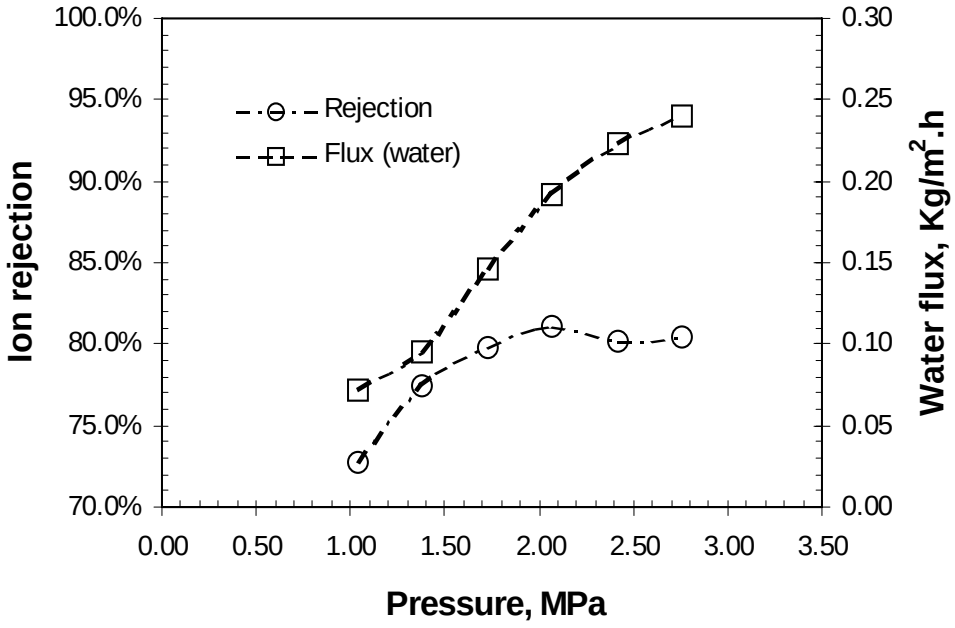

Fig. 37. Influence of operation pressure on membrane performance.

The water flux increased almost linearly from 0.072 Kg/m^2.h at operating pressures of 1.03 MPa to 0.241 Kg/m^2.h at 2.76 MPa. This is consistent with the classical solution-diffusion theory in which the driving force for water permeation is the differential pressure across the membrane. The ion rejection was found to increase from 72.7% to 80.5% as operating pressure increased from 1.03 MPa to 2.07 MPa and remained stable at ~80%, as differential pressure increased further from 2.07 MPa to 2.76 MPa.

Figure 38 gives the water flux variation as a function of transmembrane pressure. All the feed solutions with increasing NaCl concentration from 0.001M to 0.7M showed the same trend where water flux increased nearly linearly with the increase of the driving force (transmembrane pressure).

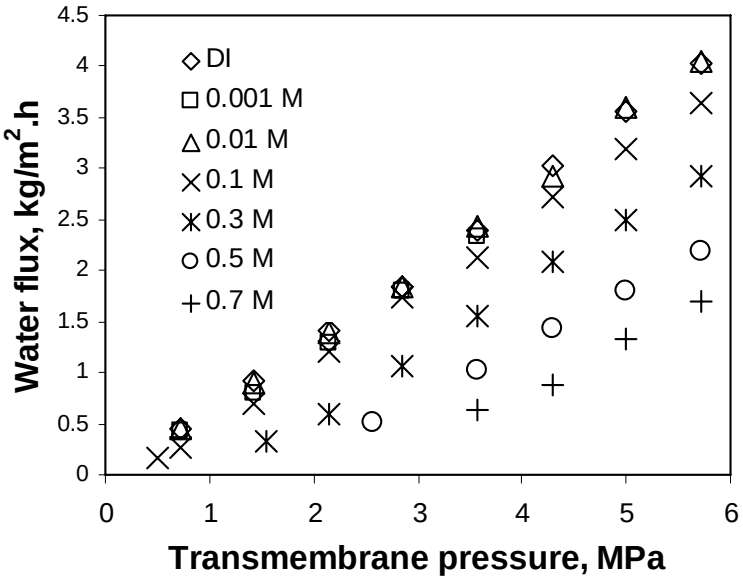

Fig. 38. Water flux variation as a function of transmembrane pressure.

Transmembrane pressure also showed considerable influence on the salt rejection efficiency, as shown in Fig. 39. Water transported across the zeolite membrane under the

driving force of effective transmembrane pressure, defined as $\Delta P = P_f - P_p - \Delta\pi$. P_f and P_p are pressures (Pa) of the feed and permeate sides, respectively. $\Delta\pi (\approx RT[C_{i,f} - C_{i,p}])$ is the osmosis pressure difference (Pa) between the feed and permeate solutions. Increasing the feed-side pressure increases the water transport driving force and thus the water flux. Fast water flux usually results in concentration polarization at the interface of the membrane, resulting in an increase in net driving force for ion diffusion. As a result, both water flux and ion permeation increased with increasing transmembrane pressure. However, the magnitude of increase in the water flux was much greater than that in the ion flux, resulting in an increase in ion rejection efficiency.

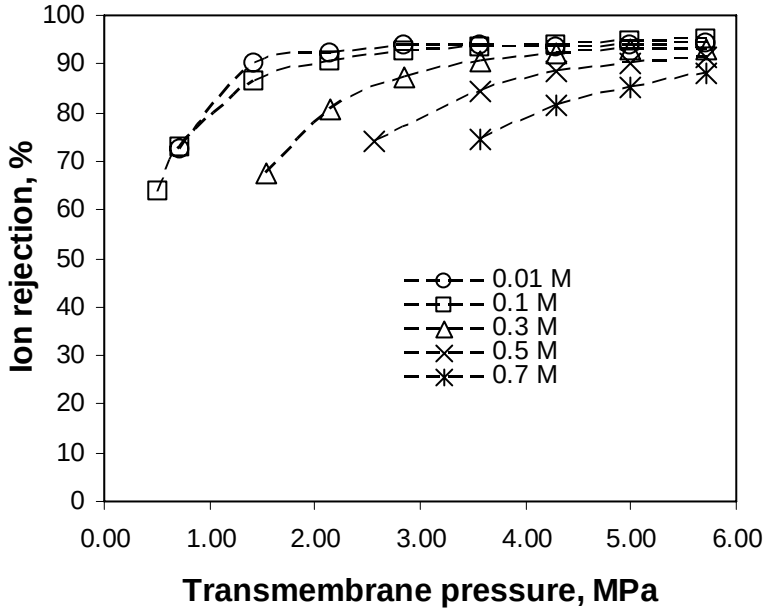

Fig. 39. Ion rejection changes as a function of transmembrane pressure.

6.1.5 Sweeping flow rate

Figure 40 shows the influence of water flow rate on membrane performance. As the sweeping flow rate increased from 0.01m/s to 0.1m/s, water flux increased from 12.1kg/m^2.h to 13.4kg/m^2.h and ion rejection increased from 85.0% to 88.9%. The

enhancement in both water flux and ion rejection at high water flow rate is explained by the influence of sweeping flow rate on the concentration polarization. Water diffusivity in zeolite membranes is at one or two orders of magnitude of that of ions [69], resulting in ion accumulation at the zeolite pore entrance. The concentration polarization at the membrane surface showed considerable influences on the membrane performance: reducing both water flux and ion rejection efficiency. One advantage of zeolite membranes compared to conventional polymeric membranes is that the zeolite membrane has excellent mechanical stability. Thus, strong turbulent flow can be deployed for breaking up the concentration polarization and enhancing the ion separation performance.

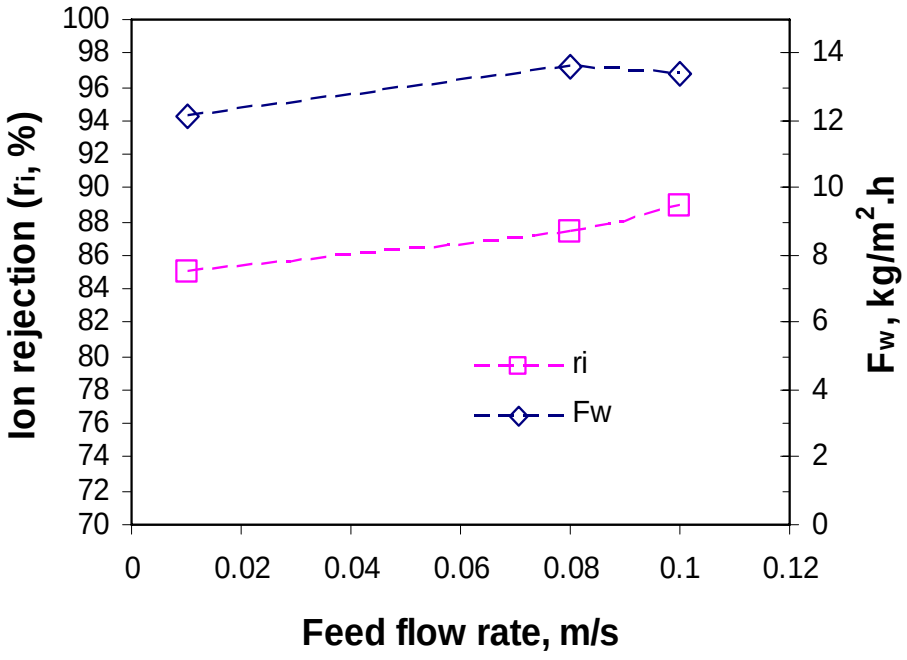

Fig. 40. Influence of feed water flow rate on the membrane separation performance.

6.1.6. Temperature

Figure 41 shows the ion rejection and water flux of a zeolite membrane at different operating temperatures. As water temperature increased from 297K to 318K,

water flux increased from 3.19 kg/m^2.h to 4.31 kg/m^2.h while ion rejection decreased from 98.7% to 95.1%. Water and ion diffusion through zeolite membranes follow the Arrhenius relation: increasing temperature will increase the water and ion diffusivities simultaneously. It was revealed that raising temperature increases the kinetic energy of ion and water that facilitates molecular collision at the zeolite pore entrances [69]. As a result, the permeation activation energies for ions (ΔE_i) are larger than those for water (ΔE_w), meaning that water flux increases more significantly at increasing temperatures compared to that of water. In the circumstances of produced water desalination, increasing the feed water temperature is desirable for the enhancement in water flux while the ion rejection is essentially the same.

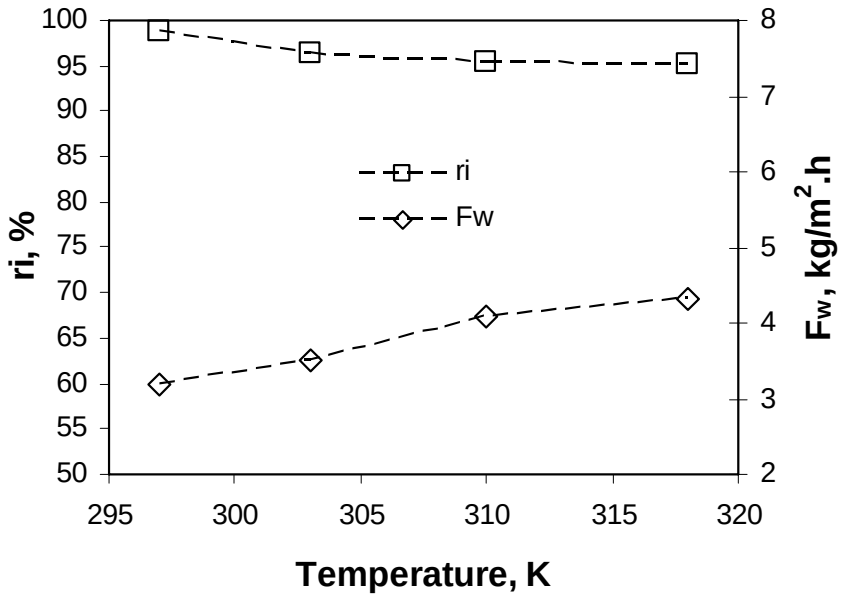

Fig. 41. Influence of temperature on water flux and ion rejection of zeolite membrane.

6.2 Mechanism of ion separation through zeolite membranes

In this part of work, we present our view of the mechanism of ion separation through polycrystalline zeolite membranes based on the microstructure of zeolite

membranes and physiochemical properties of ions in aqueous solutions. The RO permeation data of ion and water presented in next two chapters will be used to justify the proposed mechanism.

MFI-type zeolites have uniform intracrystalline pores with diameter of 0.56 nm, which is smaller than the size of the hydrated ions in studied solutions. Table 5 lists the hydration numbers and crystallographic sizes of the ions exited in produced water. A nearly perfect ion separation may be achieved on a perfect membrane (i.e. containing zeolitic pores only), as predicted by MD simulation [58]. However, the transport of hydrated ions through polycrystalline zeolite membranes also includes diffusion through intercrystalline gaps and crystal boundaries, which have pore sizes on the nanometer scale [17, 54]. Moreover, ions may also diffuse through the zeolitic channels by ion exchange on the feed side and ion desorption at the permeate side, since the alumina-supported membrane is not pure silicalite even though the synthesis solution is aluminum-free [33]. Nevertheless, ion leakage through the intracrystalline zeolite pores is likely to be minor since the membranes studied in the RO permeation has a very high Si/Al ratio, thereby having a minimum capacity for ion exchange.

Complete rejection of hydrated ions can happen on a perfect membrane, with no intercrystalline pores or other microdefects, only if the ion hydration shell is rigid and all the water molecules in the first shell are tightly bound to the ion during diffusion. The attachment of water molecules to an ion is understood to have a lifetime, which depends on the type of ions [71, 71, 72]. In experiments dealing with aqueous size exclusion, ion chromatography showed that only a portion of the water molecules in the first hydration shell is tightly bound to the ion during diffusion [7]. The “apparent dynamic hydration

number (ADHN)" is used to denote the tightly bound water molecules and distinguish them from the equilibrium hydration number in solution. According to the dynamic ionic size with ADHN (see Table 5), complete ion rejection by size exclusion is not possible on the MFI membranes for the ions studied, except for the hydrated Al^{3+}. Small ions like Na^+, K^+, and Cl^- may be able to enter the 0.56 nm zeolite channels, but their diffusivities are expected to be extremely low due to the strong effect of the zeolite framework on the charged ions in the confined spaces.

Table 5. Coordination numbers, experimental ADHN, and sizes of the ions involved in this study [7]

Ion	Crystal ion size (dia.), nm	Coordination number	ADHN	Dynamic ion size with ADHN, nm
Na^+	0.204	6	0.30	0.366
K^+	0.276	6	---	0.420
Mg^{2+}	0.144	6	5.85	0.600
Ca^{2+}	0.246	10	2.09	0.506
Al^{3+}	0.108	6	8.68	0.674
Cl^-	0.362	6	---	0.390

Ion transport through the microporous intercrystalline pores of the charged surface is restricted by the overlapping charged double layers [62, 57]. The average intercrystalline pore size is ~2-3 μm in randomly-oriented MFI zeolite membranes with reasonable quality [17, 54]. The MFI membranes synthesized from aluminum free synthesis solution contain very small amounts of aluminum in the zeolite framework due to slight dissolution of the alumina surface in the high-pH synthesis solution and solid-state diffusion of Al^{3+} during the calcination process [33]. Introduction of a controlled amount of aluminum source into the zeolite framework results in a more hydrophilicly-

charged surface, favorable for water permeation and ion exchange. The substitution of Si^{4+} with Al^{3+} ions produces negative charges on the zeolite surface, which forms charged double layers in the porous structure when contacting liquid water. For a specific membrane, the ion rejection and water flux depend not only on the size and charge density of the solute ion but also on the double layer thickness, which is a function of the ionic strength and temperature of the aqueous solution [34].

The zeolite intracrystalline zeolitic pores and intercrystalline pores are parallel to each other [73]. Water and ions can transport through both the zeolitic pores and the intercrystalline gaps, with most ion permeation occurring through intercrystalline gaps. Ion and water transport through intercrystalline and intracrystalline zeolite pores where overlapping double layers exist is illustrated in Fig. 42.

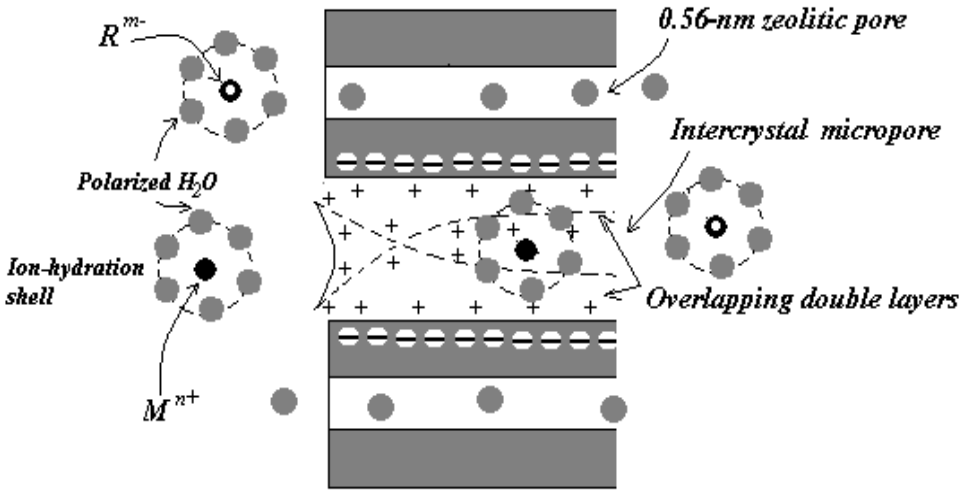

Fig. 42. Schematic illustration of water and ion transport through the MFI zeolite membranes.

In summary, ion and water transport through molecular sieve zeolite membranes is strongly dependent on operating pressure, feed ion concentration and solution chemical

compositions. Water flux of both single-salt solution and DI water increases linearly with the increase of net driving force while the ion permeation is essentially independent on the operating pressure, indicating desirable high hydraulic pressures for enhancement in separation performance. Increasing feed ion concentration results in an exponential increase of ion flux because both the driving force for ion transport and effective pore size increases with increase of ion concentration due to the diminishing of the electric double layer at increased ion concentration. Reverse osmosis permeation of 0.01 M NaCl solutions in the presence of other multivalent ions indicated that counter-cations have notable effects on water flux and Na^+ rejection of zeolite membranes, whereas counter-anions have minimal influence on the permeation and sodium ion retention. The drastic decline in Na^+ rejection and water flux in the presence of multivalent cations (eg. Ca^{2+} and Al^{3+}) is explained by the surface adsorption of multivalent cations and the strong screen effect on membrane surface charge.

7. EXPERIMENTAL STUY OF ION AND WATER FLUXES THROUGH ZEOLITE MEMBRANES

Previous studies have indicated that zeolite membranes synthesized on α-alumina substrate have a negatively charged surface via several mechanisms including ion substitution in the zeolite framework during membrane synthesis [17], dissociation of surface hydroxyl hydrogen [33], and/or ionization of surface hydroxyl groups [18]. When in contact with liquid water or aqueous solutions, an electrically charged double layer forms at the surface of the zeolite pore walls and restricts ion entrance and permeation, if the double layers are thick enough to overlap at the pore opening. The thickness of the double layer decreases with an increase in ion concentration or in the presence of the membrane's high-valence counter ions (ions with opposite charge as the membrane surface) [19]. The electrostatic exclusion governing ion transport will therefore be strongly dependent on the surface charge of zeolite and the chemistry of the feed solution.

This section reports on project findings concerning the influence of counter-ions on the permeation of NaCl solution when it is permeating through zeolite membranes. Also, the contribution of operating pressure and ion concentration on the water flux and overall ion rejection is investigated through RO permeation tests. The experimental work and results described here will be field-tested using oilfield produced waters.

The ion permeation tests were performed with a crossflow RO permeation setup described in our previous work, but modified to use a tubular separation cell machined in

our laboratory for the RO permeation tests. Figure 43 gives a schematic diagram of the RO separation cell.

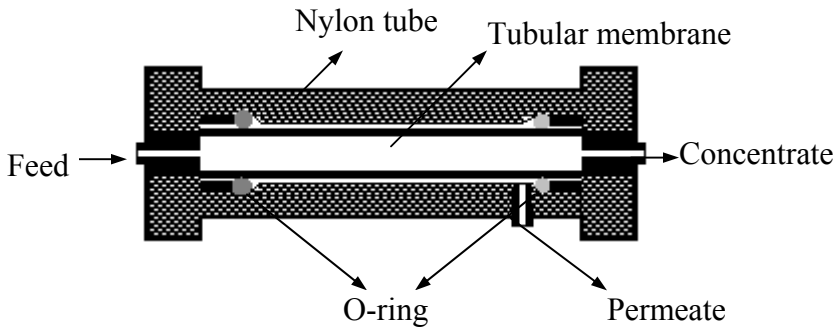

Fig. 43. Schematic diagram of separation cell for tubular membranes

The feed side was connected to a pressured solution tank with a volume of 2.4 liters and the desired transmembrane pressure was maintained by a high-pressure nitrogen cylinder. A constant feed flow rate of 1.5 mL/min was controlled through a needle valve located at the concentrate side. The permeate, defined as the solution permeating through the zeolite membrane, was collected every 8 hr and stored at 5°C in a refrigerator for further composition analysis by ion chromatograph. At these experimental conditions, ion and water permeation reached stabilization in about 48 hr.

Prior to the experiments of RO separation on different salt solutions, the permeation of DI water was tested first at increased operating pressure from 0.69 to 2.76 MPa. Reverse osmosis separations of NaCl solutions were performed with varying operating pressures (0.69 – 2.76 Mpa) and salt concentrations (0.005 – 0.3 M). The NaCl solutions with different concentrations were prepared by dissolving sodium chloride into DI water. Each permeation test lasted for ~80 hr for achievement of stabilized water flux and ion rejection. Both water flux (J_w) and ion rejection (r_i) of a standard 0.01 M NaCl solution were determined periodically throughout the permeation test to evaluate whether

the properties of the membrane had changed due to fouling or were damaged in a previous permeation test.

Figure 44 gives ion rejection and water flux of 0.01 M NaCl solution obtained at different transmembrane pressures. The permeation performance of NaCl solutions at varying salt concentration from 0.005 M to 0.3 M is shown in Fig. 45.

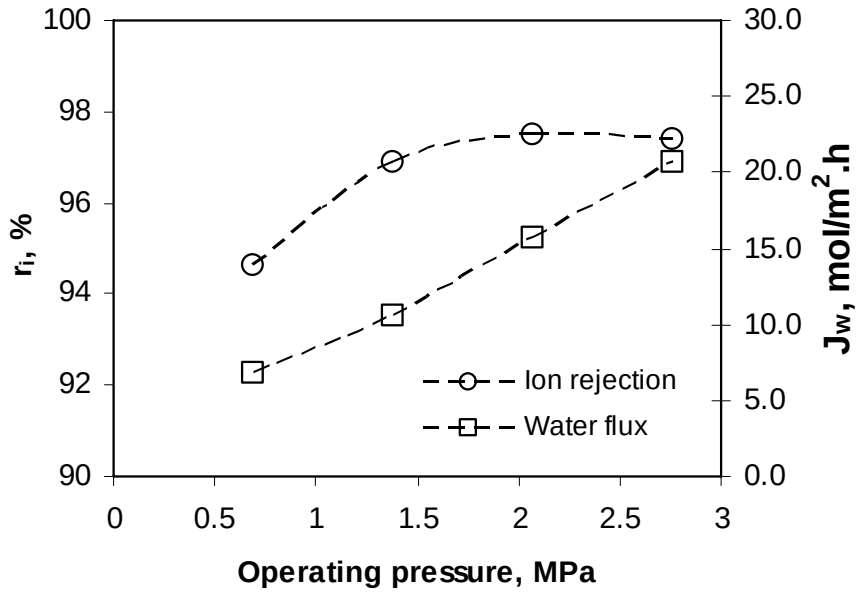

Fig. 44. Effect of operating pressure on RO permeation of 0.01 M NaCl.

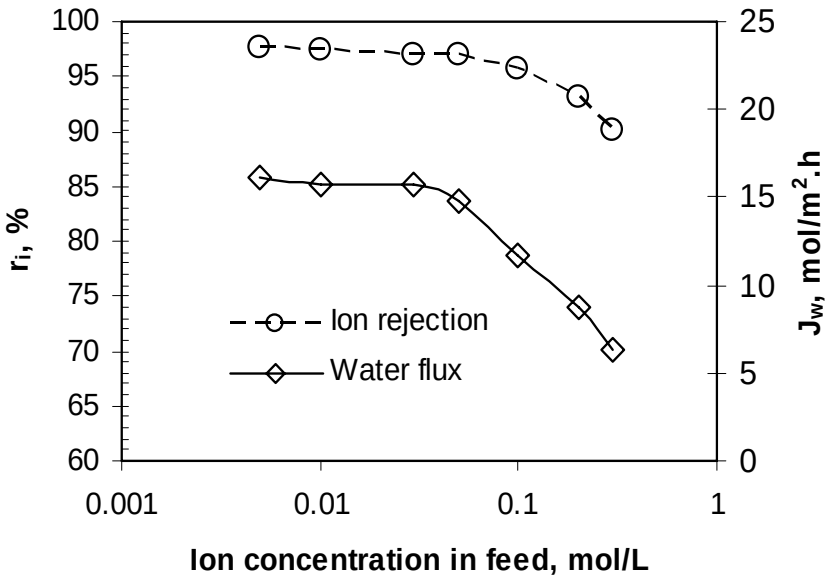

Fig. 45. Influence of ion concentration on water flux and ion rejection (P=2.07 MPa).

A typical produced water sample contains high concentrations of NaCl and other cations and anions such as K^+, Ca^{2+}, Mg^{2+}, and SO_4^{2-} [74]. The presence of these high ions will show their influence on the separation efficacy. Therefore, we investigated how the transport of Na^+ in 0.01 M NaCl solution could be affected by the presence of other counter-ions such as K^+, Ca^{2+}, and Al^{3+} and Cl^- rejection in the presence of Br^-, SO_4^{2-}. Six salt solutions were prepared by adding sodium chloride and another salt having the same cation (Na^+) or anion (Cl^-) into DI water. Each solution was forced to flow through the membrane surface and the permeate solutions were collected every 8 hr for water flux and ion rejection measurement. The chemical composition of the six solutions and the RO permeation results of these multicomponent solutions are given in Table 6. All permeation tests were carried out at a transmembrane pressure of 2.07 MPa.

Table 6. Reverse osmosis results of multicomponent solutions

Solution	J_w, mol/m^2.h	Ion rejection (%)		
		Na^+	Cl^-	Other ions
DI water	17.9	N/A	N/A	N/A
0.01 M NaCl	15.7	97.4	97.4	N/A
0.01 M NaCl+0.01 M KCl	17.8	95.2	95.3	96.1 (K^+)
0.01 M NaCl+0.01 M $CaCl_2$	13.2	77.7	89.6	94.7 (Ca^{2+})
0.01 M NaCl+0.01 M $AlCl_3$	8.9	72.4	93.7	100 (Al^{3+})
0.01 M NaCl+0.01 M NaBr	15.9	96.9	96.1	97.1 (Br^-)
0.01 M NaCl+0.01 M $Na_2SO_4^{2-}$	14.7	98.3	95.9	99.2 (SO_4^{2-})

7.1. Operating pressure and feed concentration

Water flux dependence on operating pressure and feed concentration can be well-explained by the conventional solution-diffusion model. The net driving force for water transport across a zeolite membrane is the pressure difference between transmembrane pressure and reverse osmosis pressure,

$$J_w = -K_w \cdot \frac{dp}{d\delta} = K_w \cdot \frac{[\Delta P - \Delta\pi]}{\delta} \qquad (5)$$

where K_w is the water mass transfer coefficient through the membrane. The osmotic pressure $\Delta\pi$, is given by van's Hoff equation,

$$\Delta\pi = \sum(C_{i,f} - C_{i,p})RT = \sum r_i C_{i,f} RT \qquad (6)$$

where r_i is ion (i) rejection, %; $C_{i,f}$, is feed molar concentration of ion i, mol/L; R is ideal gas constant, 0.0821 (L. atm/ K. mol), and T is absolute temperature, K. Substituting eq. (6) into eq. (5), water flux is obtained:

$$J_w = \frac{K_w}{\delta} \cdot [\Delta P - \sum r_i RTC_{c,f}] \quad (7)$$

The permeation data in Fig. 44 are recalculated and plotted in Fig. 46, which gives the dependence of water flux on the driving force calculated from eq. (7). For both the 0.01 M NaCl solution and DI water, water flux increases linearly with the increase of driving force ($\Delta P - \sum r_i RTC_{c,f}$) throughout the tested pressure range.

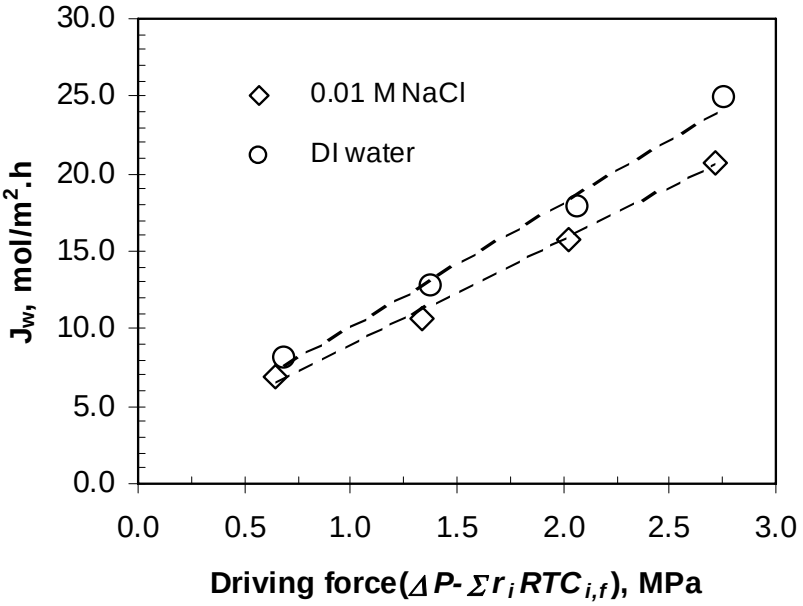

Fig. 46. Permeate flux of 0.01 M NaCl and DI water as a function of net driving force.

At the same operating pressure (P=2.07 MPa), the permeation driving force decreases with an increase in ion concentration because of the increased osmosis pressure at high ion concentrations. Figure 47 shows water flux as a function of the net driving force, caused by difference in feed concentration. A good linear relationship between the water flux and net driving force is obtained and the water transport coefficient (K_w) is calculated with a value of 2.15×10^{-9} $mol/(MPa \cdot m \cdot s)$. The positive y-intercept of the plot gives water flux of 0.259 $mol/m^2.h$ when the trans-membrane pressure is equal to

the reverse osmosis pressure. Conventional RO theory suggests that no water flux exists at zero net driving force [75]. The polycrystalline zeolite membranes contain both unique zeolitic pores with uniform pore size of 0.56 nm and intercrystalline pores with a size distribution ranging from subnanometer to a few nanometers [34]. A perfect zeolite membrane (single crystal with only zeolitic pores) shows nearly 100% ion rejection, as revealed by computer simulation [58]. However, a small amount of ions could leak from the non-selective intercrystalline pores in real polycrystalline zeolite membranes during RO permeation tests, resulting in water permeation at zero net driving force.

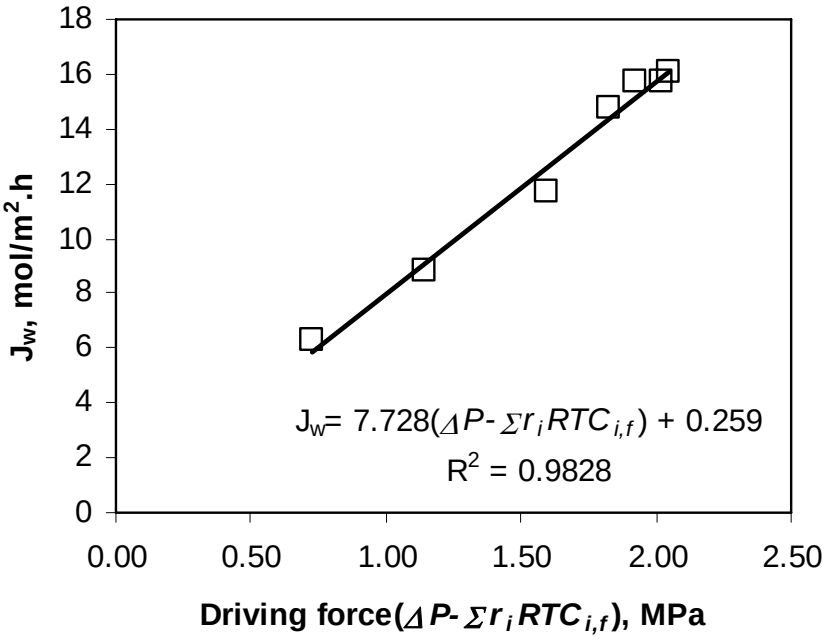

Fig. 47. Water flux of NaCl solutions as function of driving force, varying with ion concentration.

The concentration gradient across the membrane is the driving force for ion permeation through zeolite membranes. Unlike the linear relationship for polymeric membranes usually observed [75], ion flux in zeolite membranes increases exponentially with the concentration gradient across the membrane, as shown in Fig. 48. Our previous

study indicated that ion transport through zeolite membranes is a function of concentration gradient, pore entrance selectivity, membrane thickness, and ion diffusivity inside zeolite microchannels [69]. Ion flux through zeolite membranes is therefore expressed in the following equation,

$$J_i = \frac{D_{i,C}\alpha}{\delta} \cdot [C_{i,f} - C_{i,p}]^{\beta} \qquad (8)$$

where $D_{i,C}$ is ion diffusivity in the zeolite microchannel, m^2/s; α is the pore entrance selectivity; β is the power factor; and δ is membrane thickness, m.

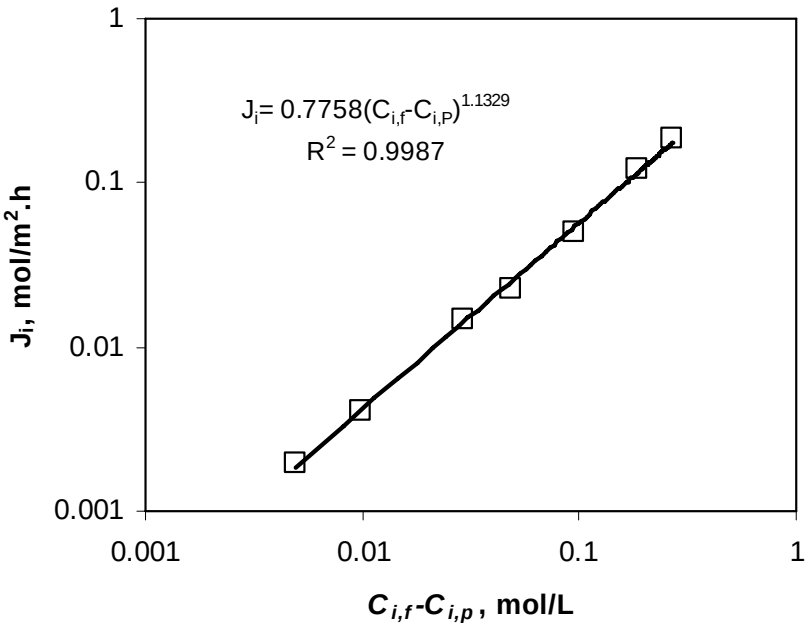

Fig. 48. Regression of ion flux versus the salt concentration gradient across a zeolite membrane.

The rapid increase of ion flux as feed concentration increases in the zeolite membrane is explained by the changes in surface property and pore structures. Zeolite has a negatively charged surface due to the dissociation of surface hydroxyl groups [18]. When in contact with aqueous solutions, an electrically charged double layer forms at the

surface of the zeolite crystals. With increase in ion concentration, the double layer shrinks due to the screening effect of counter ions on the surface charge [76], resulting in an increase of the "effective" pore size for ion transport [77] and an exponential increase in ion flux. Increasing operating pressure increases the ion rejection efficiency because the water flux increases linearly with increase of operating pressure, while ion permeation is only a function of feed concentration and is independent of the operating pressure.

7.2. Influence of counter ions

Figure 49 gives the water flux of DI water and multicomponent solutions as a function of the net driving force ($\Delta P - \sum r_i RTC_{c,f}$). Each solution contains equimolar sodium chloride and another salt with identical co-anions or cations such as KCl, $CaCl_2$, $AlCl_3$, NaBr, or Na_2SO_4. We choose K^+, Ca^{2+}, and SO_4^{2-} as co-ions to study their influences on the transport of NaCl because these ions are usually present in produced water [74]. Other co-ions such as Br^- and Al^{3+} were also studied for the comparison of the ion valences. Remarkable changes in water flux are observed for the solutions having the same anion but different cations such as NaCl/KCl, NaCl/$CaCl_2$ and NaCl/$AlCl_3$. The different slope of water flux versus net driving force suggests that the water flux of electrolyte solutions in zeolite membranes is also dependent on the solution chemistry.

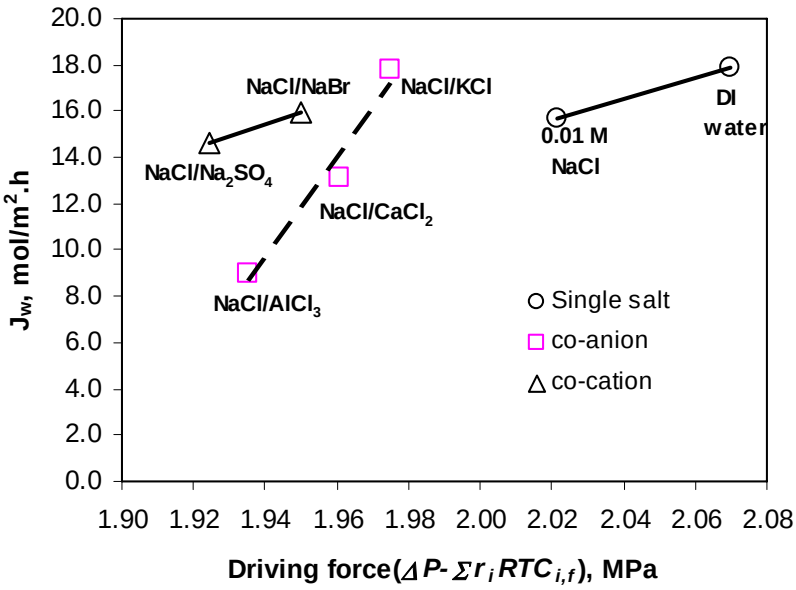

Fig. 49. Permeate flux of multicomponent solution as function of driving force.

In dilute solutions, the solvation of Na^+ is independent of the solution chemistry because the ion-ion interactions are negligible [7]. The Na^+ and water mobility in the zeolite microchannel should therefore be invariable in the presence of other counter-ions. However, it was observed that both water flux and Na^+ rejections in the multicomponent solutions are strongly dependent on the counter-ions, as shown in Figs. 50–51. It is very likely that the presence of other cations or anions in the NaCl solution changes the surface charge or micropore structure of zeolite membranes, with the resulting variation in water flux and Na^+ rejection. The presence of the counter-anion (ions with a similar charge to the membrane's) in 0.01 M NaCl solution hardly affects the water flux, whereas the presence of the counter-cation (Ca^{2+} and Al^{3+}) results in a considerable decline in water flux from 15.7 mol/m^2.h for a single 0.01 M NaCl solution to 8.9 mol/m^2.h for a mixed-salt solution containing 0.01 M NaCl+0.01 M $AlCl_3$. It is also observed that the addition of KCl into 0.01 M NaCl solution results in a considerable increase of water flux from 15.7 to 17.8 mol/m^2.h. Apparently, decline in net operating pressure is not sufficient

to explain such a variation in water flux. Besides the dissociation of surface hydroxyl groups, [18] atom substitution of Si^{4+} in zeolite framework by Al^{3+} from the dissolution of α-alumina substrate in the strong basic synthesis solution also results formation of charged surface [33]. When in contacting with electrolyte solution, cations will be absorbed on the internal and external surfaces, resulting in a considerable decline in effective pore size and decrease in water flux [69], while the anions (Br^- and SO_4^{2-}) show minimum influence on water permeation. On the other hand, the transport of electrolyte solution in microchannels with pore radii close to the MFI-type zeolite is not a single-file movement [13], which means the water molecules overtake the ions in zeolite pores during the permeation process. The water mobility in a zeolite-like microchannel is therefore dependent on the ion mobility and ion-water bonding strength [14, 77]. As ion-water bonding strength decreases, the water flux increase in an order of $J_{w,Al^{3+}} < J_{w,Ca^{2+}} < J_{w,Na^+} < J_{w,K^+}$.

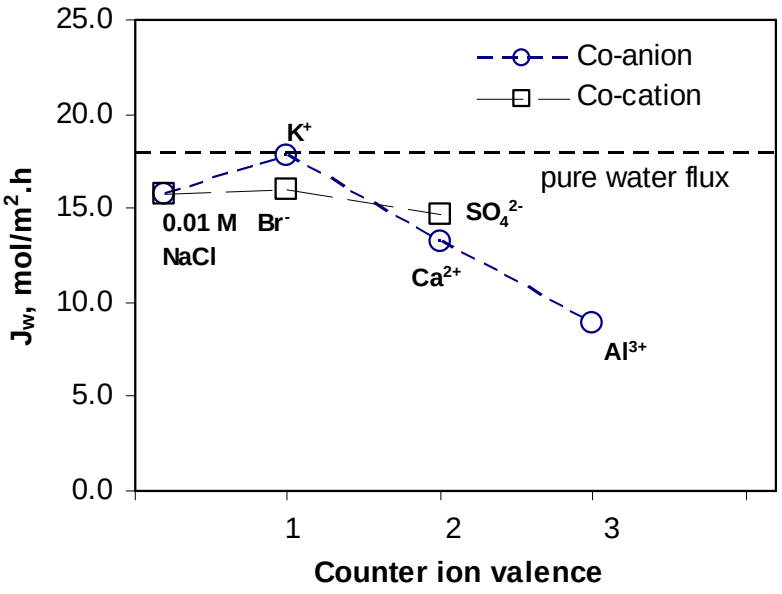

Fig. 50. Dependence of permeate water flux on counter-ions with different valences.

Simultaneously measured Na^+ rejection as a function of counter-ions with different valences is shown in Fig. 51. Similar to the influence of counter-ions on water flux, only a minor variation of Na^+ rejection is observed in the presence of counter-anions. A considerable decline in Na^+ rejection, from 97.4% to 72.4%, was observed when high valence cation (Al^{3+}) was present in the 0.01 M NaCl solution. This observation is different with regard to the permeation of a single-salt solution, in which salt rejection increases with increase of valence of both cation and anions.

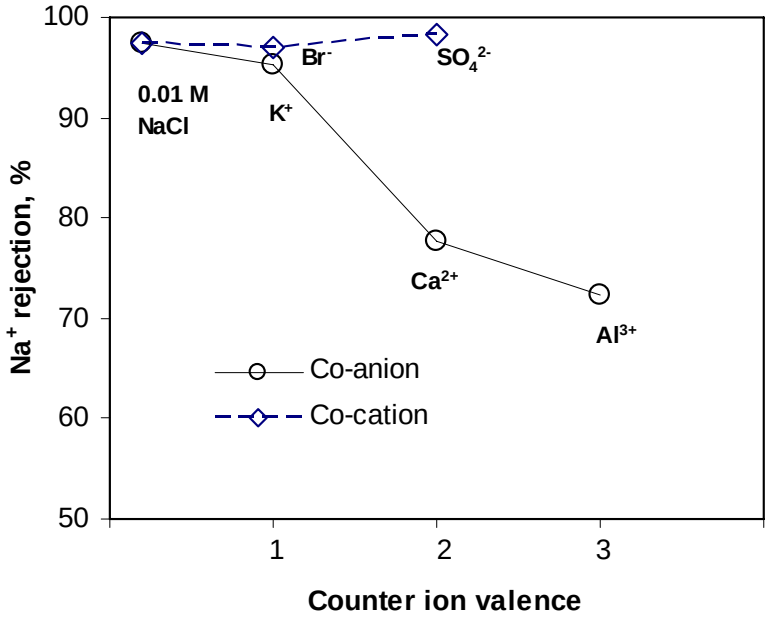

Fig. 51. Dependence of Na^+ rejection on counter-ions with different valences

High rejection of Na^+ in the presence of the multivalent anion (SO_4^{2-}) is explained by the classical Donnan exclusion theory, which suggests that negatively-charged membranes show higher ion rejection for those having an identical charge and higher valence [78]. In the presence of multivalent cations (Ca^{2+}, and Al^{3+}), the charged double layer diminishes to the "Helmholtz" layer because of the strong screening effect of multivalent cations on the surface potential of zeolite membranes, resulting in the

opening of intercrystalline pores for small ion (i.e. Na^+, dia. ~ 3.66 Å) transport. However, for large multivalent cations (i.e. Ca^{2+}, dia. ~ 5.06 Å, and Al^{3+}, dia. ~6.74 Å) [7], the openings of the intercrystalline pores are not sufficiently large for these ions to enter and transport, leading to high ion rejection for the multivalent cations such as Ca^{2+} as well as Al^{3+}.

Ion and water transport through molecular sieve zeolite membranes is strongly dependent on operating pressure, feed ion concentration and solution chemical compositions. Water flux of both single-salt solution and DI water increases linearly with the increase of net driving force while the ion permeation is essentially independent on the operating pressure, indicating desirable high hydraulic pressures for enhancement in separation performance. Increasing feed ion concentration results in an exponential increase of ion flux because both the driving force for ion transport and effective pore size increases with increase of ion concentration due to diminishing of the electric double layer at increased ion concentration.

Reverse osmosis permeation of 0.01 M NaCl solutions in the presence of other multivalent ions indicated that counter-cations have notable effects on water flux and Na^+ rejection of zeolite membranes whereas counter-anions have minimal influence on the permeation and sodium ion retention. The drastic decline in Na^+ rejection and water flux in the presence of multivalent cations (eg. Ca^{2+} and Al^{3+}) is explained by the surface adsorption of multivalent cations and the strong screen effect on membrane surface charge.

The results of this experiment suggest that MFI-type zeolite membranes can be used for desalination of produced water and other radioactive wastewater in which

polymeric membranes cannot be applied. The presence of high valence cations will reduce the ion rejection rate and also cause a decline in the water flux.

8. COMPETITIVE DIFFUSION OF ION/WATER THROUGH ZEOLITE MEMBRANES

In this study, ion rejection and water flux of the alkali metal ions have been measured through RO onto a good-quality silicalite membrane as a function of temperature. The ion and water transport behavior in the MFI membrane are discussed below, and the experimental data was used to develop a phenomenological mass transfer model for the RO process. Chemicals used in this work include lithium chloride (LiCl) (>99%, ACROS), sodium chloride (NaCl) (analytical reagent, Riedel-deHaen®), potassium chloride (KCl) ('Baker Analyzed'® reagent, J.T. Baker), rubidium chloride (RbCl) (>99.0%, ACS reagent, ACROS), and cesium chloride (CsCl) (>99.0%, ACS reagent, ACROS). All the metal chloride solutions used here have a concentration of 0.10M.

8.1. RO permeation tests of alkali metal ions

Reverse osmosis experiments were first carried out for 0.10 M LiCl solution in a temperature range of 10 to 60°C to study the effect of temperature on ion and water transport behavior. Li^+ was used in the beginning instead of Na^+ because the residual Na^+ trapped in the membrane and support during the synthesis process was difficult to remove. The same membrane was then used for RO experiments with 0.10 M single-salt solutions of other alkali metal chlorides including NaCl, KCl, RbCl and CsCl at 50 °C. The RO experiments for different ions were performed at 50°C so as to increase the amount of permeate samples collected in 12 hr for more reliable IC analysis. Finally, experiments for 0.10 M NaCl solution were conducted in a temperature range of 10 – 50°C on this membrane.

During the experiments, both cation and anion (Cl^-) concentrations were measured for the permeate solutions. The cation/anion molar ratio in the permeate solution was found to be consistent with the stoichiometric ratio of the chlorides (M^+:Cl^-= 1:1), indicating cation-anion paired permeation through the membrane that maintained the electrical neutrality. The concentration of the feed solution was treated as constant in data processing because the permeate flow rate was less than 1.0% of the feed flow rate. Table 7 summarizes the RO results for 0.10 M LiCl and 0.10 M NaCl single-salt solutions at different temperatures. The experimental data for ion and water fluxes are corrected by the volume porosity (ϕ=30%) of the substrate, i.e. $J = \frac{Q}{A_m \cdot \phi \cdot (\Delta t)}$. Here, Q is the quantity of water or ions collected in a time period of Δt; and A_m is the straightforward membrane area, m^2. For both LiCl and NaCl solutions, raising temperature increased the water and ion fluxes. The ion rejection rate, however, was only slightly affected by temperature in the tested temperature range because the ion hydration numbers do not vary much with a modest change of temperature [9].

Table 7. Water and ion fluxes and ion rejection by reverse osmosis on the MFI zeolite membrane at applied trans-membrane pressure of 2.75 MPa

T, °C	0.10 M LiCl		0.10 M NaCl	
	r_i, %	F_W, mol·m^{-2}·h^{-1}	r_i, %	F_W, Mol·m^{-2}·h^{-1}
10	99.3	3.57	97.2	3.90
30	99.0	3.84	98.0	5.67
50	98.8	5.91	98.7	6.45
60	98.7	7.17		

Figure 52 presents the ion rejection versus the crystallographic sizes of alkali metal ions at 50°C, and Fig. 53 compares the water and cation fluxes for 0.10 M alkali chloride solutions at the same temperature. The ion rejection decreased with increasing in crystallographic ion size in the order of $r_{Li^+} > r_{Na^+} > r_{K^+} > r_{Rb^+} > r_{Cs^+}$. The ion flux increased monotonically with ion crystallographic size from F_{Li^+} (4.26×10^{-4} mol/m^2·h) to F_{Cs^+} (1.90×10^{-3} mol/m^2·h). The water flux exhibited a trend of increasing, then decreasing as a function of ion (size) in the solutions, with a maximum flux appearing for the KCl solution.

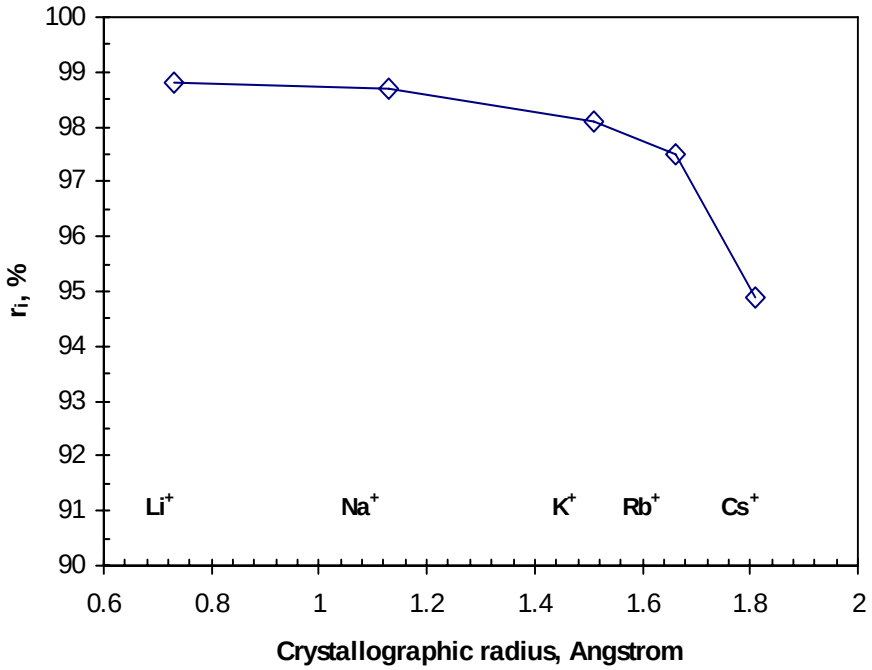

Fig. 52. Alkali ion rejection on the MFI-type zeolite membrane as a function of ion size at 50°C.

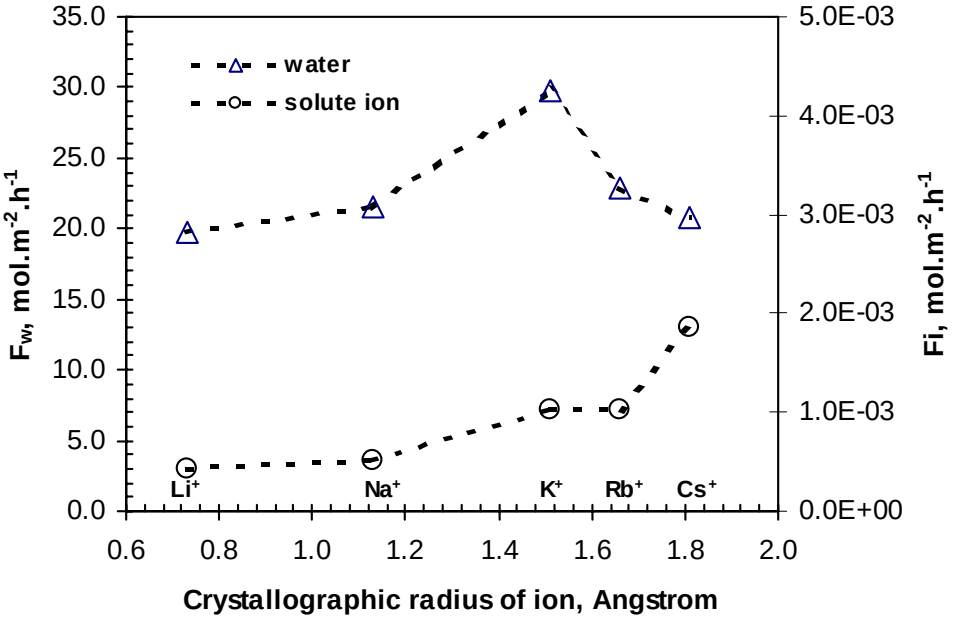

Fig. 53. Ion and water fluxes in 0.10 M alkali metal chloride solutions on the MFI membrane as functions of ion size at 50 °C.

8.2. RO models for dilute ionic solutions

The water permeation through zeolite membranes can be obtained through the classical solution-diffusion model. For dilute systems, $\overline{V}_w \pi = n_w RT$, the water flux and water diffusivity are given by

$$J_{w,D} = -K_w \cdot \frac{dp}{d\delta} = K_w \cdot \frac{[p_f - p_p - \Delta\pi]}{\delta} \qquad (9)$$

$$D_w = K_W \cdot v_w \cdot \frac{RT}{\overline{V}_w} \approx K_w^0 \cdot (RT) \cdot \exp\left(\frac{-E_{W,D}}{RT}\right) \qquad (10)$$

where v_w is the molar volume of water, m^3/mol; P_f and P_p are operating pressures in the feed and permeate sides respectively, Pa; $\Delta\pi$ is the osmotic pressure of the tested

solution, *Pa*; and $E_{W,D}$ is the overall activation energy for water permeation in zeolite membranes, *J/mol*.

A three-step mass transfer model is proposed for ion transport through the zeolite membrane, as depicted in Fig. 54. Step 1 is the entry of ions into zeolitic pores from the bulk feed, assuming concentration polarization is negligible due to the low water flux; Step 2 is the diffusion of ions from the feed-side end of the zeolite channel to the permeate-side end; and Step 3 is the exit of ions from the zeolite channel to the permeate stream. This model also assumes that ion leakage through the intercrystalline pores is negligible for dilute solutions, because ion rejection at nanoscale intercrystalline pores is well above 90%, and the area fraction of the intercrystalline pores is below 1% in a good-quality MFI membrane. Obviously, the key to quantitative utilization of the proposed model is the calculation of x_1 and x_2, the ion concentrations or mole fractions in the two ends of a zeolite channel. The x_1 and x_2 values are different from those in the feed and permeate solutions because of the selectivity at the zeolite pore openings [58, 78]. x_2 can be assumed to be the same as the composition in the permeate for a dilute feed. x_1 can be obtained in two different ways based on different ion-surface interactions: (1) inert membrane surface as assumed in the MD simulations where x_1 is determined by the probability of ion-surface collision and success in entering the pores [79]; and (2) electrostatic sorption of ions on the MFI surface (SiO_2) [18, 80]. In the following sections, phenomenological ion transport models will be derived for each mechanism. The two models constructed for the two different mechanisms were found to have identical mathematical form.

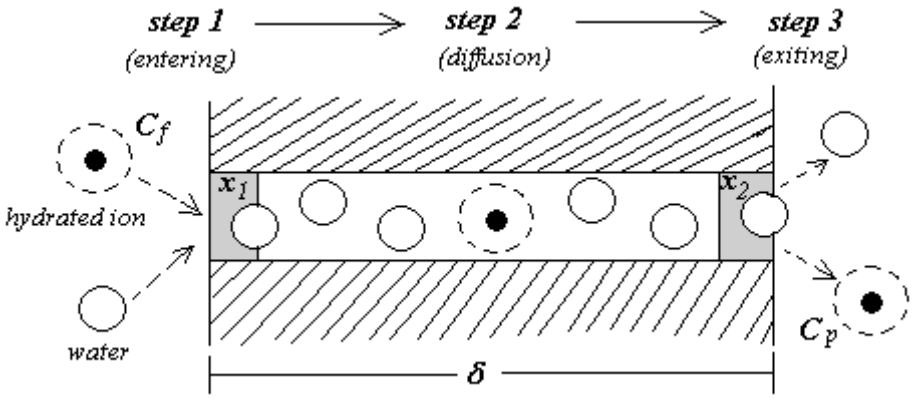

Fig. 54. Schematic showing the three-step molecular transport through a zeolitic channel.

(1) Inert zeolite surface and size-selectivity at zeolitic pores. In the first step of RO permeation, hydrated ions first overcome the energy barrier at the zeolite pore entrance and enter the zeolite channel. The energy barrier could be imposed by partial dehydration of the hydrated ion upon collision at the pore entrance [78]. Thus, the rates of ions entering the zeolite pores are dependent on the numbers and energy profiles of ion molecules in the feed/zeolite interface zone. Also, to maintain electrical neutrality in the zeolite and on the two sides of the membrane at steady state, a cation-anion coupled flow is assumed. This assumption can be justified by experimental observation of the M^+/Cl^- ratio in the permeate. The second step is the ion/water competitive molecular diffusion in zeolite microchannels. The driving force for the ion diffusion is the ion concentration gradient inside the channel, $dx/d\delta$, rather than the straightforward chemical potential gradient calculated from the concentration difference between the feed and the permeate solutions, $(C_{i,f}-C_{i,p})/\delta$. The third step occurs when the molecules exit the channel to the permeate solution. The mass transfer resistance of the third step is expected to be insignificant compared to Steps 1 and 2 [81].

At the membrane/feed interface region, only those hydrated ions with energy higher than the energy barrier at the pore entrance can enter the zeolite channel. The number of ions with such high energy is given by $n_i^0 = K_1 C_{i,f} \exp\left(\frac{-E_1}{RT}\right)$ according to the Boltzmann distribution. Here, $(K_1 C_{i,f})$ is the total number of ions in the interface region and $C_{i,f}$ is the feed concentration. E_1 is the threshold energy. The frequency of ion collision with the pore entrance depends on the energy of the ions; and thus can be expressed by $f = f_0 \exp\left(\frac{-E_2}{RT}\right)$, where f_0 is the pre-exponential factor. E_2 is the average energy of the ions. Thus, the rate of ion entering the zeolite pores, $J_{i,1}$, can be obtained by:

$$\begin{aligned} J_{i,1} = n_i^0 f\eta &= \left[K_1 C_{i,f} \exp\left(\frac{-E_1}{RT}\right)\right] \cdot \left[f_0 \exp\left(\frac{-E_2}{RT}\right)\right] \cdot \eta \\ &= (K_1 C_{i,f} f_0 \eta) \exp\left(\frac{-(E_1+E_2)}{RT}\right) = K_1^{'} C_{i,f} \exp\left(\frac{-E_3}{RT}\right) \end{aligned} \quad (11)$$

where η is the probability for an ion to successfully enter the zeolite pores during a collision; $E_3 = E_1 + E_2$; and $K_1^{'} = K_1 f_0 \eta$. Similarly, the rate of water molecules entering the zeolite pores can be expressed by:

$$J_{w,1} = K_2^{'} C_w \exp\left(\frac{-E_4}{RT}\right) \quad (12)$$

where C_w is the concentration of water (mol/m^3); $K_2^{'}$ has the same physical meaning as $K_1^{'}$; and E_4 is the energy for water molecules to enter the zeolite pores. For dilute solutions, the ion concentration in the zeolite channel on the feedside:

$$C_{i,f}^{'} \approx (J_{i,1}/J_{w,1})C_w = \frac{K_1^{'}}{K_2^{'}} \cdot C_{i,f} \cdot \exp\left(\frac{-(E_3 - E_4)}{RT}\right) \quad (13)$$

where C_w is the molar concentration of water (mol/m^3). The selectivity of Step 1 is defined as:

$$\alpha_{i,1} = \frac{x_1/(1-x_1)}{x_f/(1-x_f)} \approx \frac{x_1}{x_f} \approx \frac{J_{i,1}/J_{w,1}}{x_f} \approx \frac{J_{i,1}/J_{w,1}}{C_{i,f}/C_w} \quad (14)$$

where x_f is the mole fraction of ion in the feed solutions. Combining equations (12 ~ 14), one obtains the size- or shape-selectivity at the pore entrance $\alpha_{i,1}$:

$$\alpha_{i,1} = K^{'} \cdot \exp\left(\frac{-\Delta E_{i/w}}{RT}\right) \quad (15)$$

where the constant $K^{'} = K_1^{'}/K_2^{'}$ and $\Delta E_{i/w} = E_3 - E_4$.

The ion transport rate in the zeolite channel (Step 2) can be described by the Fick's law equation:

$$J_{i,2} = D_{i,c}\frac{dC_i^{'}}{d\delta} = D_{i,C}^{0}\exp\left(\frac{-E_{i,c}}{RT}\right)\cdot\frac{C_{i,f}^{'} - C_{i,p}^{'}}{\delta} \quad (16)$$

where δ is the length of the zeolite channel, which is approximated by the membrane thickness, and $D_{i,c}$ is the ion diffusivity inside the zeolite channels. Because $C_{i,f} >> C_{i,p}$, it is reasonable to assume that $C^{'}_{i,f} >> C^{'}_{i,p}$. Thus equation (16) is simplified as

$$J_i = J_{i,1} = J_{i,2} = \left[D_{i,C}^0 \ \exp\left(\frac{-E_{i,c}}{RT} \right) \right] \cdot \left[K^{'} \cdot \exp\left(\frac{-\Delta E_{i/w}}{RT} \right) \right] \cdot \left[\frac{C_{i,f}}{\delta} \right] = \alpha_{i,1} \cdot D_{i,c} \cdot \frac{C_{i,f}}{\delta} \quad (17)$$

Equation (17) can be rearranged to be

$$J_i = F_i = K_0^{'} \exp\left(\frac{-\Delta E_i}{RT} \right) \cdot \left[\frac{C_{i,f}}{\delta} \right] \quad (18)$$

which is the phenomenological equation for ion transport from the feed solution to the permeate solution. Here, $K_0^{'}$ is the overall mass transfer coefficient and ΔE_i ($=E_{i,c}+\Delta E_{i/w}$) is the overall activation energy of ion permeation.

(2) ***Ion sorption in zeolite***. In this case, the second step of ion diffusion remains the same as above:

$$J_{i,D} = \frac{D_{i,c}}{\delta} \cdot (C_{i,f}^{'} - C_{i,p}^{'}) \quad (19)$$

where δ is the length of the zeolite channel, and $D_{i,c}$ is the ion diffusivity inside the zeolite channels.

Because of the limitation of the pore diameter of MFI zeolite (~0.56 nm), the electrostatic ion sorption interior zeolite pores cannot be multilayered. Therefore, the ion surface coverage at the pore entrance ($\theta_{i,f}$) and at the end of the zeolite channel ($\theta_{i,p}$) are expressed by the Langmuir equation:

$$\theta_{i,f} = \frac{C'_{i,f}}{C_{T,M}} = \frac{K_i C_{i,f}}{1 + K_i C_{i,f}} \tag{20}$$

$$\theta_{i,p} = \frac{C'_{i,p}}{C_{T,M}} = \frac{K_i C_{i,p}}{1 + K_i C_{i,p}} \tag{21}$$

where K_i represents the equilibrium constant of ions in bulk solution and inside zeolite channel at the interface of the membrane. $C_{i,f}$ and $C_{i,p}$ are the feed and permeate concentrations respectively, *mol/m*^{3}. Thus, $C'_{i,f}$ and $C'_{i,p}$ can be obtained. Substitution for $C'_{i,f}$ and $C'_{i,p}$ in equation (19) gives

$$J_{i,D} = \frac{D_{i,c}}{\delta} \cdot \left(\frac{C_{T,M} K_i C_{i,f}}{1 + K_i C_{i,f}} - \frac{C_{T,M} K_i C_{i,p}}{1 + K_i C_{i,p}}\right) \tag{22}$$

$C_{T,M}$ is a coefficient relating to vacancy concentration in zeolite channels that can be occupied by water, ion or other organic molecules, *mol/m*^{3}. In dilute solutions, Henry's law is assumed to be valid, giving $K_i C_{i,f} << 1$ and $K_i C_{i,p} << 1$. Together with the assumption of $C'_{i,f} >> C'_{i,p}$, equation (22) is simplified to

$$J_{i,D} = (K_i \cdot C_{T,M}) \cdot D_{i,c} \cdot \frac{C_{i,f}}{\delta} \tag{23}$$

Equations (23) and (17) have identical mathematic forms if $\alpha_{i,1} = K_i C_{T,M}$. The dynamics of ions to enter the zeolite pores or the behavior of ion sorption in the pure

silicalite is currently not clear. However, if Step 1 predominates in the overall RO rejection, the ion diffusivity in the zeolite channels ($D_{i,c}$) can be estimated by either equation (17) or equation (23) with the same results. According to the MD simulation [58], rejection of small ions (e.g. Na^+) on small pore zeolite membranes (e.g. ZK-4) is primarily controlled by size selectivity at the pore entrance. Although MD simulation has also indicated that single-file diffusion cannot be observed in idealized zeolite-like channels with subnanometer sizes [10], it is difficult, if not impossible, for water molecules and hydrated ions to pass by each other in the MFI zeolite channels because of the space confinement and interactions between ion and channel wall. Thus, we assume $\alpha_{i,1} \approx [C_{i,p}/C_{i,f}]$ in the estimation of ion diffusivity in the zeolite channels using equation (17).

8.3. Activation energy

Figure 55 shows the Arrhenius plots of ion fluxes during the RO process. The overall activation energies for permeation of Li^+ (ΔE_{Li^+}) and Na^+ (ΔE_{Na^+}) were 20.11 kJ/mol and 13.21 kJ/mol, respectively, as obtained from the slopes of the lines. Assuming that step 1 predominates the overall RO rejection, i.e. $\alpha_{i,1} \approx [C_{i,p}/C_{i,f}]$, ion diffusivities in the zeolite channels, $D_{i,c}$, are calculated using equations (13-18) for Li^+ and Na^+ at different temperatures. The results are presented in Fig. 56. The $E_{Li^+,C}$ and $E_{Na^+,C}$ are estimated to be 11.23 kJ/mol and 9.57 kJ/mol, respectively. Thus, the energies required for Li^+ ($\Delta E_{Li^+/w}$) and Na^+ ($\Delta E_{Na^+/w}$) to enter the zeolite pores are estimated to be 8.88 kJ/mol and 3.64 kJ/mol, respectively.

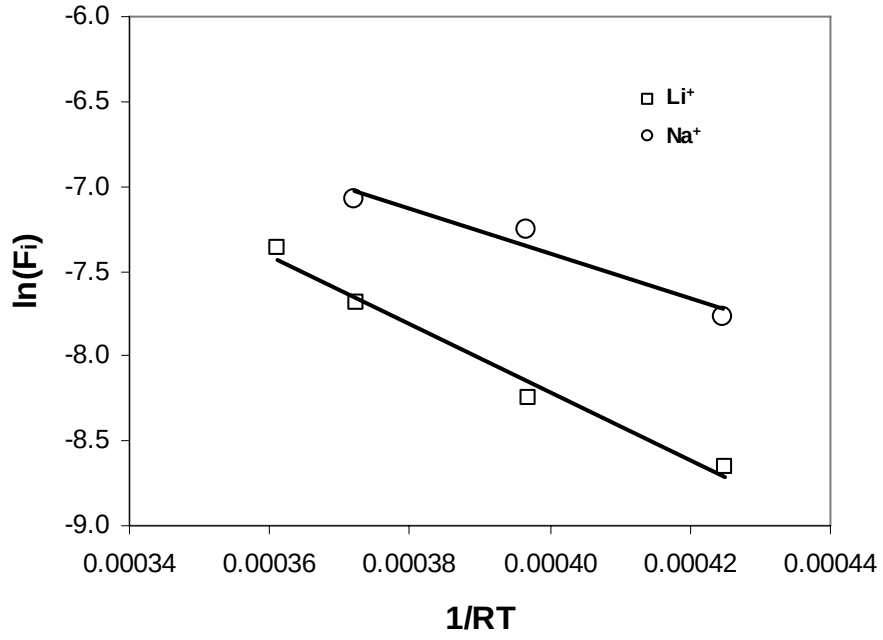

Fig. 55. Arrhenius plots of the ion fluxes for 0.10 M LiCl and 0.10 M NaCl solutions.

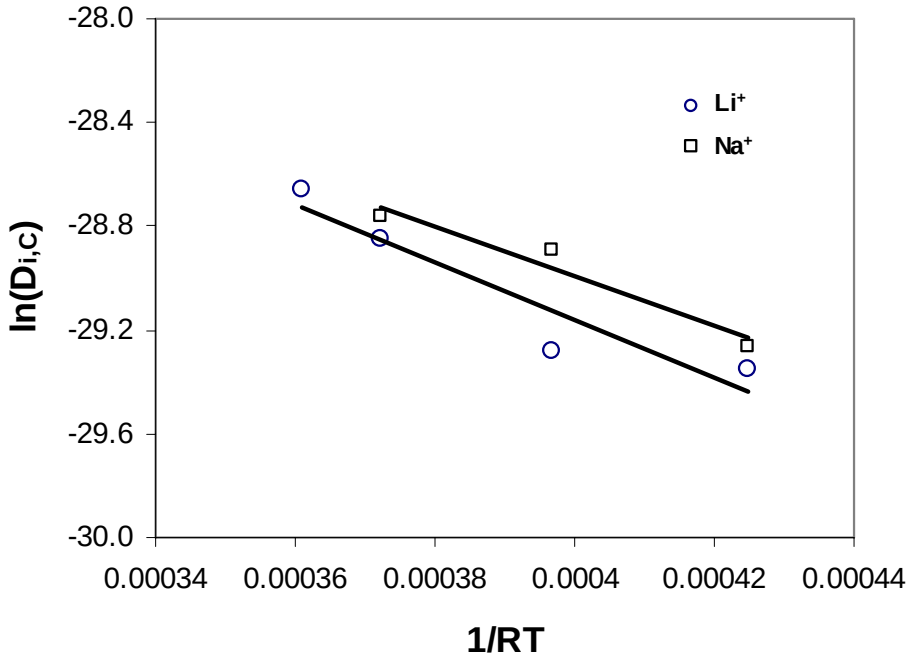

Fig. 56. Arrhenius plots of ion diffusivities in the zeolite channel.

The overall activation energy for Li^+ permeation, ΔE_{Li^+}, was much greater than ΔE_{Na^+} because the charge density of Li^+ is higher than that of Na^+. The dynamic size and dehydration energy of a hydrated ion increase with its electrical charge density [9]. As the ratio of the effective molecular dynamic size to the pore size increases, higher activation energies are needed for the molecule to enter and transport in subnanometer pores [78]. Hydrated ions with large sizes may enter pores of similar or smaller sizes by partial dehydration during collision processes [78]. The stronger bonding between Li^+ and water molecules in the hydration shell [8] requires higher energy for dehydration when entering the zeolite pores [82]. On the other hand, for small ions like Li^+ and Na^+, which tend to stay in the center of the uncharged cylindrical channel in liquid water [10], a higher charge density results in a stronger attraction to the zeolite pore wall with oxygen atoms on the surface that decreases the ion mobility [82].

8.4. Diffusivities of ion and water in zeolite membranes

The effective water diffusivities (K_W) in zeolite membranes were calculated from the permeation data by means of equations (9) and (10). At the assumption of step 1 predominating the overall RO rejection, the pore entrance selectivity, $\alpha_{i,1}$, is obtained from the rejection data by equation $\alpha_{i,1} \approx [C_{i,p}/C_{i,f}]$. The effective diffusion coefficients ($D_{i,C}$) of alkali ions inside silicalite channel at 50 °C are, therefore, calculated from Equation (23) (Table 8).

Table 8. Effective diffusivities of alkali metal ions and water in the zeolite pores at 50°C

Ion	Effective diffusivity		Pore entrance selectivity, $\alpha_{i,1}$
	Ion ($D_{i,C}$, m^2/s)	Water (K_W, m^2/s)	
Li^+	2.96×10^{-13}	1.77×10^{-11}	0.012
Na^+	3.23×10^{-13}	1.93×10^{-11}	0.013
K^+	4.48×10^{-13}	2.68×10^{-11}	0.019
Rb^+	3.44×10^{-13}	2.06×10^{-11}	0.025
Cs^+	3.11×10^{-13}	1.86×10^{-11}	0.051

The zeolite pore entrance selectivity ($\alpha_{i,1}$) varied from 0.012 for Li^+ to 0.051 for Cs^+. The pore entrance selectivity is caused by the difference between the configurational entropy inside the pore and in the free solution. The variation of pore entrance selectivity for different alkali metal ions is attributed to the effective size of hydrated ions and the interaction between the ions and the zeolite pore wall. For small ions, such as Li^+, the entry of an ion into a zeolite microchannel is restricted by its large dynamic size due to strong hydration. The large ions, such as Rb^+ and Cs^+, are more readily dehydrated but have stronger interaction with the pore wall surface, resulting higher entropy variation for ion entry from bulk solution into the zeolite cavity [7, 11].

The diffusivities of the alkali metal ions in the zeolite channels at 50°C and the apparent diffusivities of water in the zeolite membranes during RO are replotted as a function of ion crystallographic size in Fig. 57.

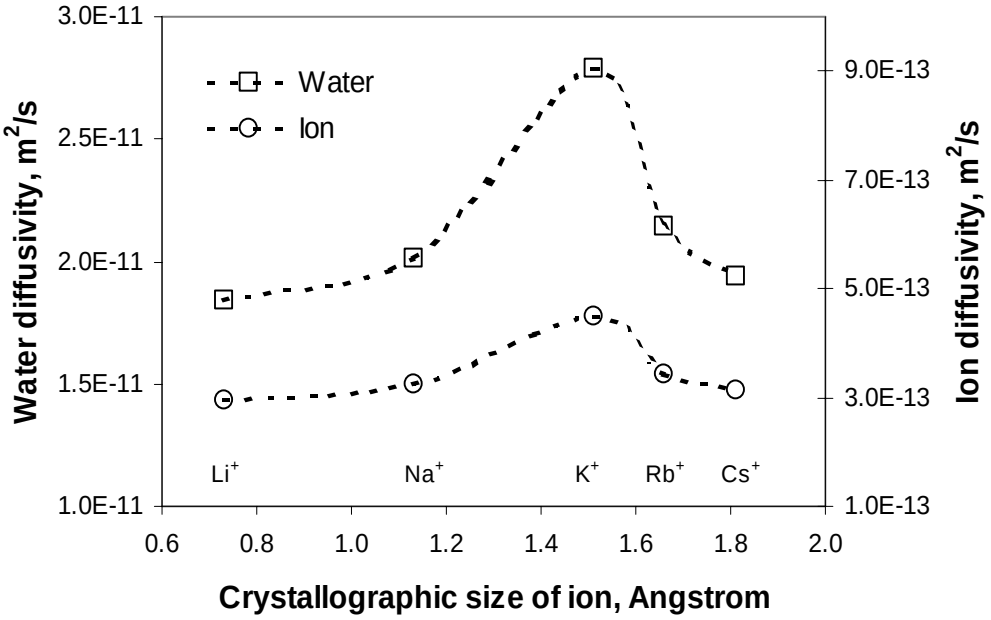

Fig. 57. Effective ion/water diffusivities of alkali metal ions inside MFI zeolite microchannel (T=50°C).

Rather than a monotonic decrease with ion crystallographic size as observed in bulk solutions [63] and uncharged smooth channels [10], the water diffusivities inside the zeolite channels rise to a maximum at K^+ with ion crystallographic size. Such a water permeation behavior in the zeolite membrane is explained by the polarization effect of ions and ion–zeolite interaction. As the size of alkali metal ions increases from Li^+ to Na^+ to K^+, the ion charge center becomes more distant from the surrounding water molecules, resulting in weaker interactions between charged ions and the bound water, thus increasing the water diffusivity. The large ions, such as Rb^+ and Cs^+, might have stronger interaction with zeolite pore wall as observed in the uncharged cylindrical pores [10], thus inhibiting the movement of water molecules. The variation of water diffusivities in the alkali metal solutions followed the same trend as the cation diffusivities. This indicates that, although single-file movement is unlikely to occur in zeolite channels for

the present system, transport of water molecules is strongly affected by the mobility of ions in the solution.

8.5. Influence of dissolved organics on RO performance of zeolite membranes

Dissolved organics are major problems encountered in wastewater treatment by RO membrane technology due to membrane degradation, fouling and strong membrane-organic solute interactions [1, 2]. The dissolved organics in produced water such as fatty acid and low molecule aramatic organics (benzene, toluene and xylene) [83] might show influence on separation performance of zeolite membrane due to their strong adsorption [84]. The influence of dissolved organics on the RO performance of the zeolite membrane were investigated through permeation tests of DI water, 0.10 M NaCl solution, 500 ppm toluene solution and ion-organic-water system (0.10 M NaCl+500 ppm toluene). The mathematical model for water and ion transport in zeolite membrane was modified for depicting the more complicated solution with existence of dissolved organics.

8.5.1 Separation of organic-ion-water system by zeolite membrane

Permeation of DI water on the zeolite membrane was first carried out to study the water permeation without salt and organics. Then, RO separation tests on single-component solutions of 0.10 M NaCl solution and 500 ppm toluene solution were performed respectively. Finally, a binary solution containing 0.10 M NaCl and 500 ppm dissolved toluene was permeated through the zeolite membrane and rejection of both Na^+ and toluene were tested by measuring their concentration changes in the feed and permeate solutions. The toluene concentration in the permeate was analyzed by total organic carbon analyzer (TOC-VCPN) and ion concentrations were analyzed by IC and

atomic adsorption (AA, with organics). Table 9 summarizes the separation results of these solutions together with the water flux of DI water.

Table 9. Influence of organics on the separation performance of zeolite membranes

Solution	Water flux, $Kg/m^2.h$	Ion rejection, %	Toluene rejection, %
DI water	0.333	–	–
0.10 M NaCl	0.285	99.4	–
500 ppm toluene	0.016	–	99.5
0.10 M NaCl + 500 ppm toluene	0.018	77.8	99.8

The zeolite membranes showed very high separation efficiency (>99%) for single-component 0.10 M NaCl solution and 500 ppm toluene solution. The toluene rejection in the binary solution containing 0.10 M NaCl and 500 ppm toluene was virtually the same (99.8%) as that in 500 ppm single component solution. However, the ion rejection decreased from 99.4% to 77.8% at existence of dissolved toluene. The adsorption of organics in zeolite membrane might change the surface properties and micropore structures [85, 86], resulting the decline in ion separation efficiency.

The decline of water flux from 0.333 $kg/m^2.h$ for DI water to 0.285 $kg/m^2.h$ for 0.10 M NaCl solution is consistent with that observed in our other experiments [87], which was explained by the narrowed transport pathways in zeolite membrane due to ion adsorption in zeolite microchannels. Drastic decline in water flux at existence of dissolved toluene was observed on both single toluene solution and the binary solution containing toluene and 0.10 M NaCl solution. Such declines in water flux and ion rejection efficiency at existence of toluene was attributed to the toluene adsorption on the

zeolite surface that reduced the hydrophilicity of the membrane surface and effective zeolite pore size.

8.5.2 Modified mathematical model for dilute organic-ion-water system

It was assumed that water flux decline at existence of organics on zeolite membrane was mainly caused by reduced mass transport pathways. Quantitatively analyzing the interaction between organic and zeolite surface is important for understanding RO performance of membranes in the presence of dissolved organics. In this case, the ion-sorption diffusion model presented in the previous chapter was modified for application in dilute organic-ion-water system.

We assume both ion and hydrocarbons (HC) transport in zeolite membrane through a sorption-diffusion mechanism. The driving force for ion and hydrocarbon migration is the surface coverage of adsorbed molecules. For the same reason of space confinement by zeolite micropores, the hydrocarbon surface coverage at the pore entrance ($\theta_{HC,f}$) and at the end of the zeolite channel ($\theta_{HC,p}$) are expressed by the Langmuir equation:

$$\theta_{HC,f} = \frac{C'_{HC,f}}{C_{T,M}} = \frac{K_{HC} C_{HC,f}}{1 + K_{HC} C_{HC,f}} \tag{24}$$

$$\theta_{HC,p} = \frac{C'_{HC,p}}{C_{T,M}} = \frac{K_{HC} C_{HC,p}}{1 + K_{HC} C_{HC,p}} \tag{25}$$

where K_{HC} represents the equilibrium constant of dissolved hydrocarbons in bulk solution and inside zeolite channel at the interface of the membrane. $C_{HC,f}$ and $C_{HC,p}$ are the feed

and permeate concentrations respectively, mol/m^3. The flux of hydrocarbons through zeolite membranes during RO permeation has a similar mathematical expression as that of ion flux, shown in equation (22):

$$J_{HC,D} = \frac{D_{HC,c}}{\delta} \cdot \left(\frac{C_{T,M} K_{HC} C_{HC,f}}{1 + K_{HC} C_{HC,f}} - \frac{C_{T,M} K_{HC} C_{HC,p}}{1 + K_{HC} C_{HC,p}}\right) \tag{26}$$

The effective zeolite pores for mass transport are partially occupied by ion adsorption ($\theta_{i,f}$) and organic adsorption ($\theta_{HC,f}$). Thus, the fraction of free zeolite channels for water transport (ε) is,

$$\varepsilon = 1 - \theta_{i,f} - \theta_{HC,f} \tag{27}$$

The water flux is, therefore, obtained from the equations (12) and (13),

$$\begin{aligned} J_w &= (1 - \theta_{i,f} - \theta_{HC,f}) \frac{D_w}{RT} \left(\frac{\Delta P - \Delta\pi}{\delta}\right) \\ &= \left(1 - \frac{K_i C_{i,f}}{1 + K_i C_{i,f}} - \frac{K_{HC} C_{HC,f}}{1 + K_{HC} C_{HC,f}}\right) \frac{D_w}{RT\delta} (\Delta P - \Delta\pi) \end{aligned} \tag{28}$$

The parameter of water diffusivity (D_w) can be determined from permeation data of DI water ($\theta_{i,f} = 0$ *and* $\theta_{HC,f} = 0$). Adsorption equilibrium constant K_i and K_{HC} were further obtained from the water flux of single component solutions. All the parameters were calculated from permeation data shown in Table 9 and equation (28) and are listed in Table 10.

Table 10. Parameters of water permeation in an organic-ion-water system

	$D_{w,}\ m^2/s$	K_{i,Na^+}	$K_{HC,\ toluene}$
Parameters	4.62×10^{-11}	0.6	4200.2

The adsorption equilibrium constant of hydrocarbon (K_{HC}) is much larger than that for the ions (K_i) because the former have much stronger interaction with the zeolite surface, resulting in a significant decline in water flux.

9. UPSCALE OF MEMBRANE SYNTHESIS AND INDUSTRY APPLICATION

9.1. Tubular zeolite membranes

Zeolite membranes used in this experiment were synthesized on alpha-alumina tubular substrates. Commercial tubular substrates (OD =10 mm, ID=7.4mm, length=25 cm) were obtained from the Pall Corporation and used as received. The tubular substrates have a two-layered structure as shown in the scanning electron microscope (SEM, JEOL 5800LV) images of Fig. 58, including a macroporous layer 1.3mm thick and a microporous layer 20μm thick. The microporous coating layer has a pore size in the range of 100~200 nm, which is preferable for growing defect-free zeolite thin film. The underlying macroporous layer provides sufficient strength for application at high transmembrane pressures (i.e., ~10 MPa).

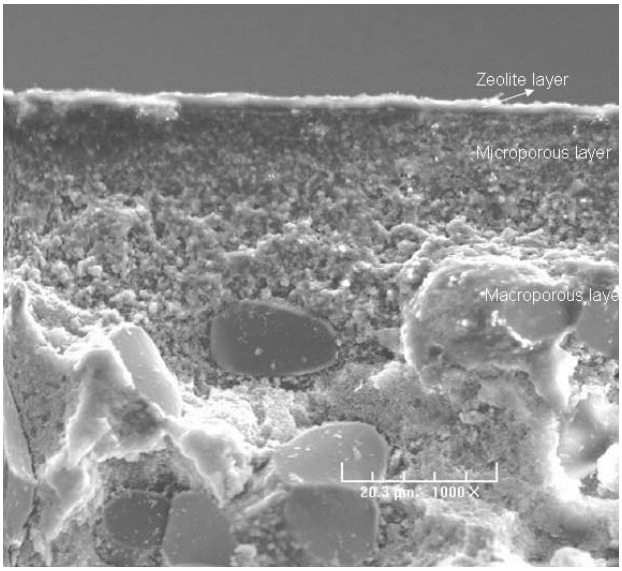

Fig. 58. Cross-section of alpha-alumina tubular substrate (SEM image).

A two-step crystallization was optimized for high-quality membrane fabrication. Differing from conventional secondary growth, in-situ crystallization was used to form a thin zeolite layer on substrate. The followed secondary growth in a synthesis solution without an organic template will further form a permselective zeolite thin layer. The first step of hydrothermal crystallization was carried out at 80°C by using a solution containing 1.08 g NaOH, 15 g fumed SiO_2, and 75 ml 1.0 M TPAOH. The crystallization was carried out at 180°C for 10 hr by rotating the autoclave at constant rate of 1.5 rad/min. After washing, drying and sintering at 500°C, the second step of hydrothermal synthesis was carried out to grow zeolite crystals into a permselective ZSM-5 layer. The synthesis solution for the second step was prepared by dissolving silica colloid (30%, Aldrich), NaOH pellets, aluminum sulfate and deionized water in a Teflon beaker with a molar ratio of 1.0 SiO_2: 41.5 H_2O: 0.38 NaOH: 0.04Al_2O_3.

The rotating synthesis process was described in the previous chapters. The lab-constructed hydrothermal synthesis equipment is shown in Fig. 59. Constant rotating is necessary to synthesize a thin and defect-free zeolite film on a porous support. As shown in Fig. 60, a stainless steel autoclave with Teflon liner was designed for membrane synthesis, which was carried out at hydrothermal condition of 180°C and vapor pressure of 1.0MPa.

Fig. 59. . Lab-constructed rotating equipment for tubular membrane synthesis.

Fig. 60. Teflon-lined stainless steel autoclave for tubular membrane synthesis.

During the membrane synthesis process, the tubular substrate was wrapped on the outside by Teflon tape. In that case, zeolite crystallization only occurs on the interior surface. The zeolite membrane synthesized by the two-step crystallization has a uniform thickness of ~2 μm. The random surface search indicated that the membranes have a good surface coverage and enhanced in-plane growth, as shown in Fig. 61.

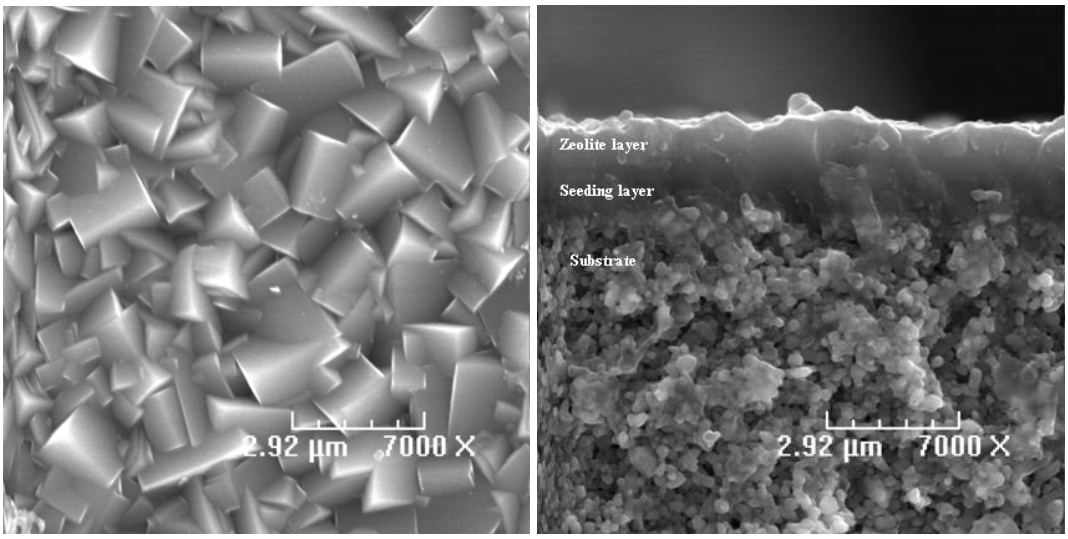

Fig. 61. SEM images of zeolite membranes synthesized by two-step crystallization.

Zeolite membranes on tubular alpha-alumina substrate are shown in Fig. 62. The zeolite membranes have glaze sealing at both ends of the tubular substrate, giving an effective membrane surface area of ~40cm^2.

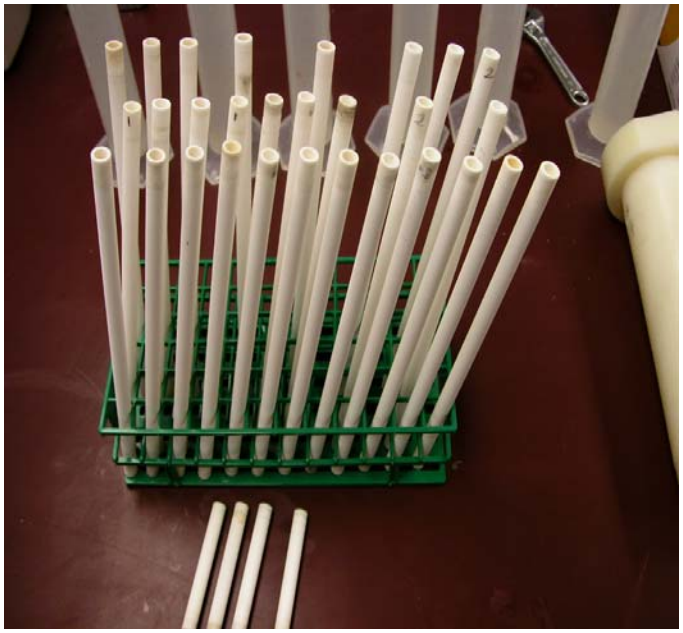

Fig. 62. Tubular zeolite membranes synthesized on commercial alpha-alumina substrate for produced water desalination.

9.2. Scale-up of zeolite membranes and desalination demonstration

To investigate reproducibility, about 80 long-tube zeolite membranes were synthesized by the two-step hydrothermal crystallization. Each individual zeolite membrane was tested for RO permeation on 0.1 M NaCl solution. The tubular zeolite membrane was mounted in a Nylon RO cell in which both ends of the membranes were sealed by O-rings. All the membranes were tested under transmembrane pressure of 3.5 MPa. The water flow rate across the surface of zeolite membrane was adjusted to above 1.0 mL/min by a needle valve located at the concentrate side. The permeate, defined as the solution transport across the membrane, was collected every 12 hr and stored at 5°C for further composition analysis. Ion rejection and water flux of each zeolite membrane were obtained from the RO permeation tests. Figure 63 summarizes the reverse osmosis permeation behavior of zeolite membranes synthesized by two-step crystallization.

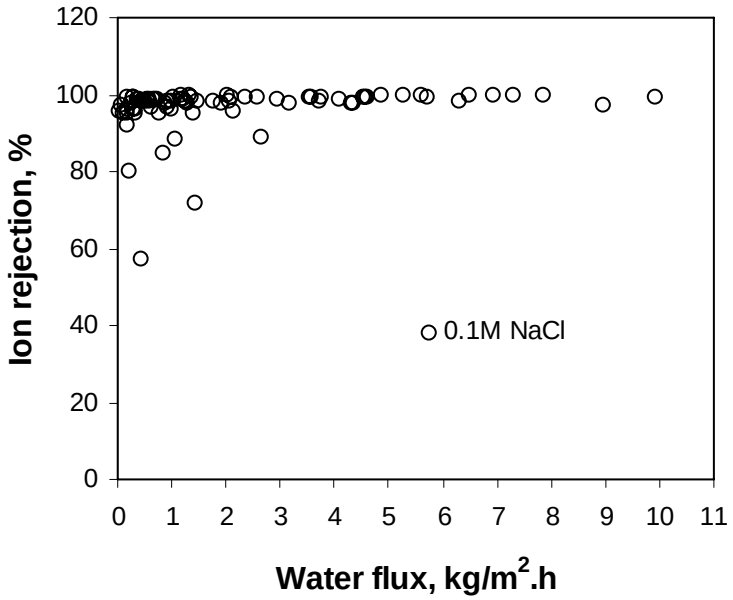

Fig. 63. Summary of RO separation performance of zeolite membranes synthesized by two-step hydrothermal crystallization.

Among the 80 tubular zeolite membranes synthesized with two-step hydrothermal crystallization, 73 zeolite membranes have ion rejection >95%. Four zeolite membranes have ion rejection between 85% and 95%. Three zeolite membranes have low ion rejection with values < 85%. The overall RO performance of the ZSM-5 membranes was investigated by assembling the tubular zeolite membranes into multichannel RO separation cells and testing for cross-flow permeation, as shown in Fig. 64. The 0.10M NaCl solution was pumped through zeolite membrane by a pump (Triplex Cat Pump) with a flow rate of 3.78 L/min. Both the concentrate and the permeate solution are collected and sent back to the feed tank to maintain a constant feed concentration.

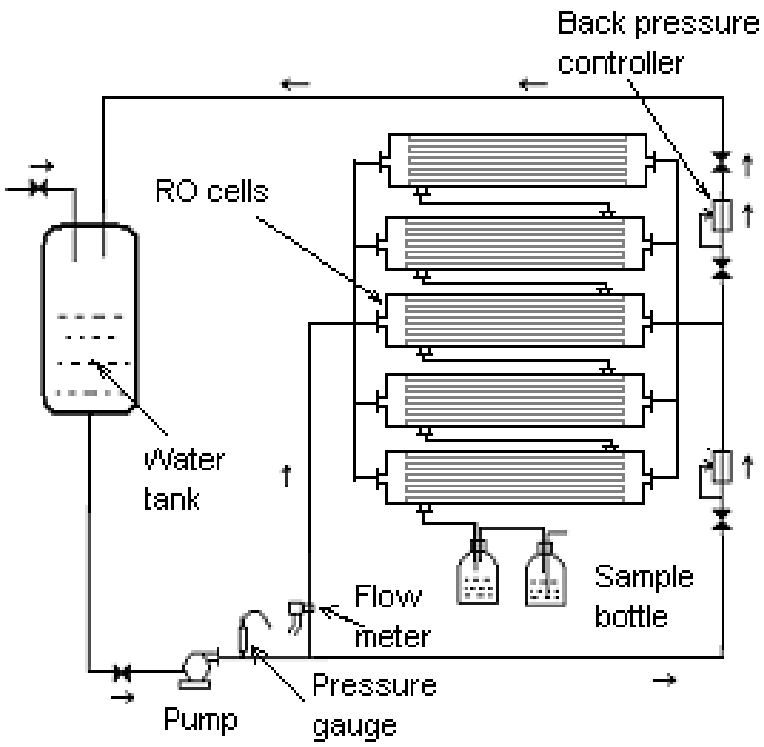

Fig. 64. Schematic diagram of RO demonstration.

9.3. Membrane modules

The process of produced water desalination by tubular zeolite membranes includes a feed stream sweeping across the interior surface of the zeolite membrane and clean water permeating across the membrane under transmembrane pressure. A multiple tube vessel was thus designed for achieving the separation objective. The RO separation vessel has a cylindrical multichannel body and tubular zeolite membranes. The tubular zeolite membranes are fixed into the pipes in the cylindrical vessel body by O-ring sealing at both ends. The inside diameter of the module device is 1.0 mm larger than the outside diameter of the tubular zeolite membranes, providing a gap between the inner surfaces of the module and outside surface of the zeolite membrane for permeate

collection. Figure 65 gives the drawing of a module device together with a tubular zeolite membrane.

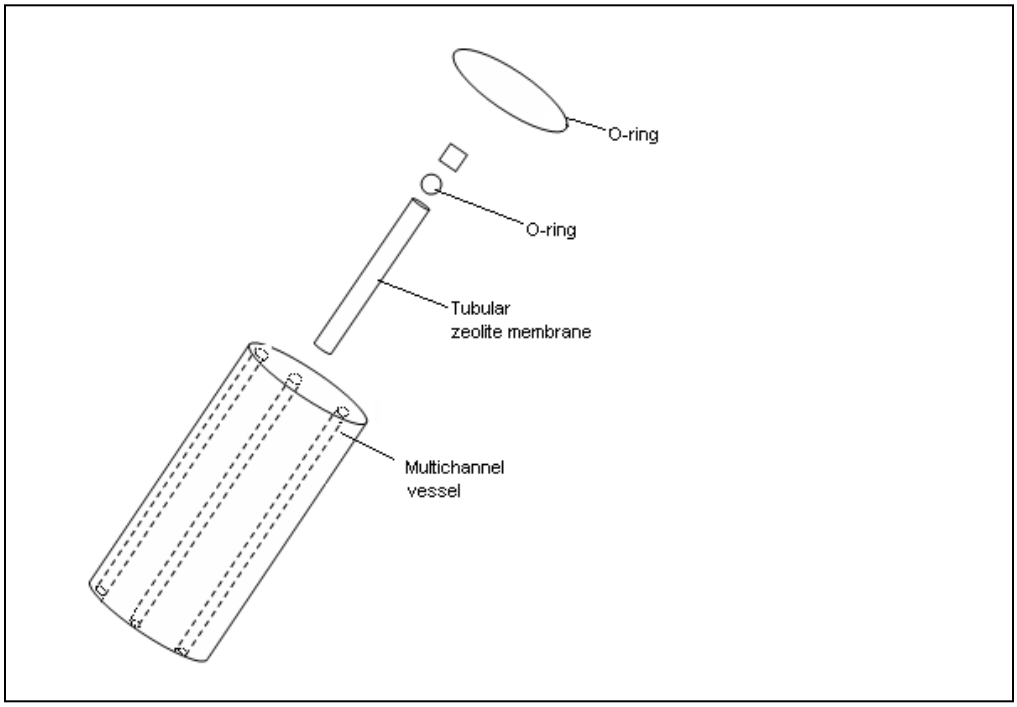

Fig. 65. Schematic diagram of multichannel membrane vessel.

The inlet and outlet are connected to the interior space of the zeolite membranes in which fluid sweeps across the membrane surface. The permeate side is connected to a small area between the membranes' outside surface and the vessel body wall, which is separated from the feed stream by O-rings at both ends of the membrane. Under hydrostatic transmembrane pressure, water transports across the zeolite membrane and accumulates in the permeate side while large ions and organic species are excluded. The material for preparation of the module body is nylon which shows sufficient strength for operating at high pressure and chemical stability in produced water environment. Figures 66 and 67 show the side and top view of the zeolite membrane module.

Fig. 66. Side view of separation module with and without inserting zeolite membranes.

Fig. 67. Top view of separation module with and without inserting zeolite membranes.

9.4. Reverse osmosis desalination unit

A reverse osmosis desalination unit with cross-flow configuration was assembled for testing produced water desalination. Each multichannel vessel with tubular zeolite membranes was tested individually for leakage and separation performance evaluation. The RO separation cells were assembled in parallel so that feed water flowed across the interior surface and the permeate could be collected together for an overall evaluation. A back pressure controller was deployed to maintain constant transmembrane pressure. A bypass loop was used to control the water flow rate on the surface of zeolite membranes. Both water flow rate and the transmembrane pressure were carefully monitored by digital flow meter and pressure sensor. The permeate was collected through a sample bottle connecting to the gas phase of a water flask. Purified water collected over a specific period of time was weighted for flux measurement and a small amount of purified water sample was diluted to appropriate concentrations (~0.0025 M) and analyzed by IC.

The demonstration unit was constructed in a trailer with dimension of 36 in. ×25 in. ×36 in. A Triplex pump with a flow rate of 3.78 L/min was used to drive the desalination process. Figure 68 shows the reverse osmosis zeolite membrane unit. The overall zeolite membrane area is ~0.3 m^2. The reverse osmosis demonstration gave an ion rejection of 96.9% and water flux of 2.23 $kg/m^2.h$ for 0.1M NaCl solution at an operating pressure of 3.5 MPa.

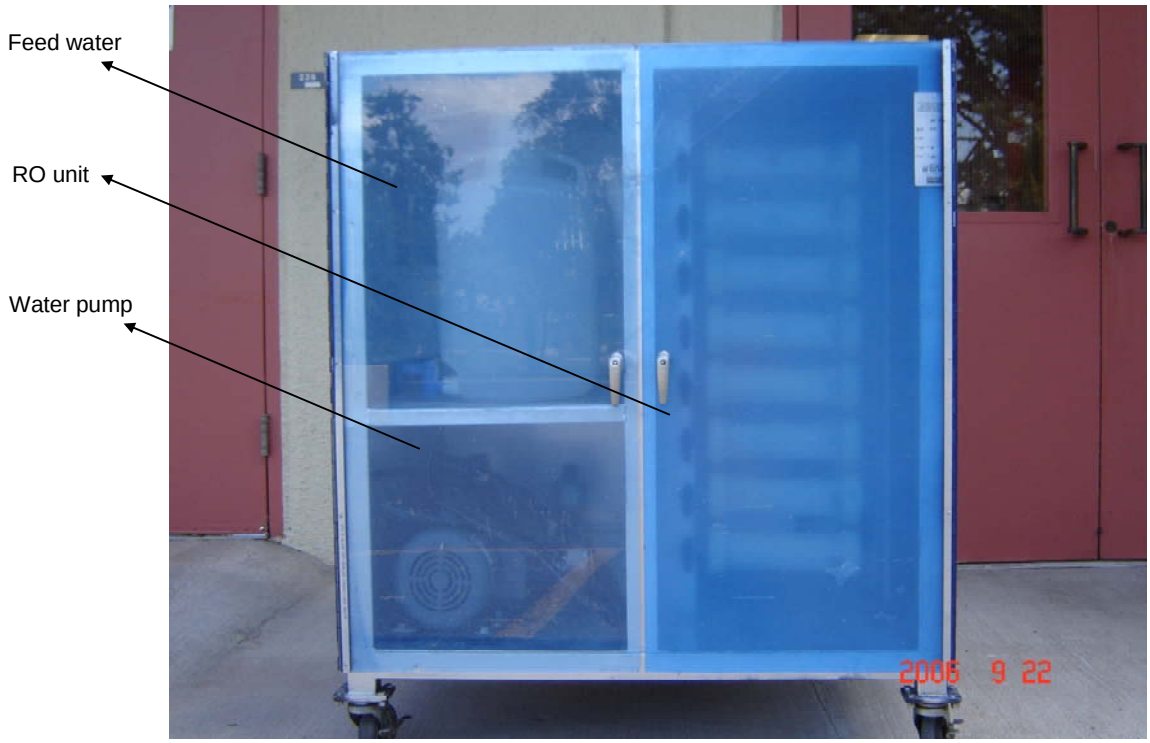

Fig. 68. Desalination demonstration of zeolite RO membranes.

10. LONG-TERM DESALINATION OF PRODUCED WATER BY ZEOLITE MEMBRANES

The purpose of long-term reverse osmosis desalination of produced water by zeolite membrane is to evaluate the membrane stability and potential fouling caused by dissolved organics and scale precipitation. An actual coalbed methane produced water from the San Juan Basin was used in the long-term permeation test. The desalination test was carried out at ambient temperature and transmembrane pressure of 500Psi. Both water flux and ion rejection were recorded every 12 hr. The foulants formed on the membrane surface were studied by scanning electron microscopy (SEM) with an EDS.

To unravel the mechanisms of organic fouling and chemical regeneration, fouling experiments were performed with organics that simulate organic species in produced water, such as fatty acid, phenol, and toluene solutions. The cleaning experiments for membrane regeneration after organic fouling were performed with diluted H_2O_2 solution under specified experimental conditions.

The water samples were diluted to desirable concentrations (~50 mg/L) and manually injected for cation and anion analysis. A sterilizing filter (0.2μm, Fisher) was deployed to remove any suspended particulates before the IC analysis. Concentrations of dissolved organics were represented by the TOC and analyzed by a TOC analyzer (Shimadzu, TOC-V). Particle size distribution of the produced water was analyzed by dynamic light scattering particle analyzer (Nanotrac NPA 150). Metal ions were analyzed by the flame atomic absorption (Varian Model 110). The surface properties of zeolite

membrane after oxidative treatment with H_2O_2 solution was studied by XPS together with FTIR (Kratos Axis Ultra spectrometer).

10.1. Chemistry of produced water

The CBM produced water used in this study has a total dissolved solid (TDS) of 2.17×10^4 mg/L and total organic carbon (TOC) of 329.2 mg/L. The original produced water contains large number of suspended particulates, floating oil droplets and dissolved components. A dynamic light scattering particle analyzer was deployed for study of particle size distribution of the produced water. Figure 69 gives the particle size distribution of the produced water. Most of fine coal powders in the CBM produced water have a particle size in the range of 1.6–6.5μm. Pretreatment by microfiltration or centrifuge is thus necessary to remove the coal fine particles before deploying the RO system for produced water purification.

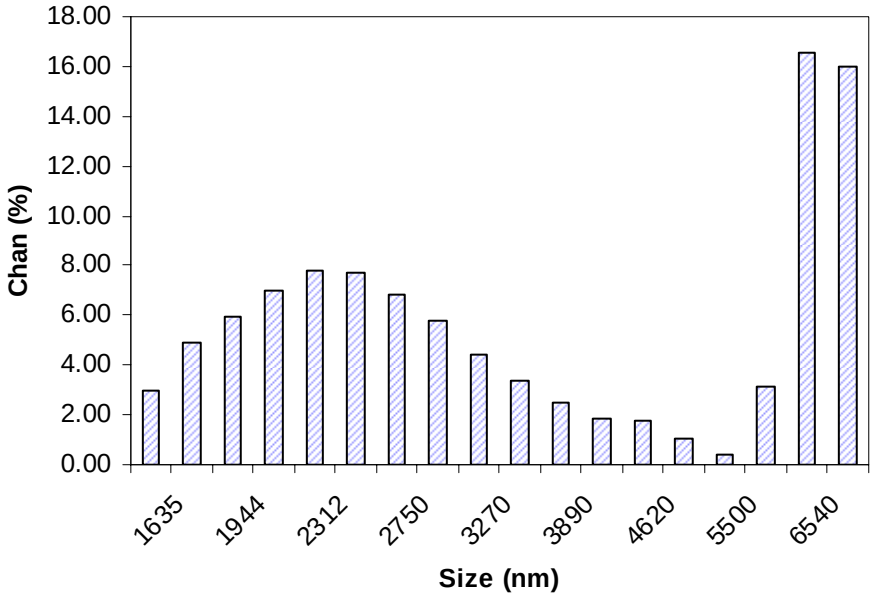

Fig. 69. Particle size distribution of suspensions in produced water.

10.2. Long-term separation of produced water by zeolite membranes

Table 11 gives the chemical composition of the produced water sample together with the ionic compositions in the permeate solution after permeating through the zeolite membrane.

Table 11. Ion removal from produced water by zeolite membranes

Composition	Feed concentration mg/L	Permeate concentration, mg/L	Ion rejction, %
Sodium (Na^+)	8853	1124	87.3%
Potassium (K^+)	25	Undetectable	~100%
Chloride (Cl^-)	15940	2143	86.6%
Magnesium (Mg^{2+})	97	Undetectable	~100%
Calcium (Ca^{2+})	88	Undetectable	~100%
Total organic carbon (TOC, mg/L)	329.2	58.4	82.3%

The zeolite membranes show higher ion separation efficiency on the bivalent ions (i.e., Ca^{2+} and Mg^{2+}) than those of the monovalent ions (i.e., Na^+ and Cl^-). This result is consistent to the individual ion permeation results [88]. Figure 70 shows the water flux of zeolite membranes as a function of elapsed permeating time. The water flux first increased from 1.40 kg/m^2.h to 3.55 kg/m^2.h, and then declined with elapsed operating time. After 35 days test, the water flux reached a relatively stable value at 1.0 kg/m^2.h. The ion rejection declined continuously from ~90% to 40% after operating for about two months as shown in Figs. 71 and 72. The initial increase in water flux was also observed for prepared NaCl solution which is attributed to the surface ionization [69]. As a zeolite membrane contacts with water, the zeolite adsorbs cations and anions from the aqueous solution by releasing protons or hydroxide ions, resulting in surface hydroxylation [89].

The formation of a group consisting of a large quantity of hydroxyls on a zeolite surface contacted with produced water results in considerable enhancement in surface hydrophilicity as well as water flux. Unfortunately, the adsorbed ion species also increase the ion concentration gradient across zeolite membranes, resulting in considerable increase in ion diffusion. As a result, ion separation efficiency will decrease. The subsequent severe declines in water flux and ion rejection are attributed to the organic fouling and scale deposition on the membrane surface.

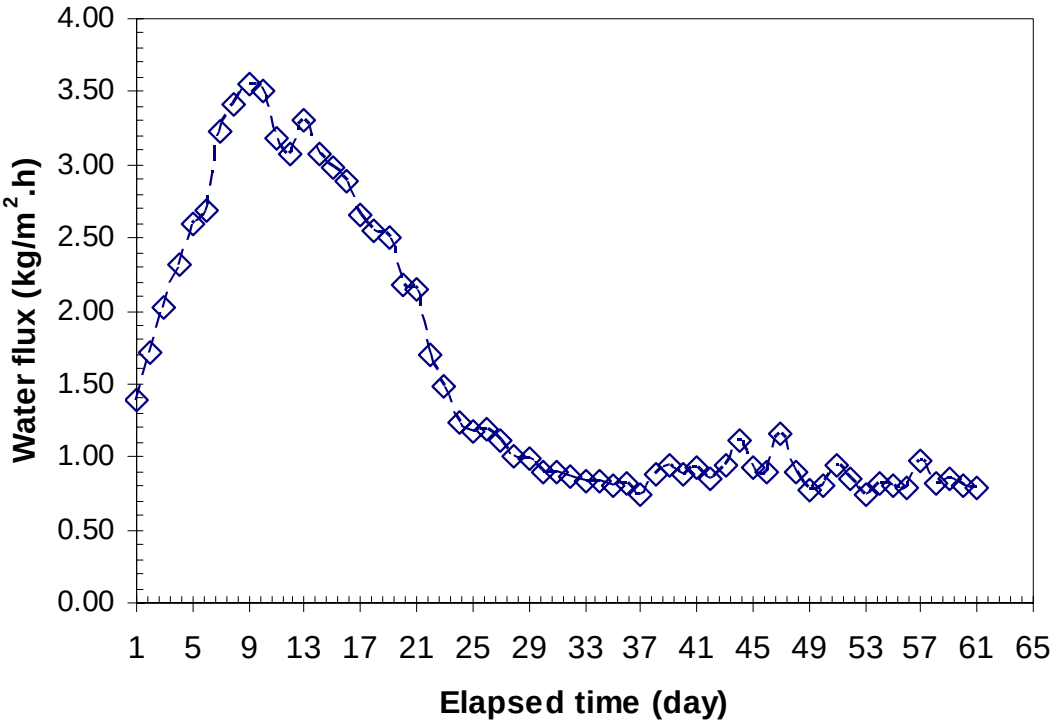

Fig. 70. Water flux variation as a function of elapsed RO permeation time.

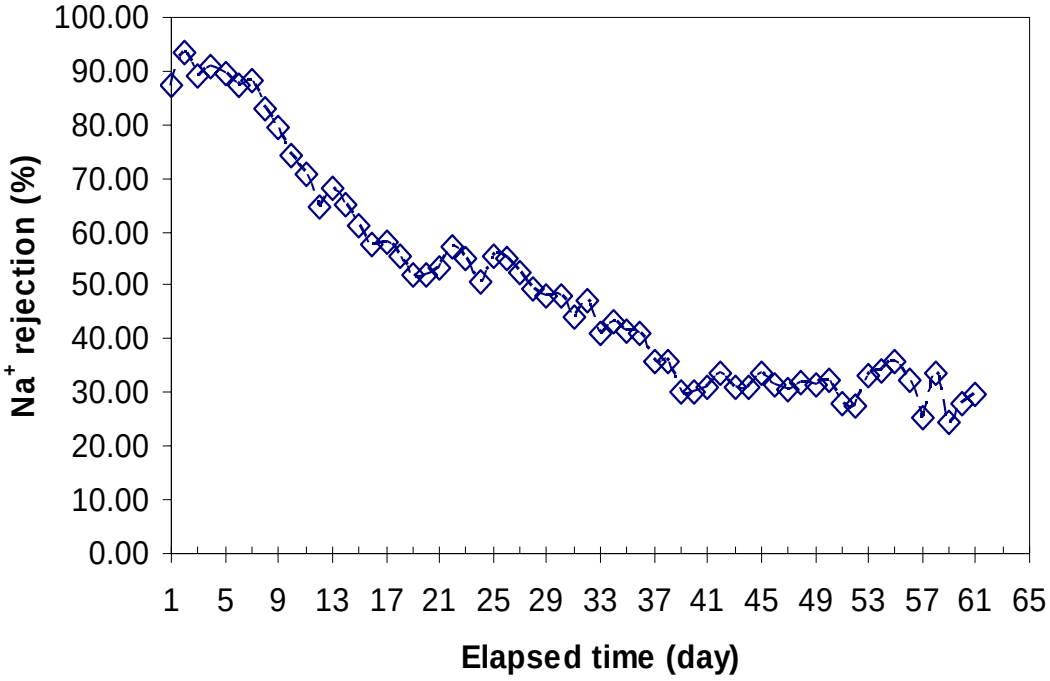

Fig. 71. Ion rejection (Na^+) as a function of elapsed RO permeation time.

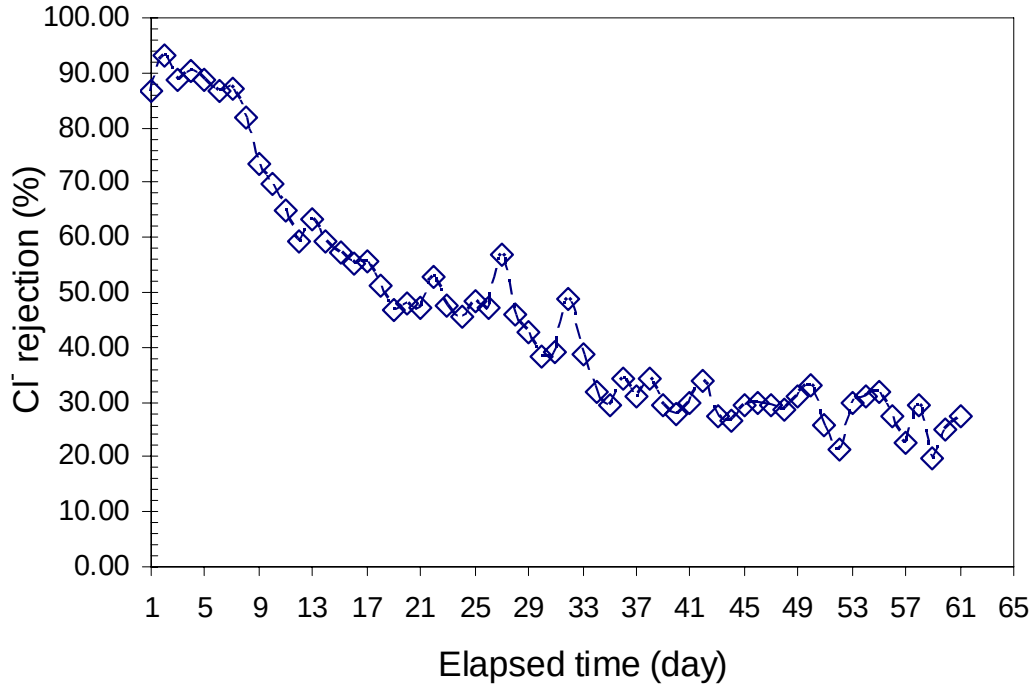

Fig. 72. Ion rejection (Cl^-) as a function of elapsed RO permeation time.

10.3. Mechanism of membrane fouling at loading with produced water

To further understand the influence of organic species in produced water on the water flux and scale deposition during long-term scale deposition, simulated produced water samples containing 0.10M NaCl and 200mg/L organic species were tested for reverse osmosis desalination. Figure 73 shows the water flux as a function of elapsed time for three solutions containing 0.1M NaCl and 200mg/L toluene, phenol and hexane, respectively. The presence of hexane and toluene in 0.1M NaCl solution results in a drastic decline in water flux while the presence of phenol causes a slight increase in water flux from 4.85 to 5.47 kg/m^2.h. As adsorption approaches equilibrium, the presence of organic species will decrease water flux due to their adsorption onto the membrane surface or into the interior cavity of the zeolite.

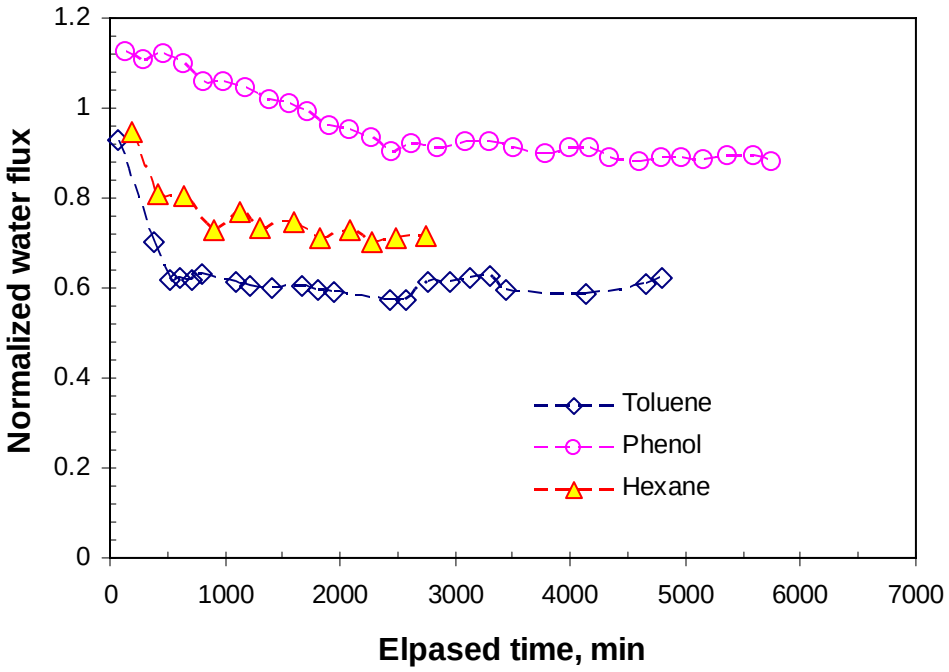

Fig. 73. Influence of organic species in produced water on membrane performance.

The zeolite membranes, after permeation with CBM produced water for two months, were washed thoroughly by using DI water and dried at 120°C for further SEM and EDS analysis. Figure 74 shows SEM images of the cross-section of a zeolite membrane after permeation with produced water for two months. The membrane with scale deposition has a thickness of 12–15μm. Further random surface searching and EDS analysis indicated that the chemical composition of the scale is mainly $CaCO_3$ and $SrCO_3$ crystals, as shown in Fig. 75. The fouled zeolite membrane was further cleaned with 0.1M HCl solution for 2 hr. The surface morphology and thickness of the zeolite membrane, after washing and drying, is shown in Figs. 76 and 77, respectively.

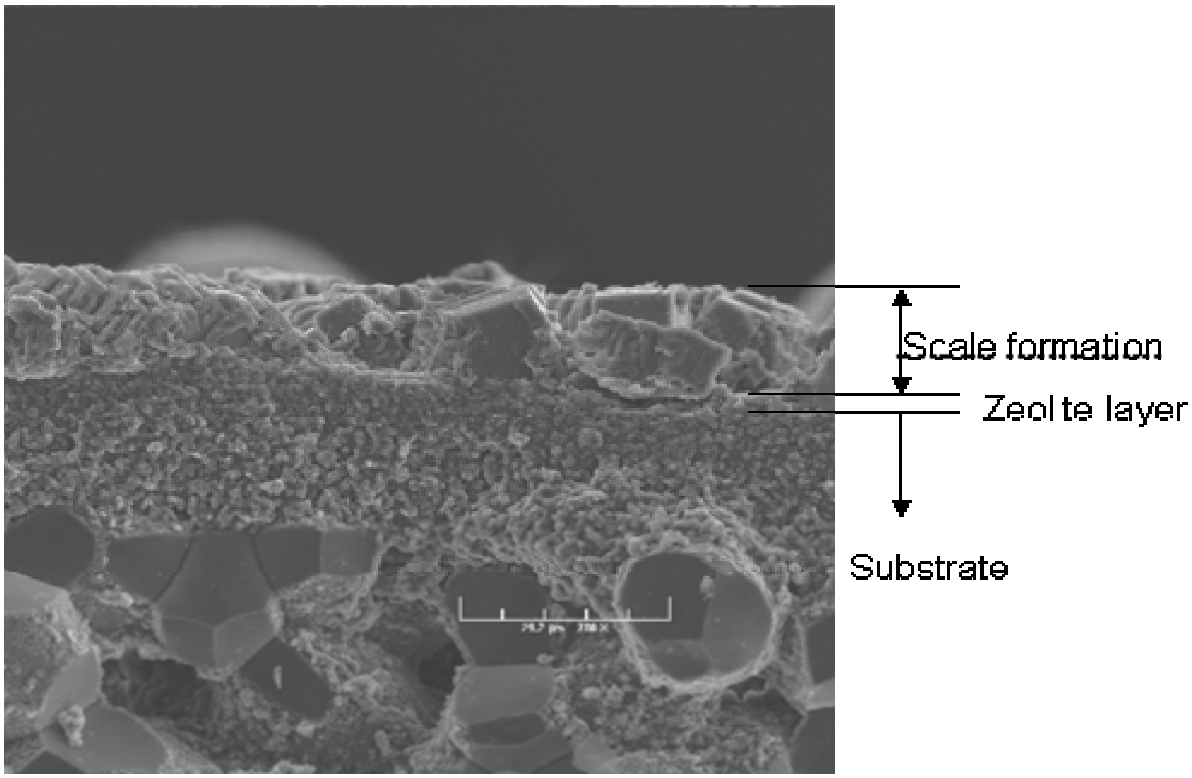

Fig. 74. Cross-section of fouled zeolite membrane after produced water desalination.

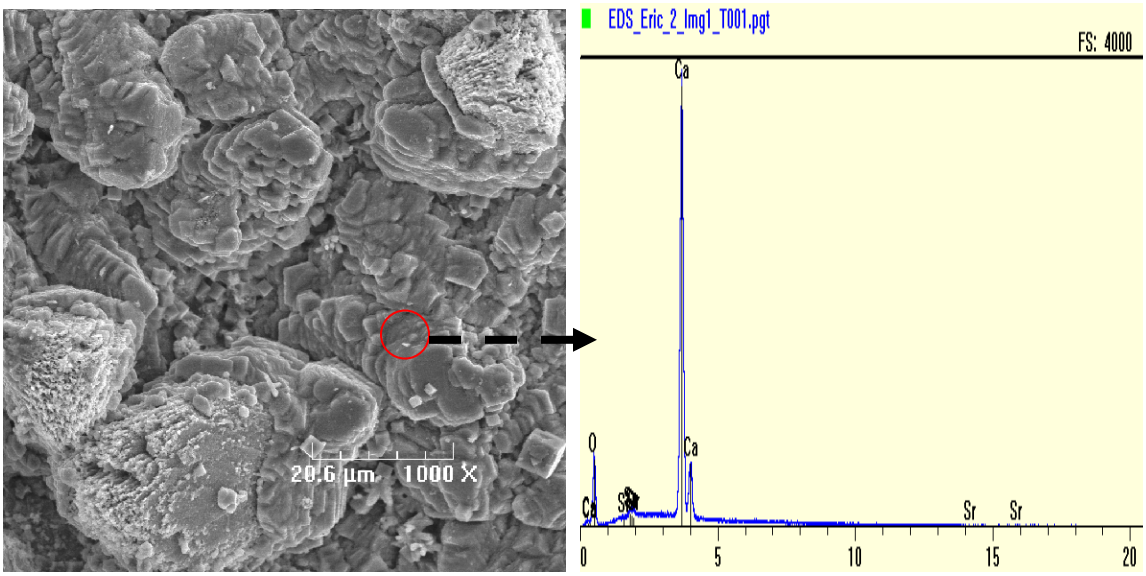

Fig. 75. Surface SEM image of zeolite membrane with foulant and EDS result for chemical composition.

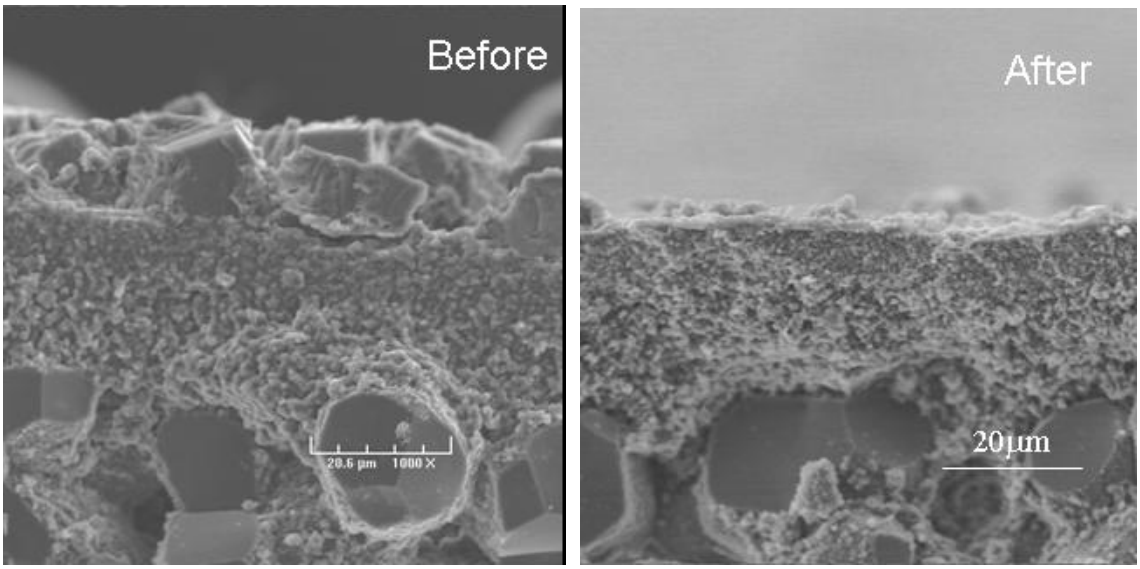

Fig. 76. SEM images (cross-section) of zeolite membrane before and after acid cleaning with 0.1M HCl solution.

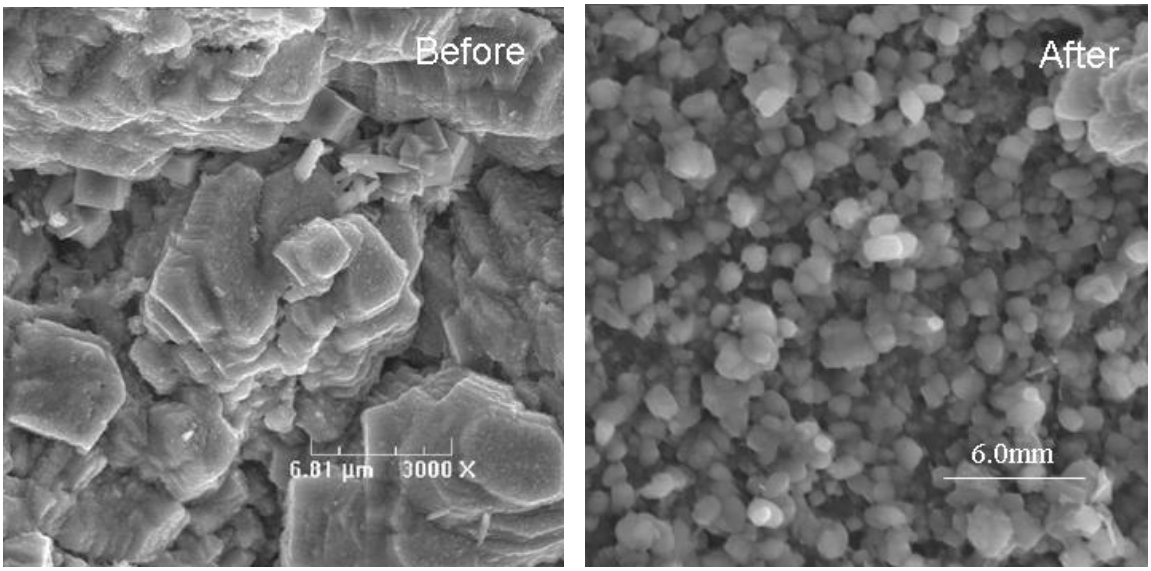

Fig. 77. SEM surface images of zeolite membrane before and after acid cleaning with 0.1M HCl solution.

10.4. Membrane regeneration by H_2O_2 solution

Severe scale precipitation and organic adsorption were observed on zeolite membrane surfaces after a long-term RO desalination test with CBM produced water. Periodic cleaning is suggested to maintain the membrane performance during long-term operation. The carbonate scale can be removed by acid solution but the adsorbed organic species is difficult to clean by regular solvent washing. In this work, an oxidative-regeneration for organic removal was studied for membrane regeneration after organic fouling. In the same permeation system, the feed tank was loaded with diluted H_2O_2 solution. Under transmembrane pressure of 100 psi, H_2O_2 solution was forced to permeate through zeolite membranes at very low flow rate. The oxidant in the micropore of zeolite membranes decomposed adsorbed organics.

Figure 78 shows the water flux and ion rejection before and after H_2O_2 oxidative regeneration. The zeolite membrane has a water flux of 4.86 kg/m^2.h and ion rejection of

97.9% for 0.1 M NaCl solution. The water flux gradually declined to 3.71 kg/m^2.h while the ion rejection slightly decreased to 97.2% when 200mg/L toluene was added into the 0.1M NaCl feed solution. The organic fouled membrane was followed by a treatment with 15% H_2O_2 solution at ambient temperature for 2 hr for organic decomposition. The water flux was recovered to 4.60 kg/m^2.h while the ion rejection decreased to 94.1%.

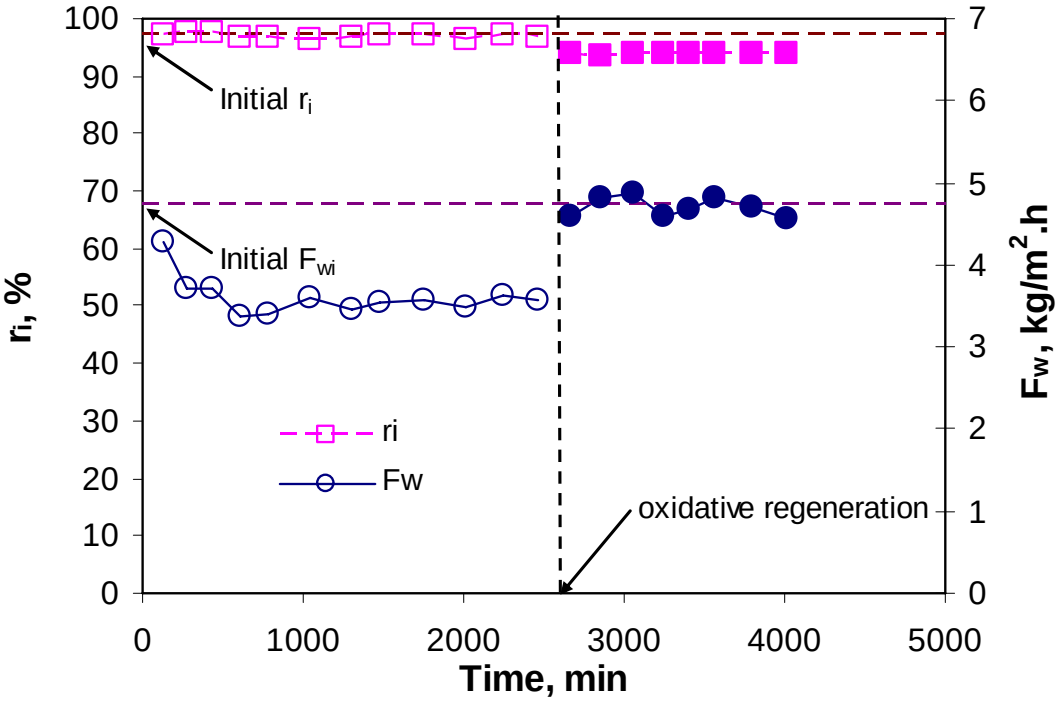

Fig. 78. Oxidative regeneration of zeolite membranes after organic fouling.

XPS measurements were performed on a Kratos Axis Ultra spectrometer using an AlK α 1486 eV monochromatic X-ray source. An electron flood gun for charge neutralization and hemispherical analyzer with an eight-multichannel photomultiplier detector was employed for analysis. Three large areas (300μm × 700 μm) per sample ere analyzed for (1) low resolution survey spectra at 80 eV PE, and (2) high resolution O 1s, Na 1s, C 1s and Si 2p spectra at 20 eV. Figures 79 and 80 show the low resolution survey

spectra and high resolution C1s respectively. Two types of O were detected for – SiO_2 and C_xO_y species. The C=O species may also contribute to 532.4 eV, making O not suitable for concluding on chemical composition. Three types of carbons were detected , C-C, C-O and C=O (COOH). Significant increase in C-C and C=O for the treated sample suggested increase in –COOH group on the zeolite surface after oxidative regeneration. The enhancement in surface hydrophilicity due to the presence of large amounts of −COOH group might be the reason for enhanced water flux.

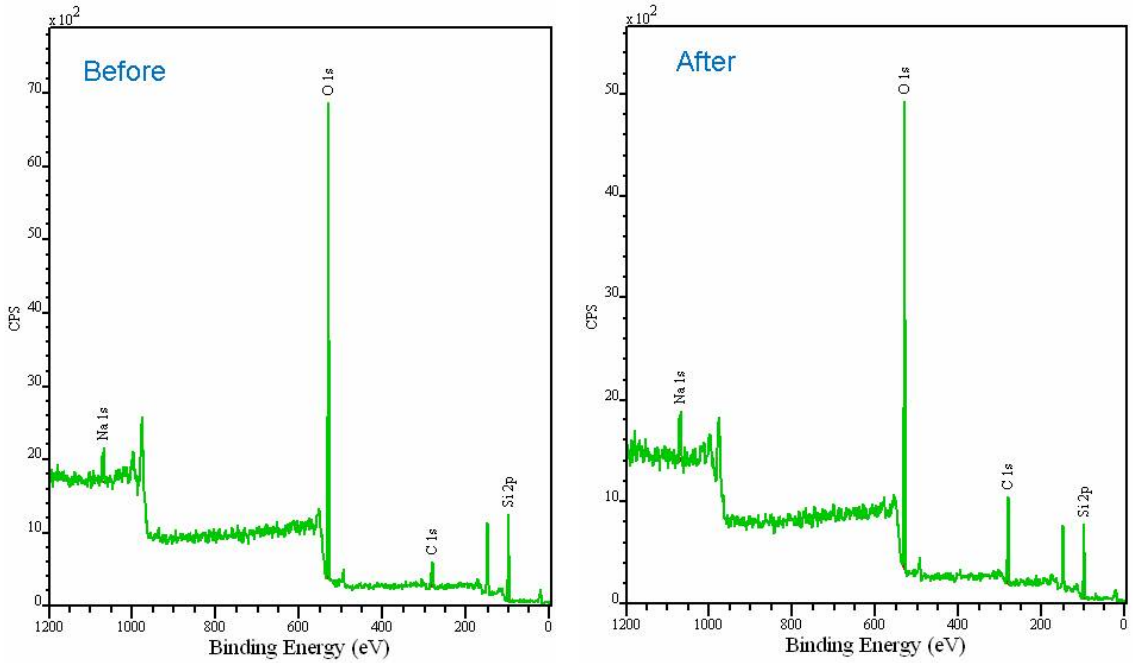

Fig. 79. Low resolution survey spectra of zeolite before and after H_2O_2 oxidative treatment.

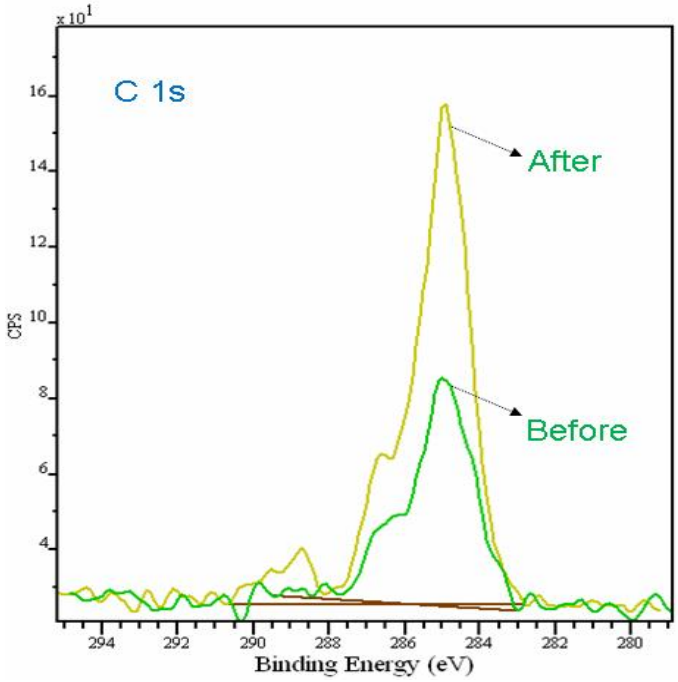

Fig. 80. High resolution C 1s spectra for zeolite membrane before and after oxidative H_2O_2 oxidation.

Despite the rigorous efforts to reduce membrane fouling, such as surface modification and pretreatment, fouling is essentially inevitable, particularly for produced water containing large amounts of fine coal powder and dissolved organics. In addition, CBM produced water contains high concentrations of bicarbonate ions that promote scale deposition on membrane surface during a RO process. Thus, development of effective chemical cleaning, i.e., in-situ oxdative regeneration, is a necessary process to ensure sustainable operation for the long-term CBM produced water desalination.

11. ENGINEERING ASPECT AND ECONOMICS

Currently, only a few types of zeolite membranes have been commercialized or demonstrated for industry application. A typical example of the commercial application of zeolite membranes includes alcohol dehydration by LTA zeolite membranes and CO_2 separation by DDR-type zeolite membranes [90]. Recent research efforts focus on MFI-type and FAU-type zeolite membranes, which have larger pore sizes at 0.56nm and 0.74nm, respectively, and enhanced chemical stability. However, the commercialization of these zeolite membranes have not been reported. Caro and coworkers [90] summarized the engineering difficulties for upscaling the fabrication of zeolite membranes, from the laboratory to commercial application.

First, zeolite membranes usually have an asymmetric cross-section with a multilayer structure for the purpose of reducing mass flow resistance. Unfortunately, the membranes with layered structure have to be fired at each step of synthesis, considerably increasing the production costs.

Secondly, at least 70% of the zeolite membrane price comes from the fabrication of ceramic support. Thus, tremendous efforts are being devoted to searching for cheaper, automated production of membrane supports that can be used as support for coating thin zeolite layers. Defect-free zeolite membranes have been successfully synthesized on porous supports including α-alumina and stainless steel.

Thirdly, module design needs to meet the requirement of application under harsh conditions. Advantages of inorganic membranes include high stability at elevated temperatures and in the presence of strong organic solvents. The module and seal should

be applicable for the specific environment and in-situ oxidative regeneration. A solution provided by the auther is potting the membranes into a stainless steel module by a ceramic binder. But, the seeding and zeolite layer fabrication must be laid down after completion of the housing.

The major disadvantage of the zeolite membranes is that the zeolite membranes are about 10–50 times more expensive than the equivalent polymeric membranes. But, the unique application of this membrane in produced water purification might be able to overcome the disadvantages. Specifically, the zeolite membranes have advantages including tolerance to dissolved organics in produced water, high mechanical strength, and easy regeneration by in-situ oxidation. Tactics that were deployed to reduce the membrane cost and upscale the fabrication process include:

(1) Selecting appropriate substrates for high-quality zeolite fabrication.

Three-type of inorganic supports were investigated for MFI-type zeolite fabrication: α-alumina, stainless steel, and Zr-coated stainless steel. Figure 81 shows these substrates that we studied in our laboratory.

(a) Stainless steel (Mott Metallurgical Corporation, Farmington).

(b) α-alumina (Pall Process Filtration Co.)

(c) Zr-coated stainless steel (Pall Process Filtration Co.)

Fig. 81. Inorganic substrates tested for zeolite membrane fabrication.

From the perspective of ion rejection, water flux, and membrane reproducibility, the sequence of membrane quality on different substrate are: α-alumina>stainless steel>Zr-coated stainless steel. In addition, the zeolite layer formed on stainless steel is not stable during long-term permeation testing, which was explained by corrosion of stainless steel in high concentration produced water.

(2) New zeolite coating process for defect-free zeolite membrane synthesis.

Fabrication of thin and defect-free thin zeolite layer on porous support is the primary objective of a membrane synthesis. High temperature sintering (i.e., 450°C) for template removal and low repeatability of membranes are the major cost of membrane synthesis. In this work, high quality zeolite membranes were synthesized by a two-step crystallization process. First, porous substrate was dipped into a synthesis solution containing high concentration template (TPAOH solution) for seeding layer formation. A thin zeolite layer (~1.0 μm) was crystallized on porous support. Permeation tests have indicated that zeolite layer formed by this process shows a high density of microdefects and has very low ion rejection efficiency. Secondly, the zeolite layer formed by in-situ crystallization was sintered at 450°C for template removal. Finally, defect-free zeolite membranes were formed by treating the seeded substrates in a template-free solution at hydrothermal condition: zeolite crystals grow further and form a dense layer on porous support. Figure 82 shows the fabrication process of zeolite membranes. With this process, over 90% zeolite membranes have high ion rejection efficiency (>95%) and high water flux (>1.0 $kg/m^2.h$).

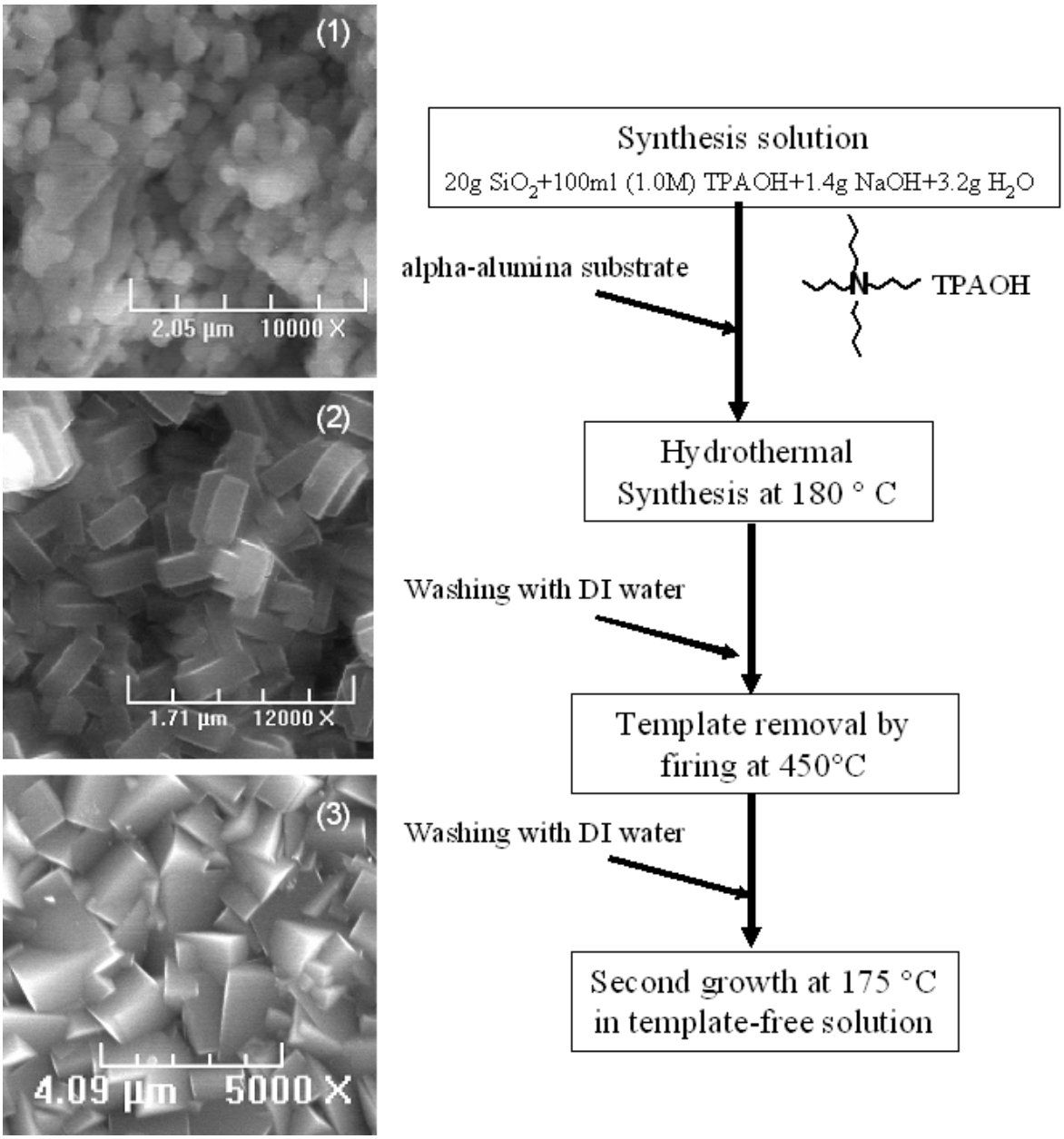

Fig. 82. Membrane synthesis process by two-step crystallization.

(3) Design of module compatible with the ceramic membranes and produced water characteristics.

Advantages of the inorganic membranes compared to polymeric membranes are the tolerance in organic solution and in-situ oxidative regeneration. Corrosion resistance

for long-term application in produced water environment also needs to be considered. To retain these advantages, the module of the 0.3 m^2 membrane area is equipped with tubular zeolite membranes in a cross-flow configuration.

The zeolite RO system, which employs zeolite membranes instead of conventional polymeric membranes, has a layout similar to that used in other RO processes. The produced water will be pretreated first by filtration or centrifuging for particulate removal. A high-pressure pump will then be employed to drive water molecules to pass through a semipermeable membrane and produce clean water. Several factors including quantity of produced water and plant capacity are believed to be critical for unit production costs. Major elements of economic calculation include: (1) direct capital cost; (2) indirect capital cost; and (3) annual operating cost.

The direct capital cost includes purchase of equipment, land use, building constructions, and membrane unit. The indirect cost includes insurance, construction overhead and owner's costs. The operating costs include electricity, labor, membrane replacement, maintenance and amortization charges. Figure 83 gives the major elements of RO cost evaluation [91].

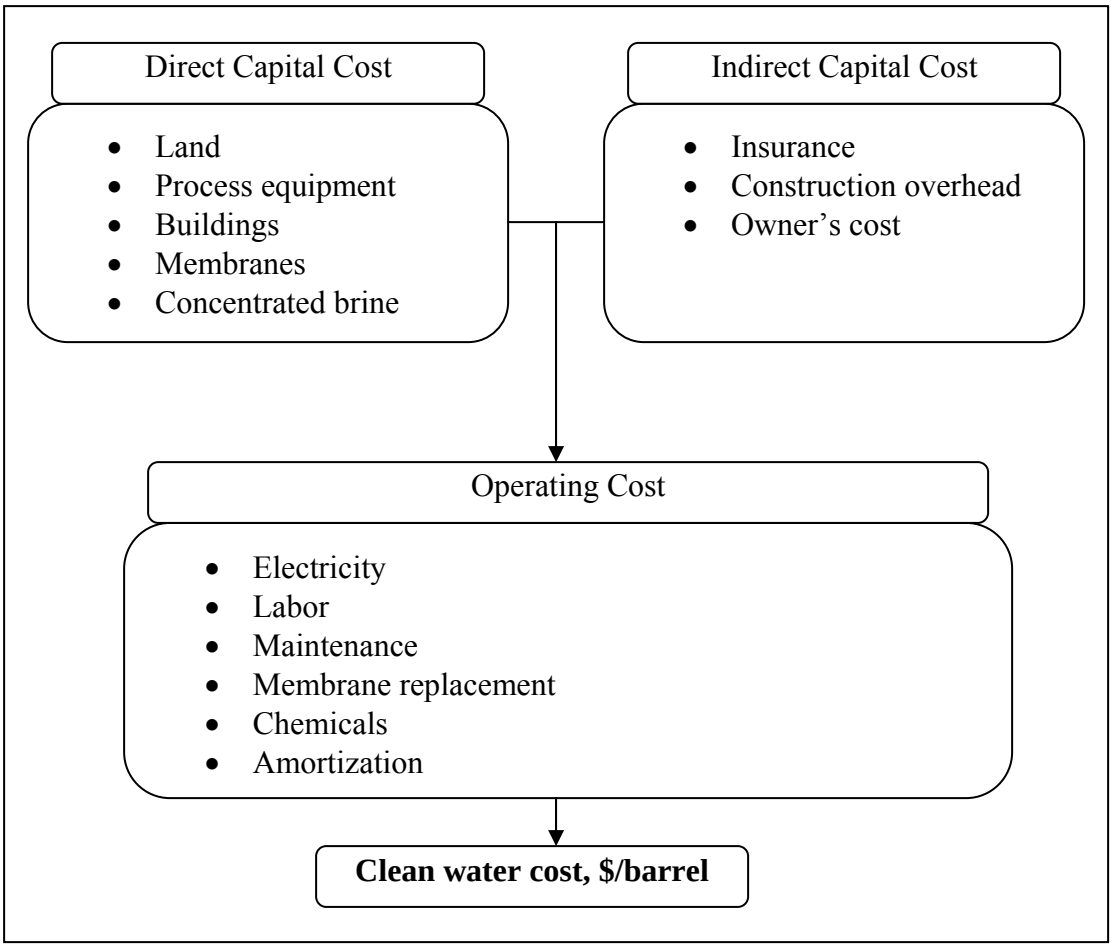

Fig. 83. Elements used for cost analysis of RO desalination.

For a RO unit with desalination capacity of 1,000 m^3/d, the capital cost and operating cost of the conventional RO process is listed in Table 12 [92].

Table 12. Overall cost of a RO unit with capacity of 1,000 m^3/d

Capital cost, $	Unit capital cost, $/$m^3$/d	Energy cost, $/Yr	Unit energy cost, $/$m^3$	Unit chemical cost, $/$m^3$	Water cost, $/$m^3$
924,000	924	1,710,000	0.52	0.11	1.51

The above cost calculation is based on seawater desalination, in which the membrane replacement rate varies between 5%–20% per year. Produced water contains

large quantities of waste such as suspended solids, iron, and organic and inorganic contaminants. The frequency of membrane replacement will be much higher than it is for the desalination of seawater. The polymeric RO membranes tested for produced water desalination show considerable decline within 3 months due to serious fouling, suggesting a short lifetime and high replacement rate [93]. The zeolite membrane has been developed for attacking organic fouling in produced water, due to its extremely stable chemical and mechanical properties. With a water flux of 5 $kg/m^2.h$, zeolite membranes with a surface area of 8332 m^2 are needed to generate a capacity of 1000 m^3/d. Table 13 compares the membrane cost and replacement rate of polymer membranes and the zeolite membranes developed in this research.

Table 13. Membrane cost and replacement rate

	Membrane flux, $kg/m^2.h$	Membrane surface area, m^2	Membrane cost	Membrane life time	Membrane replacement, $/yr
Polymer membrane	30	1388	20,000	3 months	$267,300 at 20% per year
Zeolite membrane	5–10	8332	916,520	5 years	$429,540 at 20% per year

Note: zeolite membrane price is estimated as $\$110/m^2$.

At the assumption of: (1) same land, equipment and building cost, (2) same insurance, labor and maintenance, the variation of unit water cost when applied to produced water is summarized in Table 14. Periodically cleaning the zeolite membrane by H_2O_2 oxidant (once every month) is suggested for recovering the water flux.

Table 14. Influence of membrane material and replacement on the unit water cost

	Membrane cost	Membrane replacement, $/yr	Chemical cost, $/m^3	Water from produced water, $/m^3
Polymer membrane	20,000	5,346,000	1.2	16.62
Zeolite membrane	916,520	429,540	1.5	6.01

In conclusion, a zeolite membrane with a water flux of 5.0 kg/m^2.h and operating lifetime of 5 years can clean produced water at a cost of ~$6/m^3. The major operating cost comes from membrane installation, replacement and chemicals used for foulant removal. It is expected that either improvement of membrane performance (i.e. enhanced water flux) or decline in membrane cost will result in a considerable decline in the cost of clean water produced.

12. CONCLUSION AND RECOMMENDATIONS

The main objective of this research is to demonstrate the desalination capacity of zeolite membranes and to evaluate technical and economic potential of zeolite membranes for application in produced water desalination. For achieving the research objectives, a module of ~0.3 m^2 membrane area with tubular zeolite membranes has been produced. The zeolite membranes show excellent chemical and mechanical stabilities where high operation pressure (>10MPa) and strong turbulent flow can be applied for breaking the organic fouling and concentration polarization. Under the preferable operating conditions, microporous structure of zeolite membranes were investigated by different techniques including cross-flow permeation, BET, and XPS of FTIR.

1. The MFI zeolite membranes are capable of removing ions from aqueous solutions via reverse osmosis. In the reverse osmosis process, both ion and water fluxes can be enhanced by increasing the temperature or the transmembrane pressure (ΔP). However, changing temperature and pressure have different impacts on the ion rejection rate. Raising temperature has a greater influence on the ion permeation than on the water permeation, resulting in a decline of the ion rejection. On the contrary, increasing the transmembrane pressure can enhance both the water flux and ion rejection rates because the ion flux is much less affected by pressure compared to the water flux. Operating at elevated temperatures and high hydraulic pressures is desirable for enhancing the separation efficiency.
2. Ion separation performance of zeolite membranes can be improved by incorporating Al^{3+} ions into zeolite framework. The enhancement in RO

performance of the ZSM-5 membranes is explained by strong water affinity on the zeolite surface and a high surface charge caused by ion substitution.

3. A module of 0.3m^2 zeolite membrane area is equipped with 80 tubular zeolite membranes produced in this research. The zeolite membranes have >95% ion rejection and large variation in water flux from 0.6 to 10.0 kg/m^2.h. These findings suggest that for RO, zeolite membranes, which possess excellent thermal and mechanical stabilities, have the potential for use in severe environments. However, the zeolite membranes are not competitive with polymer membranes in seawater desalination due to the high cost of membrane substrate. It is suggested that in specific conditions where polymeric membranes fail, i.e., produced water, strong solvents and radioactive environments, zeolite membranes could be an alternative option for water purification.
4. A post-synthesis modification method by using Al^{3+}-oligomers was developed for repairing the undesirable nano-scale intercrystalline pores. The undesirable intercrystalline pores can be effectively reduced by means of depositing metal ion oligomers with considerable enhancement in ion rejection but less influence on water flux. This new method of zeolite membrane modification is particularly useful for enhancing the efficiency of ion separation from aqueous solutions because the modification does not require high-temperature operation and may be carried out online during the RO operation.
5. A gradual decline in both water flux and ion rejection was observed during long-term operation in produced water desalination, which was attributed to scale deposition and organic fouling. An in-situ oxidative regeneration experiment was

carried out for organic decomposition. Zeolite membranes treated by 15% H_2O_2 show >90% recovery in both water flux and ion rejection. Pretreatment for divalent ion removal and periodic regeneration by strong oxidant treatment are suggested for long-term produced water purification.

In summary, the research conducted in this project has resulted in eight papers published in peer-reviewed journals, a pending patent, and six conference preceedings.

REFERENCES

[1] Veil, J.A., M.G. Puder, D. Elcock, P.J. Redweik, A White Paper Describing Produced Water from Production of Crude Oil, Natural Gas, and Coal Bed Methane, DOE Report, W-31-109-Eng-38, National Energy Technology Laboratory, (2004).

[2] Tao, F.T., S. Curtice, R.D. Hobbs, J.L. Sides, J.D. Wieser, C.A. Dyke, D. Tuohey, and P.F. Pilger, *Oil Gas J.* 91 (1993), 88-91.

[3] Van Veen, H.M., Y.C. Van Delft, C.W.R. Engelen, and P.P.A.C. Pex, *Sep. Purif. Technol.* 22-3 (2001), 361-366.

[4] Visvanathan, C., N. Boonthanon, A. Sathasivan, and V. Jegatheesan, *Desalination* 153 (2003), 133-140.

[5] Kumakiri, I., T. Yamaguchi, and S. Nakao, *J. Chem. Eng. Jpn.* 33 (2000), 333-336.

[6] Li, L.X., J.H. Dong, T.M. Nenoff, and R. Lee, *Desalination* 170 (2004), 309-316.

[7] Kiriukhin, M.Y., and K.D. Collins, *Biophys. Chem.* 99 (2002), 155-168.

[8] Chong, S.H., and F. Hirata, *J. Chem. Phys*. 111 (1999), 3654-3667.

[9] Chowdhuri, S., and A. Chandra, *J. Chem. Phys.* 118 (2003), 9719-9725.

[10] LyndenBell, R.M., and J.C. Rasaiah, *J. Chem. Phys.* 105 (1996), 9266-9280.

[11] Hubbard, J., and L. Onsager, *J. Chem. Phys.* 67 (1977), 4850-4857.

[12] Bluhm, E.A., E. Bauer, R.M. Chamberlin, K.D. Abney, J.S. Young, and G.D. Jarvinen, *Langmuir* 15 (1999)，8668–8672.

[13] Hartnig, C., W. Witschel, and E. Spohr, *Ber. Bunsen-Ges. Phys. Chem. Chem. Phys.* 102 (1998), 1689-1692.

[14] Allen, T.W., S. Kuyucak, and S.H. Chung, *J. Chem. Phys.* 111 (1999), 7985–7999.

[15] Holt, J.K., H.G. Park, Y.M. Wang, M. Stadermann, A.B. Artyukhin, C.P. Grigoropoulos, A. Noy, and O. Bakajin, *Science* 312 (2006), 1034-1037.

[16] Li, L.X., Liu, N., McPherson, B., and Lee, R. *Desalination*. In press, 2008.

[17] Dong, J.H., Y.S. Lin, M.Z.C. Hu, R.A. Peascoe, and E.A. Payzant, *Microporous Mesoporous Mat.* 34 (2000), 241-253.

[18] Nikolakis, V., M. Tsapatsis, and D.G. Vlachos, *Langmuir* 19 (2003), 4619-4626.

[19] Chau, J.L.H., C. Tellez, K.L. Yeung, and K.C. Ho, *J. Membr. Sci.* 164 (2000) 257–275.

[20] Majumder, M., N. Chopra, R. Andrews, and B.J. Hinds, *Nature* 438 (2005), 44-44.

[21] Olson, D.H., W.O. Haag, and W.S. Borghard, *Microporous Mesoporous Mat.* 35-36 (2000), 435-446.

[22] Coronas, J., J.L. Falconer, and R.D. Noble, *AICHE J.* 43 (1997), 1797-1812.

[23] Noack, M., P. Kolsch, J. Caro, M. Schneider, P. Toussaint, and I. Sieber, *Microporous Mesoporous Mat.* 35-36 (2000), 253-265.

[24] Jareman, F., J. Hedlund, and J. Sterte, *Sep. Purif. Technol.* 32 (2003), 159-163.

[25] Auerbach, S.M., K.A. Carrado, and P.K. Dutta, Handbook of Zeolite Science and Technology, Marcel Dekker, Inc. New York, 2003**.**

[26] Van de Graaf, J.M., E. van der Bijl, A. Stol, F. Kapteijn, and J.A. Moulijn, *Ind. Eng. Chem. Res*. 37 (1998), 4071-4083.

[27] Hedlund, J., J. Sterte, M. Anthonis, A.J. Bons, B. Carstensen, N. Corcoran, D. Cox, H. Deckman, W. De Gijnst, P.P. de Moor, F. Lai, J. McHenry, W. Mortier, and J. Reinoso, *Microporous Mesoporous Mat.* 52 (2002), 179-189.

[28] Uguina, M.A., A. Delucas, F. Ruiz, and D.P. Serrano, *Ind. Eng. Chem. Res*. 34 (1995), 451-456.

[29] Lai, R., and G.R. Gavalas, *Microporous Mesoporous Mat.* 38 (2000), 239-245.

[30] Lai, Z.P., G. Bonilla, I. Diaz, J.G. Nery, K. Sujaoti, M.A. Amat, E. Kokkoli, O. Terasaki, R.W. Thompson, M. Tsapatsis, and D.G. Vlachos, *Science* 300 (2003), 456-460.

[31] McDonnell, A.M.P., D. Beving, A.J. Wang, W. Chen, and Y.S. Yan, *Adv. Funct. Mater.* 15 (*2005),* 336-340.

[32] Oonkhanond, B., and M.E. Mullins, *J. Colloid Interface Sci.* 284 (2005), 210-215.

[33] Dong, J.H., K. Wegner, and Y.S. Lin, *J. Membr. Sci.* 148 (1998), 233-241.

[34] Huheey, J. E., E.A. Keiter, and R.L. Keiter, Inorganic chemistry: Principles of Structure and Reactivity. HarperCollins College Publisher, New York (1993).

[35] Bandini, S., and D. Vezzani, *Chem. Eng. Sci.* 58 (2003), 3303-3326.

[36] Williams, M.E., J.A. Hestekin, C.N. Smothers, and D. Bhattacharyya, *Ind. Eng. Chem. Res*. 38 (1999), 3683-3695.

[37] Zhou, W.W., and L.F. Song, *Environ. Sci. Technol*. 39 (2005), 3382-3387.

[38] Bowen, T.C., R.D. Noble, and J.L. Falconer, *J. Membr. Sci*. 245 (2004), 1-33.

[39] Mon, K.K., J.K. Percus, *J. Chem. Phys*. 117 (2002), 2289-2292.

[40] Bowen, T.C., J.C. Wyss, R.D. Noble, and J.L. Falconer, *Ind. Eng. Chem. Res.* 43 (2004), 2598-2601.

[41] Nomura, M., T. Yamaguchi, and S. Nakao, *J. Membr. Sci*. 187 (2001), 203-212.

[42] Gu, X.H., J.H. Dong, and T.M. Nenoff, *Ind. Eng. Chem. Res.* 44 (2005), 937-944.

[43] Buelna, G., and Y.S. Lin, *Microporous Mesoporous Mat.* 30 (1999), 359-369.

[44] Zhao, D.Y., Q.S. Huo, J.L. Feng, B.F. Chmelka, and G.D. Stucky, *J. Am. Chem. Soc.* 120 (1998), 6024-6036.

[45] Brunauer, S., L.S. Deming, W.E. Deming and E. Teller, *J. AM. Chem. Soc.* 62 (1940), 1723-1732.

[46] Storck, S., H. Bretinger, and W.F. Maier, *Appl. Catal. A-Gen.* 174 (1998), 137-146.

[47] Horvath, G., and K. Kawazoe, *J. Chem. Eng. Jpn.* 16 (1983), 470-475.

[48] Saito, A., H.C. Foley, *Microporous Mater.* 3 (1995), 531-542.

[49] Groen, J.C., L.A.A. Peffer, and J. Perez-Ramirez, *Microporous Mesoporous Mat.* 60 (2003), 1-17.

[50] Tsuru, T., *Sep. Purif. Methods* 30 (2001), 191-220.

[51] Zhao, D.Y., J.L. Feng, Q.S. Huo, N. Melosh, G.H. Fredrickson, B.F. Chmelka, and G.D. Stucky, *Science* 279 (1998), 548-552.

[52] Caro, J., M. Noack, P. Kolsch, and R. Schafer, *Microporous Mesoporous Mat.* 38 (2000), 3-24.

[53] Wang, Z.B., and Y.S. Yan, *Chem. Mat.* 13 (2001), 1101-1107.

[54] Li, S., X. Wang, D. Beving, Z.W. Chen, and Y.S. Yan, *J. Am. Chem. Soc*. 126 (2004), 4122-4123.

[55] Hsu, P.H., *Clays Clay Min*., 36 (1988) 25-30.

[56] Pinnavaia, T.J., *Science* 220 (1983), 365-371.

[57] Ishiguro, M., T. Matsuura, and C. Detellier, *J. Membr. Sci.* 107 (1995), 87-92.

[58] Lin, J., and S. Murad, *Mol. Phys*. 99 (2001), 1175-1181.

[59] Jamnik, B., and V. Vlachy, *J. Am. Chem. Soc*. 115 (1993), 660–666.

[60] Pavlov, M., P.E.M. Siegbahn, and M. Sandstrom, *J. Phys. Chem*. *A* 102 (1998), 219-228.

[61] Biswas, R., and B. Bagchi, *J. Chem. Phys*. 106 (1997), 5587-5598.

[62] Yang, K.L., S. Yiacoumi, and C. Tsouris, *J. Chem. Phys*. 117 (2002), 8499-8507.

[63] Lee, S.H., and J.C. Rasaiah, *J. Phys. Chem.* 100 **(**1996), 1420-1425.

[64] Bak, I., J. Hutter, and G. Palinkas, *J. Chem. Phys*. 117 (2002), 9838-9843.

[65] King, A.J., G.C. Lillie, V.W.Y. Cheung, S.M. Holmes, and R.A.W. Dryfe, *Analyst* 129 (2004), 157-160.

[66] Li, L.X., Molecular Sieve Zeolite Membrane and Micro/mesoporous Clay Membranes for Liquid and Gas Separation. Ph.D Dissertation, New Mexico Institute of Mining and Technology, 2005.

[67] Ishiguro, M., T. Matsuura, and C. Detellier, *Sep. Sci. Technol.* 31 (1996), 545-556.

[68] Chowdhuri, S., and A. Chandra, *J. Chem. Phys*. 115 (2001), 3732-3741.

[69] Li, L.X., J.H. Dong, and T.M. Nenoff, *Sep. Purif. Technol.* 53 (2007), 42-48.

[70] Impey, R.W., P.A. Madden, and I.R. McDonald, *J. Phys. Chem*. 87 (1983), 5071-5083.

[71] Neilson, G.W., and J.E. Enderby, *Adv. Inorg. Chem*. 34 (1989), 195-218.

[72] Helm, L., and A.E. Merbach, *Coord. Chem. Rev.* 187 (1999), 151-181.

[73] Scott M. Auerbach, Kathleen A. Carrado and Prabir K. Dutta, Handbook of Zeolite Science and Technology, Marcel Dekker, Inc., New York, 2003.

[74] Hansen, B.R., and S.R.H. Davies, *Chem. Eng. Res. Des.* 72 (1994), 176-188.

[75] Wijmans, J.G., and R.W. Baker, *J. Membr. Sci*. 107 (1995), 1-21.

[76] Labbez, C., P. Fievet, A. Szymczyk, A. Vidonne, A. Foissy, and J. Pagetti, *Sep. Purif. Technol.* 30 (2003) 47–55.

[77] Huisman, I.H., G. Tragardh, C. Tragardh, and A. Pihlajamaki, *J. Membr. Sci.* 147 (1998) 187–194.

[78] Andersen, O.S., and S.W. Feldberg, *J. Phys. Chem*. 100 (1996), 4622-4629.

[79] Murad, S., K. Oder, and J. Lin, *Mol. Phys.* 95 (1998), 401-408.

[80] Schreier, M., and J.R. Regalbuto, *J. Catal*. 225 (2004), 190-202.

[81] Giaya, A., and R.W. Thompson, *J. Chem. Phys.* 117 (2002), 3464-3475.

[82] Rempe, S.B., L.R. Pratt, G. Hummer, J.D. Kress, R.L. Martin, and A. Redondo, *J. Am. Chem. Soc*. 122 (2000), 966-967.

[83] Santos, S.M., and M.R. Wiesner, *Water Environ. Res.* 69 (1997), 1120-1127.

[84] Zhang, J., J.H. Dong, M. Luo, H. Xiao, S. Murad, and R.A. Normann, *Langmuir* 21 (2005), 8609-8612.

[85] Xomeritakis, G., S. Nair, and M. Tsapatsis, *Microporous Mesoporous Mat.* 38 (2000), 61-73.

[86] Xomeritakis, G., Z.P. Lai, and M. Tsapatsis, *Ind. Eng. Chem. Res.* 40 (2001), 544-552.

[87] Li, L.X, A. Ryan, Tina, M. Nenoff, J. Dong, and R. Lee. Paper SPE 89892, presented at the SPE Annual Technical Conference and Exhibition held in Houston, Texas, 26-29 September 2004.

[88] Li, L.X., J.H. Dong, T.M. Nenoff, and R. Lee, *J. Membr. Sci.* 243 (2004), 401-404.

[89] Tamura, H., K. Mita, A. Tanaka, and M. Ito, *J. Colloid Interface Sci*. 243 (2001), 202-207.

[90] Caro, J., M. Noack, and P. Kolsch, *Adsorpt.-J. Int. Adsorpt. Soc.* 11 (2005), 215-227.

[91] Ettouney, H.M., H.T. El-Dessouky, R.S. Faibish, and P.J. Gowin, *Chem. Eng. Prog*. 98 (2002), 32-39.

[92] Matz, R., and U. Fisher, *Desalination* 36 (1981), 137-151.

[93] Visvanathan, C., P. Svenstrup, and P. Ariyamethee, *Water Sci. Technol.* 41 (2000), 117-123.